Abstract

Title of dissertation: **EFFECT OF TIP CLEARANCE ON THE THERMAL AND HYDRODYNAMIC PERFORMANCE OF SHROUDED PIN FIN ARRAYS.**

Kevin A. Moores, Doctor of Philosophy, 2008

Dissertation directed By: Professor Jungho Kim,
Professor Yogendra Joshi,
Department of Mechanical Engineering

The use of shrouded pin-fin arrays to enhance heat transfer is a common occurrence in many engineering disciplines, from compact heat exchangers in the process industry, to turbine blade cooling in the aerospace industry, to system thermal management in the electronics industry. In this study, experimental methods are employed to study the effect of introducing a small clearance gap between the tips of a pin-fin array and its shroud. Three arrays consisting of tapered cylindrical pin-fins were employed for this purpose. They exhibited pin height-to-diameter ratios (H/D) of 0.5, 0.8 and 1.1, and pin pitch ratios (S_L/D and S_T/D) of 1.15 and 1.3 respectively. The arrays were heated uniformly and cooled with distilled water in a closed-loop test facility. Heat transfer visualization studies were conducted using thermochromic liquid crystals to estimate convection coefficients as a function of Reynolds number ($10^2 < Re < 2x10^4$), through a range of clearances (0 to 25 percent of pin height). Adiabatic pressure drop across the pin-fin array was also measured.

In terms of pressure drop performance, the impact of tip clearance was found to be greatest at low Re, ($< 5x10^3$), with the effect being significantly diminished by

Re = $1.5x10^4$. While the dimensionless pressure drop (*f*) eventually decreases with the addition of clearance, there appears to be an initial increase in *f* relative to the non-clearance case for clearances on the order of 5-10 percent of pin height. This increase was seen to be as much as 50 percent at Re on the order of 10^2.

Observed heat transfer trends were somewhat mixed. In some cases, a modest increase in overall heat transfer was experienced, apparently due to the exposure of the pin tips and their associated area to the cooling fluid. Highest rates of overall heat transfer tended to occur within a clearance range of 10 to 18 percent of pin height. Local heat transfer however was generally seen to decrease. On a constant pumping power basis, the inclusion of clearance was found to generally produce higher heat transfer per unit pumping power for a dimensionless clearance (Cg/D) less than 0.2, when compared to the non-clearance case.

EFFECT OF TIP CLEARANCE ON THE THERMAL AND HYDRODYNAMIC PERFORMANCE OF SHROUDED PIN FIN ARRAYS

By

Kevin A. Moores

Dissertation submitted to the Faculty of the Graduate School of the
University of Maryland, College Park, in partial fulfillment
of the requirements for the degree of
Doctor of Philosophy
2008

Advisory Committee:
Professor Jungho Kim, Chair/Advisor
Dr. Yogendra Joshi, Co-chair/Advisor
Associate Professor Andre Marshall, Dean's Representative
Associate Professor F. Patrick McCluskey
Assistant Professor Bao Yang

Dedication

To my parents Eric and Betty for giving me the confidence to pursue my dreams and to my wife Roxanna for helping me achieve them.

Acknowledgements

Thanks to all my lab-mates for their considerable help and years of friendship; Shekhar, Lan, Enchou, Sunil, Camil, Yuan, Wei, Tom, Dong, Siva, Shivesh, Qian, Robert, Jeff, Kyoung Joon, Dai Wan, Jack, Payam, Greg, Rishi, Thierry, Bahman, and Patrick. Thanks to Mr. Gary Miller of Lockheed Martin and Dr. Gerhard Schiroky of Lanxide Electronic Components Inc. each of whom represented the companies that provided significant support to my research through the CALCE Electronic Pakaging and Research Consortium. My thanks to Dr. Avram Bar-Cohen for providing me with shelter during a critical stretch of my studies. Thanks also to my committee members, Dr's McCluskey, Yang, and Marshall for their time and constructive comments regarding this dissertation. And lastly but by no means least, I owe a great deal of gratitude to my advisors Dr. Joshi and Dr. Kim for their kindness and consideration and for giving me a chance to exceed my own expectations.

Table of Contents

List of Tables

List of Figures

Nomenclature

A	area [m^2 or mm^2]
B	blue component in RGB color space [0-255 or 0-1 scale]
Bi	Biot number [nd] hL_c/k_{bp}
C	tip clearance [percent of H] (nominal unless denoted otherwise)
Cg	tip clearance gap (m)
cp	Specific heat [J/kgK]
D	average diameter [m] (of pin fin unless denoted otherwise)
f	flow friction factor [nd] - Eq. (3.15).
g	gravity constant [9.81 m/s^2]
G	green component in RGB color space [0-255 or 0-1 scale]
h	heat transfer coefficient [W/m^2K] – Eq. (3.19)
H	height [m] (of pin fin unless denoted otherwise)
H	hue component in HSV color space (0-255 or 0-1 scale)
I	electrical current [A]
k	thermal conductivity [$W/m{\cdot}K$]
L	length [m]
L_c	Characteristic length of Bi (V_{bp}/A_w)
$\dot{m}$	mass flow rate [kg/s]
nd	non-dimensional variable
N	number of pin rows in array
Nr	Number of pin fin rows from array longitudinal midpoint
Nu	Nusselt number [nd] (of array unless noted otherwise). Eq. (3.17)
P	pressure [Pa]
Pr	Prandtl Number [nd] (ν_f/α_f)
$\dot{q}''$	heat flux [W/cm^2]
Q	heat [W]
R	red component in RGB color space [0-255 or 0-1 scale]
Re	array Reynolds number [nd] – (Eq. 3.20 unless noted otherwise)

S	center-to-center pin spacing [m]
SEE	standard estimate of error [°C] (Eq. 3.4)
t	thickness [m]
	time [s]
T	average temperature [°C]
U	bulk mean inlet fluid velocity upstream of array[m/s] $\dot{V}/A_c$
V	volume (m^3)
	electrical voltage (V)
	Value component in HSV color space [0-255 or 0-1 scale]
$\dot{V}$	volumetric flow rate [m^3/s]
V_{max}	maximum array velocity [m/s] - Eq. (3.26)
W	width [m, unless noted otherwise]
	Uncertainty [units of given variable]
z	insert depth [m] (see figure 2.4)

Greek Symbols

α	Polynomial coefficient [nd]
	Polynomial exponent [nd]
	Thermal diffusivity (m^2/s)
ΔP	differential pressure [Pa]
ΔT	differential temperature [°C]
ε	Energy balance coefficient
κ	Empirical correlation coefficient [nd]
η	fin efficiency [nd] Eq. (3.24)
μ	dynamic viscosity [N-s/m^2]
θ	calibration angle [radians]
	temperature excess between pin and cooling fluid [°C]
ρ	density [kg/m^3]
σ	standard deviation [units of application]
υ	kinematic viscosity [m^2/s]

Ω	electrical resistance [ohms]
ψ	flow angle of attack [degrees]

Subscripts

100	corresponding to 100 percent pin efficiency
A	array
amb	ambient air
atm	atmospheric
ave	average
bp	base plate
c	cross-section of channel
c(0)	relative to array with no tip clearance
C > 0	relative to array with tip clearance
cal	calorimetry (ie arrived at through an energy balance)
D	diagonal direction $\left[S_L^2 + \left(S_T/2\right)^2\right]^{1/2}$
ew	endwall
f	fluid
fm	flow meter
fp	flat calibration plate
H	heater block
in	inlet of test section
L	longitudinal direction (parallel to flow)
L,cond	losses via conduction and natural convection
L,conv	losses via forced convection outside array
meas	measured
n	indices designator
out	outlet of test section
p	array projection (W_A x L_A)
pf	pin fin
pt	pin tip

t	pin tip
T	transverse direction (perpendicular to flow)
w	wetted surface
wc	water column
xdcr	transducer

Chapter 1: Introduction

1.1 Background and Motivation

The use of pin fin arrays to enhance heat transfer is common in many engineering disciplines. In the process industry, banks of pins fins are used in air-to-air and air-to-liquid heat exchangers. In the aerospace and energy industries, pin fin arrays are designed into the interior of turbine blades (**Figure 1.1a**) to help cool the airfoil-like surface, allowing the turbine to operate at higher mean temperatures with maximum efficiency. And in the electronics industry, pin fins are employed in the thermal management of systems ranging from desktop computers to the power semiconductors aboard locomotive engines.

Pin fin arrays are either shrouded or un-shrouded. In the case of a shrouded array, the pins extend from a base area and are closely constrained by opposing walls on all other sides as shown in **Figure 1.1b**. More often than not, the array is in physical contact with the shroud at both ends of the pins as depicted in **Figure 1.2a**. This arrangement is typical in heat exchanger and turbine cooling applications. While the pins themselves can come in a variety of shapes, the right circular cylinder is by far the most common. In this work, when referring to pin fin arrays, a circular cross section is implied unless stated otherwise.

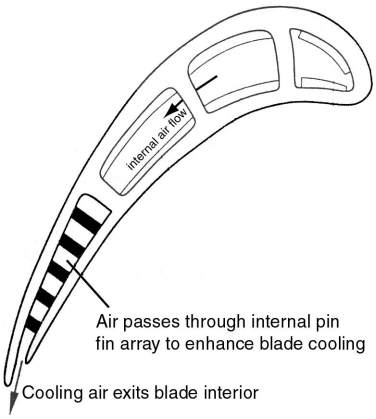

Figure 1.1 (a) Cross-section of turbine blade showing trailing edge pin array. (Modifed from Huang and Lui 1999A)

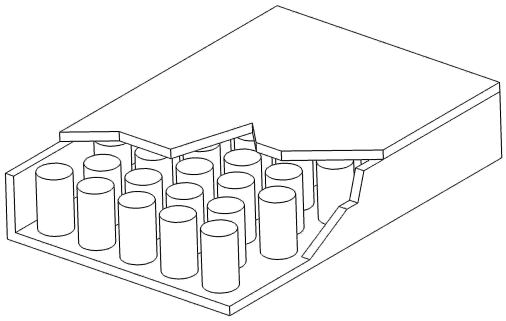

Figure 1.1: (b) Cut-away view of a basic shrouded pin fin arrangement

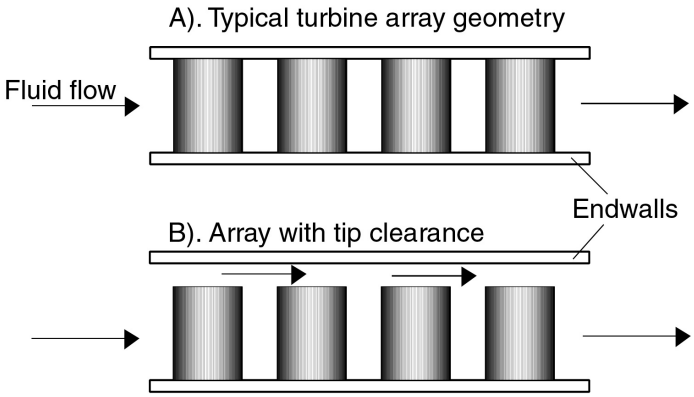

Figure 1.2: Side view of pin array (A) without tip clearance and (B) with tip clearance

Until recently, the un-shrouded pin fin array was most common in electronics cooling applications. In this situation, the array is open on all sides other than the base, and the cooling fluid is free to approach the array from any direction, or to bypass the array completely. This approach reduces system pressure drop requirements and associated noise, but it does not lend itself to the most volumetrically efficient heat transfer. It is little surprise then, that with the ever-increasing cooling demands required by today's electronic systems, thermal

management schemes are evolving towards shrouded array designs to maximize the cooling effect of a given heat sink. It is this shrouded form of the pin fin array that is considered in this study.

1.2 Objectives of Current Study

Specifically, the aim of this work is to examine the general effect of tip clearance on the performance of shrouded pin fin arrays. Though there has been a sizable amount of research conducted in the area of pin fin array heat transfer and fluid flow, very little attention has been paid to what amounts to a hybrid of the shrouded and un-shrouded scenarios, in which the sides of the array are closely contained, while a finite amount of flow area exists at the tip end of the pin fins as shown in **Figure 1.2B**.

The inclusion of tip clearance can be expected to have a number of competing influences on the thermal and hydrodynamic performance of the array. The addition of an unobstructed flow area above the fins will allow a portion of the flow to bypass the interior of the array thereby reducing local velocities within the array and decreasing the overall heat transfer performance. At the same time however, the tips of the pins become exposed to the cooling fluid, increasing the total wetted surface area of the array, which should result in an increase in heat transfer capacity of the given heat sink for a given flow field. In addition there is reason to believe that tip clearance may promote three-dimensional flow effects that act to break up the thermal boundary layer along the endwall of the array, thereby further enhancing heat transfer. It is logical to assume then, that among these competing phenomena, there

may well exist an optimum amount of clearance whereby the degenerative effects of bypass are more than offset by the additional heat transfer area and any three dimensional flow effects that may be induced.

While a considerable amount of research has been conducted regarding the performance of shrouded pin fin arrays, only a handful of studies have considered the effect of tip clearance. This is likely due to the fact that the vast majority of all such work has come from the turbine blade heat transfer research community. In turbine cooling scenarios the pin arrays are cast into the interior of the blades, spanning the full height of the blades, and perform a structural as well as a thermal role. As a result, tip clearance is not a viable option and has not been a typical consideration in blade cooling studies to date. In electronics cooling however, the pin fins typically protrude from the base of a heat sink with the tips of the pins flush against a shroud. While this is essentially the same configuration as in turbine applications, the array in this case is normally not required to perform a structural role. Therefore the inclusion of tip clearance represents only a minor change in the design of the electronics cooling system and in many cases may be accommodated relatively easily.

1.3 Literature Survey

At its essence, the scenario under consideration here is that of heat transfer due to fluid flow across an array of heated cylinders. Research in this area has been ongoing since the mid 1930's in conjunction with the development of air-to-air and air-to-liquid heat exchangers in the chemical and energy process industries. Early contributors included **Pierson (1937)**, **Huge (1937)**, and **Grimison (1937)**. All were

employees of Babcock and Wilcox Inc., a company involved in large scale heating and cooling projects. They were the first to produce generalized correlations of heat transfer and fluid resistance for the cross flow of gases over tube banks, including the effects of dimensionless tube spacing and flow conditions. A detailed review of the work done in tube bank heat transfer from that time forward was provided by **Zukauskus (1972)**. Using data from his own research and that of previous studies, he proposed a set of generalized correlations to predict heat transfer and pressure drop through an array of cylinders based on the particular geometry of the array and the thermal and fluid dynamic conditions of the flow field. While new studies in tube bank performance continue to be generated, the correlations developed by Zukauskus are still regarded today as the primary tool for empirical estimates of heat transfer and pressure drop for cross-flow through arrays of cylinders, including tube bundles and pin fin arrays.

On the other hand, while similar in nature to flow over tube bundles, the study of heat transfer in shorter pin fin arrays constitutes a separate area of research due primarily to differences in boundary conditions and associated flow phenomena. **Figure 1.3** offers a classification of cylinder arrays according to pin length-to-diameter ratio (H/D) and functional type. Pin fins in turbine blade and electronics cooling applications tend to have an H/D on the order of 10^{-1} to 10^{1}. In contrast, classic tube bundles within process heat exchangers tend to have ratios on the order of 10^{1} to 10^{2}. As a result, endwall interactions play an important role in pin fin performance, while being relatively negligible in the case of tube bundles.

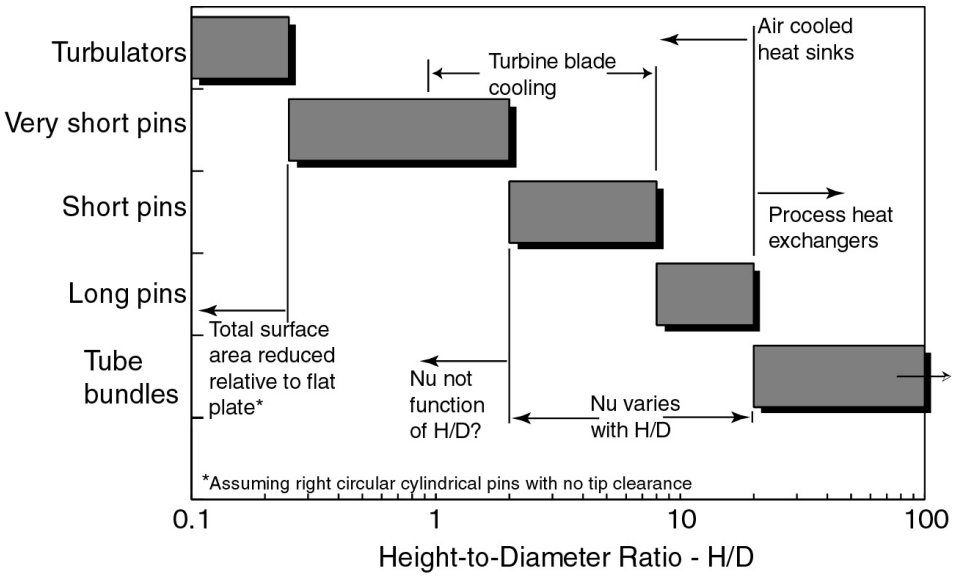

Figure 1.3: Classification of arrays by pin length to diameter ratio (H/D)

During the mid 1960's, research (**Theoclitus, 1966**) showed that this difference plays an important role in modifying pin fin heat transfer. It became evident therefore, that the vast amount of work conducted on arrays of long cylinder bundles over the previous 30 years was inadequate for understanding the performance of shorter pin fin arrays. Since that time, a number of researchers have studied the heat transfer and fluid dynamics unique to relatively short pin fin arrays. Nearly all this work has been produced in the past twenty-five years. Based on a review of the literature, the majority of the studies conducted in this area fall into one or more of nine primary categories of pin fin array performance that includes:

- Pin Length-to-Diameter Ratio (H/D) effects
- Lateral and Transverse Pin Pitch (S_T/D, S_L/D) effects
- Array Orientation effects
- Pin shape effects

- Row resolved development of Nu
- Comparison of pin heat transfer vs. endwall heat transfer
- Thermal boundary condition effects
- Channel geometry (sidewall configuration) effects
- Tip clearance effects

The majority of array geometries and associated parameters listed above are illustrated in **Figure 1.4**. A brief summary of each primary area of research is discussed, including the relevance, if any, to the current study.

1.3.1 Pin Length-to-Diameter Ratio (H/D)

Some of the earliest work on pin fins was performed by **Theoclitus (1966)** who measured array averaged heat transfer from nine inline copper pin fin arrays with H/D from 12 down to 4. He compared the results with available correlations for tube banks (H/D ≈100) and found that the relatively short pin fins under-performed in comparison by as much as 35 to 50 percent. The data also showed (with one exception) that based on total heat transfer area, pins of H/D = 12 outperformed those at H/D = 8, which in turn outperformed those at H/D = 4. **Metzger et al. (1982A,B)** looked at even shorter pin fins (H/D = 1). When comparing the results to the Zukauskus correlation for tube banks, they found a 50 percent discrepancy at Re = 10^4, with increasingly larger discrepancies (approaching 100 percent) near Re = 10^3.

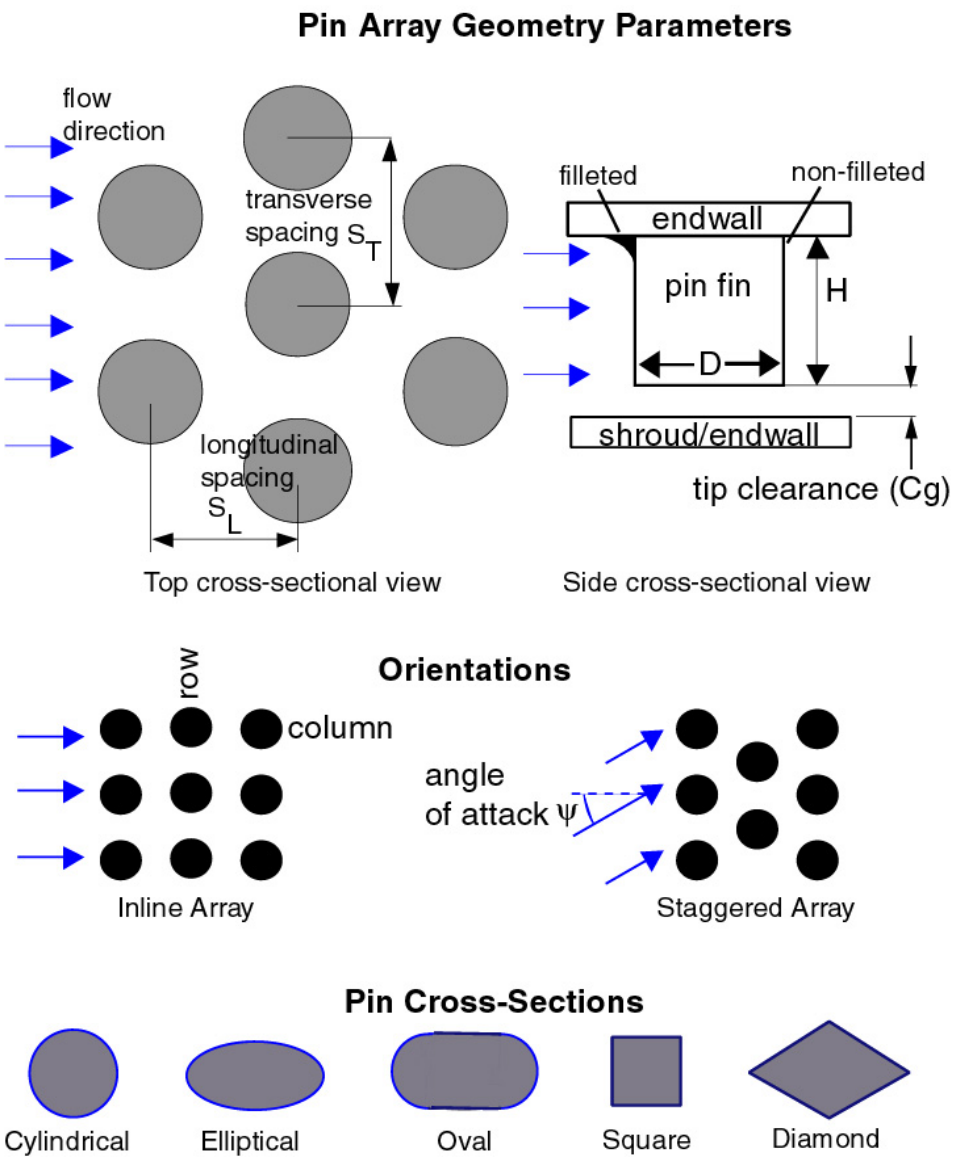

Figure 1.4: Illustration of various pin fin array parameters

In work by **VanFossen (1982)** and **Brigham and VanFossen (1984)**, arrays of H/D = 0.5, 2.0, and 4.0 were evaluated. In the latter study, this data was compared with the earlier study of Metzger and with that of **Kays and London (1955)** who's study included pins with H/D = 8.0. They compiled a set of data in the range 0.5 < H/D < 8.0 which showed Nu to be independent of pin length for H/D ≤ 2.0. Above

this ratio, there was a substantial increase in Nu at increasing pin lengths, with the effect being greater at low Re (10^3) than at high Re (10^5).

On the other hand, **Sparrow et al. (1981)** considered pin fin arrays of $7 \leq H/D \leq 19$. Employing napthalene sublimation, they found no effect of pin length on the mass transfer rate. They also found their data to be in excellent agreement with that predicted by the Zukauskus correlation for tube banks. However, the fins in that study were attached to only one endwall, and had a tip clearance of 71 percent of pin height.

Armstrong and Winstanley (1988), in their review of pin array performance for turbine cooling applications, argue that the lower Nu level for shorter pins is due to domination of endwall interactions with the pin fins, which they assert extends out to about one pin diameter from the wall. For pin lengths substantially larger than the diameter, higher heat transfer coefficients along the pin dominate the overall performance, and mean heat transfer approaching that of tube bundles is achieved.

A survey of H/D considered in the literature is summarized in **Figure 1.5**. The pin fins in the current study are in the range of H/D = 0.5 to 1.1. While a large number of these previous studies considered H/D on the order of 1, only a handful has considered cases where H/D is less than unity. As such, one of the aims of this study is to provide additional test data in this little considered region, and in doing so, test the earlier assertion of VanFossen et al. (1982, 1984) that H/D has little or no affect on heat transfer below H/D = 2.0.

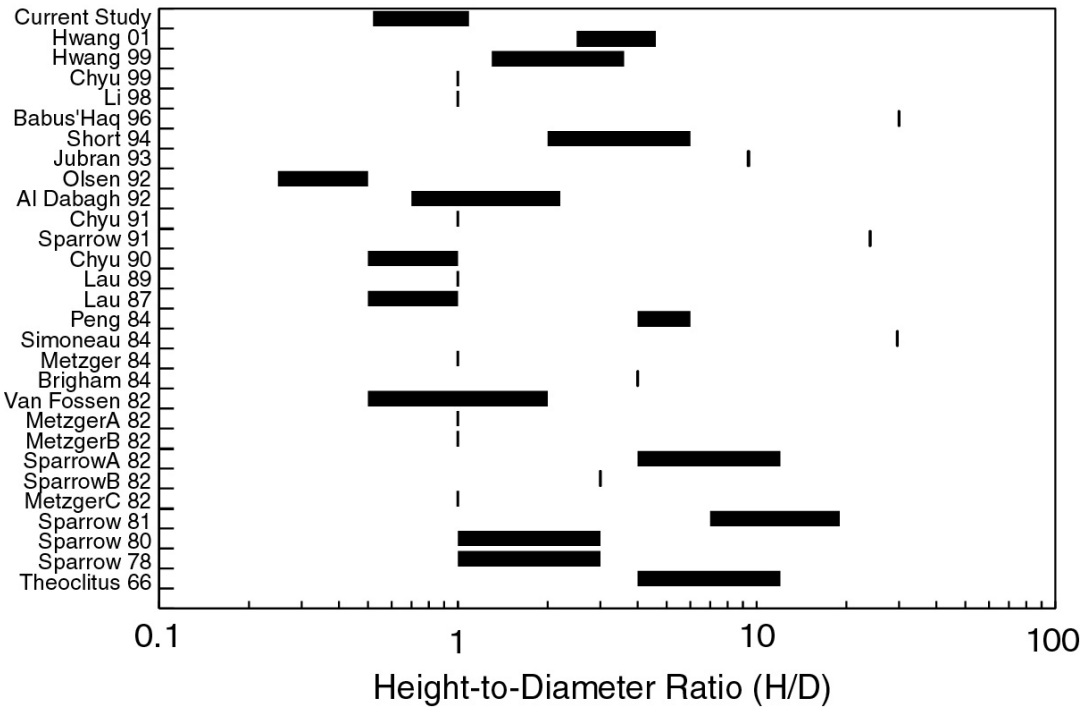

Figure 1.5: Survey of pin length-to-diameter ratios considered in pin fin array literature

1.3.2 Longitudinal and Transverse Pin Pitch (S_L/D, S_T/D)

Metzger et al. (1982A) were among the first to consider the effects of pin spacing and pitch in a systematic fashion. They looked at the change in Nu with increasing longitudinal pin pitch ranging from 1.05 to 5.0. Metzger reported an increase between the two extremes to be over 100 percent at Re = 2000, with the difference being closer to 50 percent at Re = 40,000. The effects of transverse pitch were not considered.

Short (1994) evaluated by far the largest number of pin spacing combinations to date. Fifty separate pin fin arrays with S_T/D of 1.8 to 3.2 and S_L/D of 2.0 to 6.4 were tested. Empirical correlations for both Nu and *f* as a function of pin pitch and H/D were proposed and his results suggested that heat transfer is moderately affected

by the transverse pitch but is relatively independent of longitudinal pitch, which is contrary to the earlier findings of **Metzger (1982A)**. Unfortunately, Short's data were not adjusted to account for the affects of fin efficiency, so the correlations are of limited practical use.

Jubran et al. (1993) on the other hand, evaluated the widest range of pin pitches to date. They claim that an optimum pin spacing based on maximum heat transfer per unit area occurs at equal longitudinal and transverse pin pitches of 2.5. They have also proposed empirical correlations for mean array heat transfer that suggest longitudinal spacing to have a slightly higher impact on performance than transverse spacing. Again, unfortunately in this case, the authors chose to non-dimensionalize the correlations based on array width and length, rather than pin diameter, making comparisons with other works difficult, and general use of the correlations impractical.

Babus Haq et al. (1995) also considered heat transfer from arrays with a wide pitch range. They claim the optimum pitch to be between 1.6 and 1.9 in the transverse direction, and approximately 2.0 in the longitudinal direction. This is somewhat lower than the findings of Jubran et al. The results are based on a single Reynolds number of 1800, where Re is based on the bulk mean fluid velocity. The arrays of Bubus'Haq deviated from most of those considered in the literature in that H/D was 30, which is by far, the greatest relative pin height of all the studies reviewed.

Longitudinal pitch and transverse pitch are not varied in the current study. With $S_L/D = 1.15$ and $S_T/D = 1.3$, the arrays to be considered here are rather densely packed compared to the majority of those considered in the literature. As a result, the

data generated in this work will help cover a region not often evaluated. **Figure 1.6 and Figure 1.7** illustrate the range of pin pitches evaluated in previous studies.

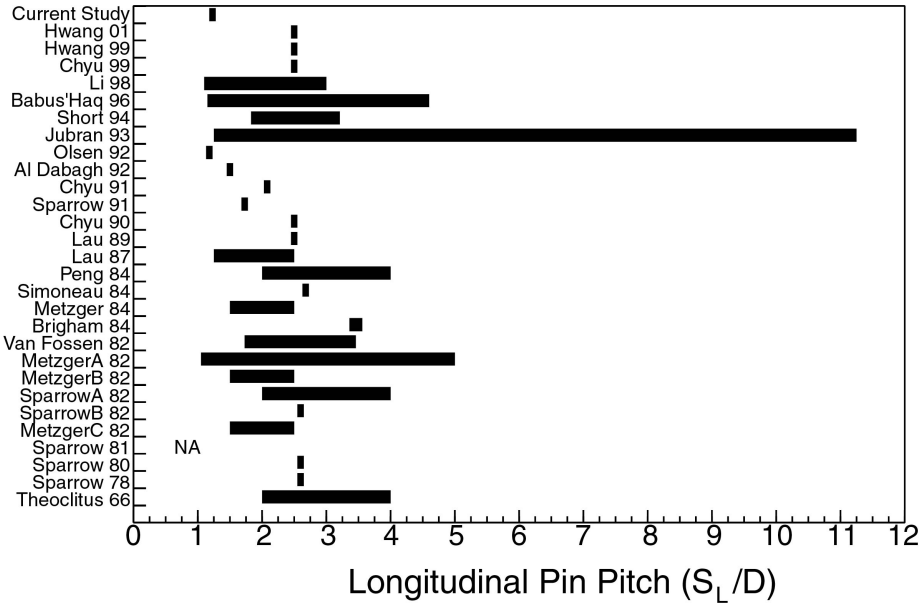

Figure 1.6: Survey of longitudinal pitch (S_L/D) ranges considered in pin fin array literature

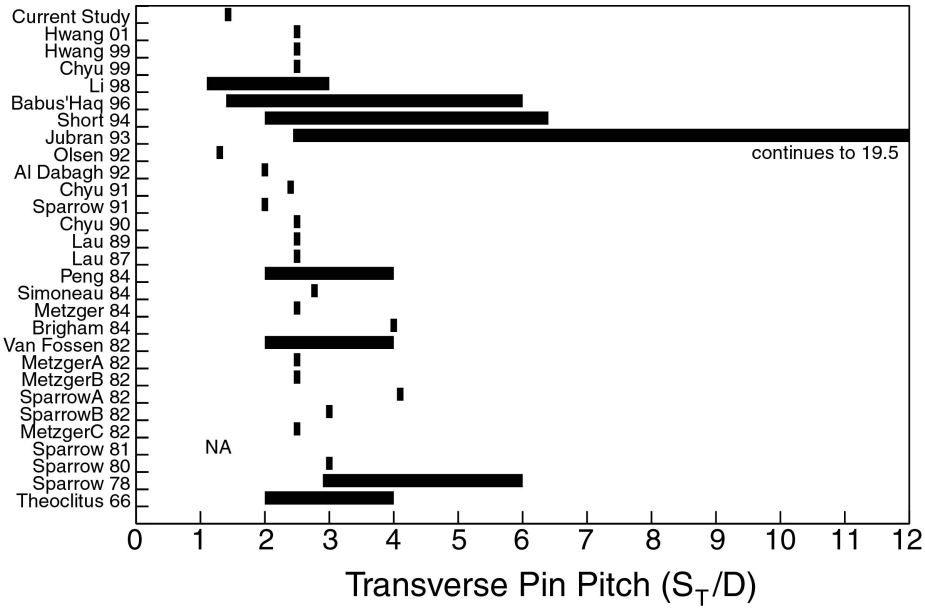

Figure 1.7: Survey of transverse pitch (S_T/D) ranges considered in pin fin array literature

1.3.3 Array Orientation

The most common orientations in pin fin arrays are inline and staggered (see **Figure 1.4**). The inline configuration consists of uniform rows and columns of pins while in the staggered array, rows are offset by half the transverse pin spacing. The pin arrays employed in the current study are of the staggered variety.

Sparrow et al. (1980) employed naphthalene sublimation to compare the relative performance of these two configurations. They concluded that inline arrays transfer more heat at a given pumping power and surface area, while the staggered array minimizes the surface area required for a fixed heat duty and flow rate. Therefore, the answer to which orientation is most efficient depends on what operating parameter is to be optimized.

The inline and staggered arrangements are not the only possible orientations, but instead represent the two extremes that are possible. By altering the angle at which the flow encounters an array, any inline array can be made to appear as a staggered array and vice versa. **Metzger et al. (1984)** looked at the effect of altering the so called angle of attack (ψ) (refer to **Figure 1.4**). They varied the flow from $\psi = 0$ degrees where the fluid sees a staggered array, to $\psi = 40$ degrees where the array appeared to the flow to be inline. They found that an intermediate angle of 26 degrees produced the highest rates of heat transfer through the majority of Re range tested, producing a 9 percent increase in Nu and an 18 percent decrease in pressure drop across the array relative to $\psi = 0$.

In the current study, the orientation remains unchanged. The array under consideration is in a staggered formation with each pin positioned equidistant from it neighbors.

1.3.4 Pin Shape

By far, the most common pin fin type is the right circular cylinder, and most studies have been based on this type. This is probably due to the fact that in molding and extrusion processes, a cylindrical shape is more easily cast. For example, the arrays in this study were produced in a molding process, and manufacturing concerns dictated the shape of the pin fins. Still, a handful of researchers have looked at the relative performance of other pin shapes in hopes of finding an optimum configuration superior to that of cylindrical pins.

Metzger et al. (1984) evaluated the performance of pin fins with an oblong cross-sectional area, where the length of the pin is twice the end diameter, and compared them to cylindrical pin fins. In their simultaneous study of pin shape and array orientation, they found the oblong pins to have a maximum Nu at $\psi = 30$ degrees. This orientation resulted in heat transfer approximately 20 percent higher than that produced by an array of circular pin fins. But this increase was more than offset by a 100 percent increase in pressure drop.

Li et al. (1998) compared the performance of oblong pin fins using a single naphthalene pin among an array of wax pins. They found the oblong pins to exhibit slightly higher Nusselt numbers than cylindrical pin fins at a given Reynolds number, while resulting in significantly (44 to 66 percent) lower pressure losses. In an earlier

study, **Li et al. (1996, in German)** considered "drop shaped" pin fins and found Nu to be 8 to 29 percent higher at a given Re while experiencing about half the pressure loss of what the authors claim to be an equivalent cylindrical pin array.

Chyu et al. (1998) made a direct comparison between inline and staggered arrays with cylindrical, square, and diamond shaped pin fins. They found the maximum heat transfer rate (from highest to lowest) to be produced by the staggered square, staggered diamond, inline square, staggered cylinder, inline diamond, and inline cylindrical in that order. Conversely, they found the maximum pressure drop (from highest to lowest) to be produced by the staggered diamond, staggered square, staggered cylinder, inline diamond, inline cylinders and inline square in that order. The staggered square array on average, produced an Nu approximately 20 to 40 percent higher than the diamond array, and 30 to 80 percent higher than the cylindrical array. For the inline case, the differences were 10 to 20 percent and 10 to 40 percent respectively. However in each case, a larger percentage increase in pressure drop was required to achieve the given heat transfer improvements.

Apart from the issue of pin cross-section, **Chyu (1990)** considered the effect of pin fillet on array heat transfer (see **Figure 1.4**). In most studies done to date, the test assemblies have consisted of fabricated arrays where the pin is inserted into a hole in the endwall, thereby producing a right angle at the base of the pin. However in many real world applications such as turbine blade cooling, the pin fins are cast and have a fillet or radiused endwall profile. Chyu found that filleted pins produced 6 to 13 percent lower heat transfer than straight pins at the leading row of an array, with the difference decreasing with increasing Re.

The pins considered in the current study differ slightly from most cylindrical fins considered in the literature in that they are tapered from the base to the tip at an angle of 4.8 degrees and possess an endwall fillet. **Short (1994)** also reported his arrays to posses a slight taper, although the angle was not specified. This shape is often referred to as a tapered pin or truncated spine. However, the taper in this case is rather small, so related performance effects are expected to be minimal, and direct comparisons with non-tapered pin arrays are made.

1.3.5 Row Resolved Development of Nu

A number of authors have considered the behavior of Nu along the longitudinal or streamwise direction of the array. Of all the aspects of pin fin array performance, this is perhaps the best understood, with few remaining questions. **Sparrow et al. (1980)** showed Nu to be lowest in the first row of the array, with an increase at the second to third rows as concomitant mixing occurs, and a subsequent decrease and leveling off in later rows as the heat transfer becomes fully developed by the fourth or fifth row.

Metzger et al. (1982B) found similar behavior with the exception that the increase in Nu was delayed into the third or fourth row, and instead of a leveling off, they found the heat transfer to gradually decrease in subsequent rows. They found a difference of 12 percent between the maximum Nu achieved and that attained in the final (tenth) row of the array.

Chyu (1990) was able to bridge the gap between the two earlier studies. He found Nu to reach a maximum by the second or third row. At low Reynolds numbers,

Nu appeared to plateau past the fifth row as was observed by Sparrow. However, as Reynolds number was increased, the gradual decrease in Nu reported by Metzger was observed. In a later study, **Chyu (1998)** considered the development of Nu in pin arrays with square and diamond shaped cross-sections. The results show that heat transfer development is similar in non-circular arrays as well.

In the current study, only the interior rows (fifth to thirteenth out of fifteen) of the array are considered. Based on this restriction, the heat transfer of the observed rows is expected to be fully developed.

1.3.6 Endwall vs. Pin Heat Transfer

In contrast to the development of the mean heat transfer along the length of the array, the question as to the relative magnitudes of pin fin heat transfer (Nu_{pf}) verses endwall heat transfer (Nu_{ew}) is perhaps the most unsettled. A relative comparison between the rate of heat transfer from pin fins and that of the endwall was first attempted by **Van Fossen (1982).** He fit experimental data to an analytical model of the pin and endwall heat transfer and estimated that Nu_{pf} was approximately 35 percent higher than that of Nu_{ew}.

Metzger et al. (1982A) disputed this claim based on performance comparisons between arrays constructed of thermally conductive pins, and identical arrays composed of non-conducting (wooden) pins. They found the performance between the two to be within ten percent of one another (based on active heat transfer area) for $5000 < Re < 50{,}000$. More directly, their results suggested the relationship to be somewhat dependent on Reynolds number, with the endwall heat transfer greater

than that of the pins at the lower end of the range (Re < 10,000), and less than that of the pins at the high end of the range (Re > 20,000).

Metzger et al. (1984) again revisited this aspect in a study on pin shape and flow orientation. They compared their results using non-conducting pins, with those of another study (**Metzger 1982B**) involving thermally conducting pins, and estimated the pin heat transfer to be 180 percent to 210 percent that of the endwall, depending on tranverse pitch. This relationship was found to be essentially independent of Re.

This aspect was also considered by **Al Dabagh and Andrews (1992)**. They examined the performance of three staggered arrays of hollow pin fins with H/D of 0.7, 1.0, and 2.2, using a large number of thermocouples inserted into the endwalls, and on the inner surface of the pins. Their conclusion contradicted that of the previous studies and found Nu_{ew} to be up to 40 percent higher than Nu_{pf}, with no clear dependence on Reynolds number.

Recently, several investigators have employed the naphthalene sublimation technique, which is particularly suited to the task of comparing the two heat transfer rates. **Li et al. (1998)** looked at a staggered array of elliptical pins, in which a molded pin of solid naphthalene was placed among similar wax pins. The section of endwall local to the test pin was also constructed of naphthalene. Their results showed Nu_{pf} to be as much as 23 percent higher than Nu_{ew} at low Reynolds number (1500), with the ratio between the two reaching unity by Re = 8000. This ratio falls between that of **VonFossen (1982)** and **Metzger (1982A)** as described above, but the relationship is completely reversed from that of **Metzger (1982B)**. Interestingly, both studies

showed the cross-over point to occur at approximately the same point (Re = 8000 - 10,000).

Chyu et al. (1999A) coated an entire array of pins and the complete endwall with naphthalene, and evaluated the relative rates of mass/heat transfer from both an inline and staggered array of cylindrical pins. They found array averaged values of Nu_{pf} in both cases to be 10 to 20 percent higher than Nu_{ew} , but with no clear dependence on Re.

In all, a half dozen studies directly comparing pin and endwall heat transfer are known to have been conducted thus far. All were based on relatively similar geometries, with H/D in the range of approximately 1-2, and both transverse and streamwise pitches between 2 and 4. Among them, Nu_{pf} / Nu_{ew} has been reported to be as high as 2.1 and as low as 0.6. Several studies have indicated a dependence on Re, while several others show little or no such dependence. The two most recent studies, based on mass transfer measurements, both suggest the ratio to be on the order of 1 to 1.2, particularly for $Re < 10^4$. While this agreement is promising, additional studies appear warranted considering the overall inconsistency in results reported to date. Unfortunately, the techniques used in this study are not sufficient to address this particular issue.

1.3.7 Boundary Conditions

The effect of thermal boundary conditions on pin fin array performance has not received any real attention in the literature. As opposed to the other eight issues described in this report which have been considered to some degree, it is the near total

lack of attention paid to this issue that sets it apart as one worthy of mention. It is well established for open channel flow that the magnitude of Nusselt number is dependent on the type of thermal boundary condition present. Of 34 experimental studies reviewed by the author, just over three quarters approximate a steady state isothermal boundary condition or employed a transient technique that assumes a far-field isothermal boundary. Less than a quarter of the studies have been based on an isoflux boundary condition. No studies were found that directly compared the difference between the two idealized boundary conditions.

The prominence of the isothermal boundary condition is due in part because the majority of studies have come from the turbine blade research community. While in reality the turbine blade does not operate isothermally, it is probably the best idealized boundary condition for modeling turbine blade passages. Conversely, **Short (1994)** was the first to remark on what is a potential problem when applying this research to electronics cooling. He noted that many electronics cooling applications typically involve what is better described as an isoflux boundary condition than an isothermal one. He also noted that the few studies that had employed the isoflux condition also situated the pin fins between two thermally conducting endwalls as is the case in turbine cooling. In contrast, a typical electronics cooling application often employs a non-conducting shroud or endwall. Short established the first sets of comprehensive pin fin data and empirical correlations based on the electronics cooling scenario. However, he did not make a direct comparison between the different endwall boundary conditions.

To date, this is an issue having yet to be studied in earnest. While this issue is not directly considered in this work, the data to be presented here appears to be one of few since that of **Short** to employ the boundary conditions most appropriate to the application of electronics cooling as opposed to turbine blade cooling.

1.3.8 Channel Geometry

This issue is particular to the performance of turbine blade cooling arrays and is of little practical concern to the present study. It involves the differences in channel cross-sectional area and flow inlet conditions that occur in actual blade passages compared with those used in most literature studies. While most work has been based on channels with rectangular cross-sections, turbine blade passages are generally more trapezoidal in nature and exhibit a gradual decrease in channel height along the flow length as depicted in **Figure 1.1a**. Studies in channel geometries have also considered the effect of lateral ejection along the length of the pin array, which is also particular to turbine cooling. Recent studies in these areas include **Hwang et al. (2001, 1999A, B)**, **Chyu et al. (1999A,B)**, and **Lau et al. (1989)**.

1.3.9 Tip Clearance

This ninth and final issue is the primary focus of the current study. Only a handful of researches have considered tip clearance in relation to pin fin arrays. **Sparrow et al. (1978, 1980)** first considered the effect of tip clearance on the performance of a shrouded array of short pin fins. They considered both inline and staggered arrays with H/D of 1, 2, and 3 with a constant duct height, which resulted in clearance gap-to-pin length ratios (Cg/H) of 0.14, 0.72 and 2.44. The study, which

employed a single naphthalene coated cylinder within an array of non-coated cylinders, found only a 20 percent decrease in Nu_{pf} between the two extreme tip clearances for staggered arrays. They also found little difference in performance between inline and staggered arrays for the case of large tip clearance. However, their work did not include a case with zero tip clearance, so the relative impact of clearance on the performance as compared to this more common baseline situation is not available.

Peng, (1984) evaluated a series of arrays in which the pins extended from each endwall, but were shorter than half the channel height, thereby leaving a gap through the center of the channel. The author evaluated gaps that were 0, 100 and 200 percent of the total pin length (summation of top and bottom pins), and found the configurations with a gap produced lower heat transfer rates due to significant flow bypass through the center portion of the channel. However, the ratio of Nu/f generally increased, thereby producing a higher rate of heat transfer per unit of pressure drop, particularly for Re > 5,000. But because of the geometry involved, the results are, for the most part, only applicable to turbine blade applications.

Jubran et al. (1993) considered inline and staggered arrays with (Cg/H) of 0, 0.5 and 1.0, proposing correlations for each clearance. The reduction in heat transfer between the two extremes was found to be 40 percent, or twice that reported by Sparrow, despite the fact that the maximum clearance in this case was less than fifty percent of that in the case of Sparrow. Unfortunately, they chose to non-dimensionalize the results based on the width and length of the array, which makes extension of the results to other geometries difficult.

Chyu et at (1999C) looked at the effect of tip clearance. In this study an inline array of pins with square cross-section was considered, with Cg/H values of 0, 0.25, 0.5, 1.0, and 2.0 evaluated. The pins were constructed from Plexiglas and a transient liquid crystal technique was used to determine endwall and pin heat transfer coefficients. They found Nu to be only 1.5 percent lower at Cg/H = 0.25 compared to the case with no gap, while at the maximum clearance, Nu was 45 percent lower, which is a similar result to that found by Jubran.

With regards to the introduction of three-dimensional effects, **Sparrow and Samie (1981)** have shown that for a single pin fin attached to a wall at only one end, the relative rate of heat transfer is higher at, and adjacent to, the tip of the fin than along the lateral face of the pin away from the tip. In other words, the exposed tip of the pin not only increases the total heat transfer area; it may produce a higher coefficient of heat transfer than the rest of the pin does on average. Also, **Chyu (1999c)** reported increased heat transfer along the endwall, upstream of the array's leading edge, when tip clearance was present. He credited the production of vortices along the tips of the pin fins and their subsequent interaction with the endwall for this behavior.

Finally, a very recent numerical study of low Reynolds number flow and heat transfer within pin fin arrays was conducted by **Rozati, Tafti, and Blackwell** (2008). This is the only previous study, either experimental or numerical, known to systematically consider the effect of relatively small amounts of tip clearance on heat transfer and pressure drop. Their study was based on arrays with transverse and longitudinal pin pitches of 2.12 and 1.06 respectively, with Cg/H varying from 0 to

67 percent, H/D from 1.0 to 0.6, and Re from 5 to 400. Their simulations suggested tip clearance effects to be a relatively complex phenomenon. Among their findings, their model predicted clearance to be of greatest impact on heat transfer at low Re, and they saw an increase in heat transfer relative to the non-clearance case for some ranges of Re and Cg, with decreases in heat transfer under other conditions.

Beyond the studies as described, there appears to be no experimental work to date which has fully considered, in a systematic manner, the effect of low levels of tip clearance on the performance of a cylindrical pin fin array. This therefore, is the primary focus of the current study.

1.3.10 Tabulation of Survey Data

Additional details regarding the studies mentioned here, as well as others, have been tabulated and are provided in **Appendix A**. **Table A.1** provides a summary of the geometries and experimental conditions covered in each study. **Table A.2** provides a cross-reference showing the primary areas of investigation covered in each study. **Table A.3** summarizes the empirical correlations gathered from these studies, with the relevant limitations of each described.

1.4 Overview of Present Study:

In summary, the aim of this study is to investigate in a parametric fashion, the effect of tip clearance on the pressure drop and mean heat transfer rate across a given pin fin array. The relative performance of an array with tip clearances (Cg) that are

nominally 0, 6, 12, 18, and 25 percent of the total pin height are investigated and discussed.

In **Chapter 2**, a description of the experimental apparatus and the data acquisition procedures used in this study are presented. Data reduction techniques including estimation of experimental uncertainties and assumptions used in the analysis of the data are summarized in **Chapter 3**. Presentation and discussion of the experimental results are provided in **Chapter 4**. This includes both quantitative as well as qualitative heat transfer results based on full field liquid crystal thermography, as well as hydrodynamic results regarding general pressure drop characteristics of the array. Finally in **Chapter 5**, a summary of the contributions of this work is provided, along with suggestions for future research.

Additional detailed information not contained in the body of this report is provided in the appendices. As mentioned earlier, **Appendix A** contains a tabulated survey of the literature including available correlations and corresponding limitations. Details of the uncertainty analysis of experimental data are given in **Appendix B**. Photographs and technical drawings of the test assembly are provided in **Appendix C**.

Chapter 2: Experimental Setup and Procedures

Experiments were conducted using a custom designed, water cooled, closed-loop test facility. Temperature measurements were made using thermocouples and through the evaluation and analysis of thermochromic liquid crystals coated onto the surface of the pin fin arrays. The liquid crystal measurements produce two-dimensional images that provide both quantitative and qualitative information and are supplemented by the thermocouple measurements. Separate adiabatic pressure drop measurements were also made using a differential pressure transducer. The following sections describe in detail, the apparatus used and the test procedures that were followed. Procedures and the theoretical basis for the analysis of the experimental data are considered in **Chapter 3**.

2.1 Test Specimens

A set of three power electronics base plates were used as the test vehicles to evaluate pin fin performance as a function of tip clearance. The base plates, manufactured by dmc^2 Electronic Components Inc., are composed of an Aluminum Silicon-Carbide (AlSiC) metal matrix composite and are formed into the shape shown in **Figure 2.1A** through a molding process and high temperature infiltration stage. The base plate and pin fin array comprise a single, contiguous structure with uniform properties throughout. The pin fins have a 4.8 degree taper angle from base to tip to facilitate removal from the mold during manufacturing. As a result, the pin diameter varies slightly along the length of the fin as evident in **Figures 2.1** and **2.2**. The three

base plates considered here are geometrically identical except for pin height which varies between 2 mm and 4 mm, resulting in a height-to-diameter aspect ratio of between 0.5 and 1.1. All three test specimens were fabricated as identical base plates with 6 mm pin fin heights. Each base plate then underwent a grinding process to arrive at its final pin height. The three geometries are shown in **Figure 2.1B – 2.1D**. A summary of the base plate dimensions and material properties is provided in **Table 2-1**.

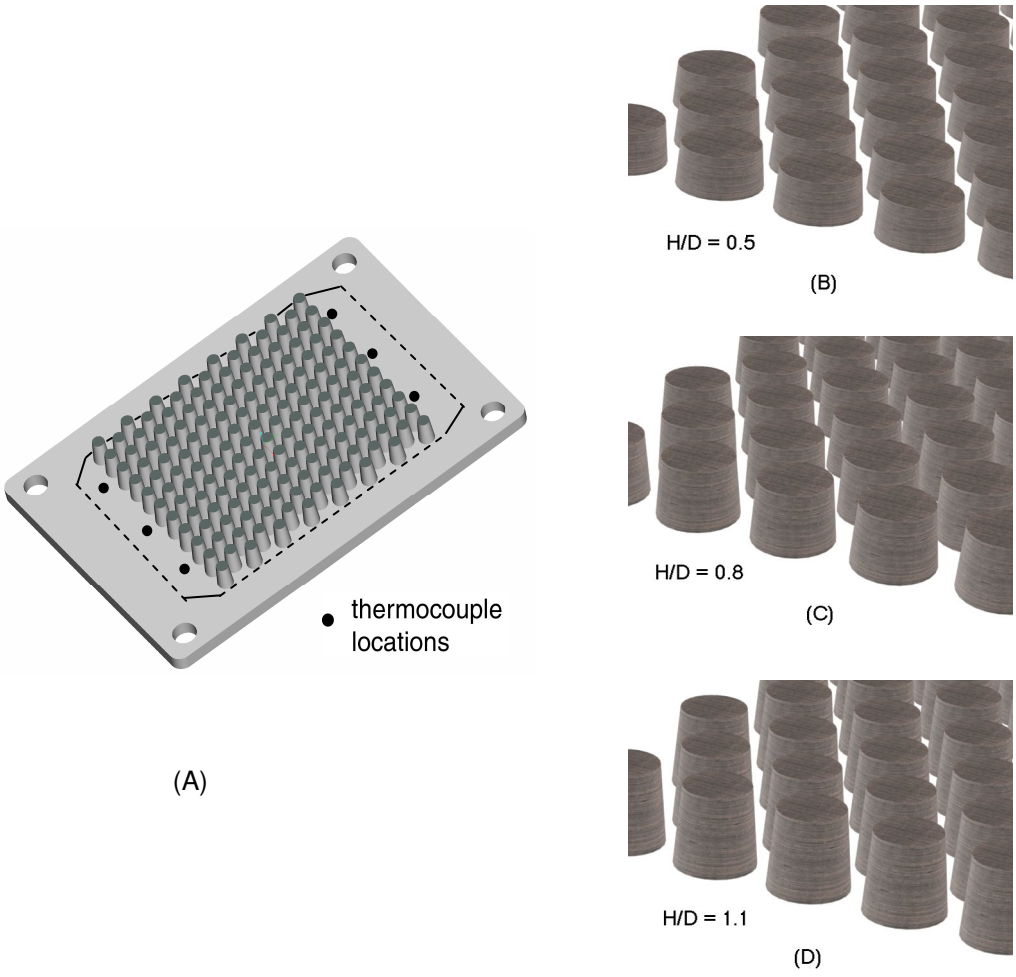

Figure 2.1: 3-D models of full AlSiC base plate and each of (3) pin configurations

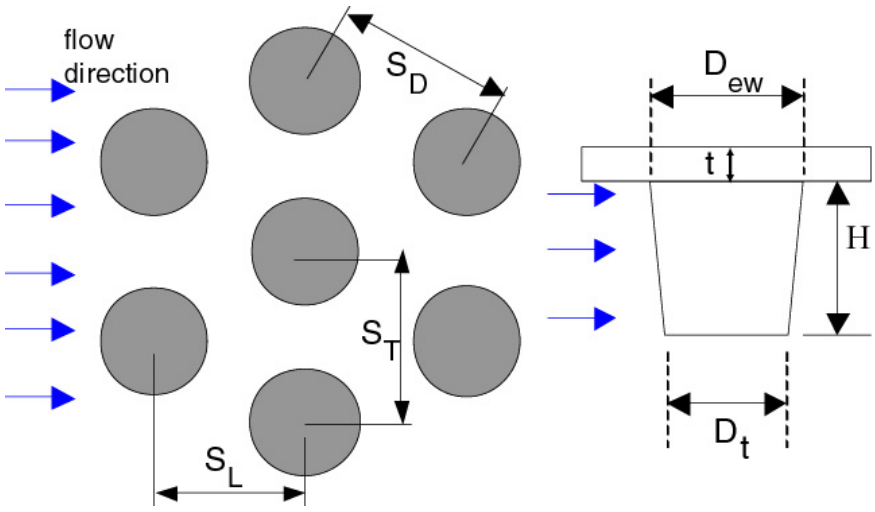

Figure 2.2: Test specimen pin fin array geometry definitions

Table 2-1. Array dimensions and material properties

Plate:	#1	#2	#3
W_{bp},W_A :	0.072 , 0.054		
L_{bp},L_A :	0.106 ,0.065		
t_{bp}:	0.005		
H (mm):	2.0	3.0	4.0
D_{ew} (mm):	4.0	4.0	4.0
D_t (mm):	3.67	3.5	3.33
D (mm):	3.84	3.75	3.67
S_T (mm):	5.0	5.0	5.0
S_L(mm):	4.33	4.33	4.33
H/D:	0.52	0.8	1.09
S_T/D:	1.3	1.33	1.36
S_L/D:	1.13	1.15	1.18
A_p (mm^2)	3570	3570	3570
$A_{w,c(0)}$ (mm^2)	3497	4389	5238
$A_{w,c>0}$ (mm^2)	5168	5909	6614
N:	15		
Pins/Row:	11/major row; 10/interstitial row		
k_{bp} (W/m K):	160		

2.2 *Test Assembly Design and Construction*

The base plates were evaluated by mounting them on an open-channel aluminum and Plexiglas housing as depicted in **Figure 2.3** and **Figure 2.4**. The lower section of the housing was milled from a single piece of aluminum to provide good rigidity and strength to the assembly. Plexiglas was chosen as the upper section for its insulating properties and to allow for liquid crystal visualization of the pin fin array during operation. Silicone rubber O-rings provided a seal between the mating faces of the base plate and aluminum housing, and between those of the Plexiglas and Al housing. A Plexiglas insert sitting atop a silicone sponge gasket was situated between the tips of the pin fins and the Plexi housing. Four set-screws located at the corners of the insert and threaded into the body of the upper housing enabled the insert to be raised and lowered relative to the tips of the pin fins to control clearance. In the case of zero clearance, the set screws were removed and sufficient gasket material placed under the insert to insure that when the base plate was bolted onto the housing, the tips of the pins pressed down onto the insert, compressing the gasket material. This assured good physical contact between the pins and insert across the entire array.

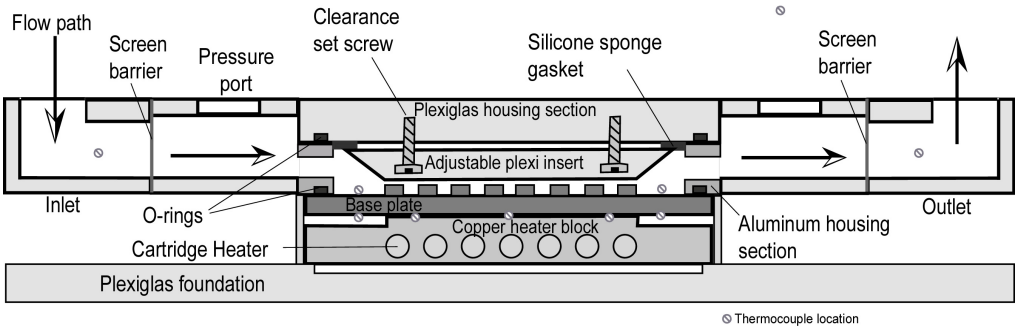

Figure 2.3: Primary test assembly, side cross-sectional view

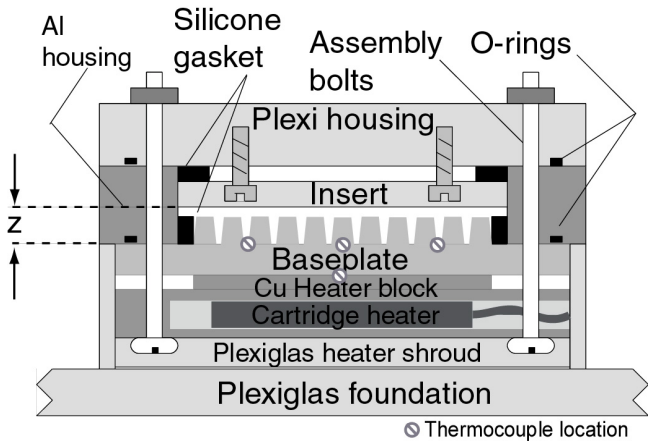

Figure 2.4: Primary test assembly, end cross-sectional view

Pressure taps were located directly upstream and downstream of the main housing section. These segments were also machined from Plexiglas and ported to an Omega PX771-100WD1 piezo-resistive differential pressure transducer to measure pressure drop across the test section. Fiber glass window screening (7.1 x 6.3 mesh/cm; 0.028 cm wire diameter) was situated between each end section and the adjoining pressure tap section to promote a uniform flow field to the pin array, and for better mixing of the fluid downstream of the base plate to assist in bulk fluid temperature measurements. Beyond this, no attempt was made to characterize or condition the flow into the array due to limitations imposed by O-ring seal requirements.

A copper block with seven embedded cartridge heaters (Omega #CIR-10201/240) was used to provide a uniform heat flux to the base plate. The face of the heater block was undercut so that it came in contact with the base plate only along the area corresponding to the pin array on the opposite side of the plate. The block was mechanically fastened to the base plate and housing by machine screws, with thermal

joint compound (Thermalloy Inc., Thermalcote II) applied at the heater-to-baseplate interface to minimize contact resistance. The copper block was then enclosed in a plexiglas shroud and mounted onto a plexiglas foundation, which in turn rested on a layer of Styrofoam insulation in order to minimize heat losses through the base.

The primary test assembly was operated in a closed-loop facility as depicted in **Figure 2.5**. Upstream of the test assembly, a Lauda WK500 chiller with integral pump provided distilled cooling water at a constant flow rate and inlet temperature (± 1°C). During adiabatic pressure drop tests only, a peristaltic pump was used in place of the chiller pump, which enabled testing to be extended up to $Re = 1.8 \times 10^4$. Located between the chiller and assembly was a pair of bypass valves to control flow rate to the test section, a 1μm cartridge filter to remove any particulates in the flow stream, and a series of three Blue-White Industry Inc. variable area flow meters:

Model Number	Flow Range - m^3/s (L/min)	
F-44250LH8	0 - 1.67×10^{-5}	(0 – 1.0)
F-375LH8	1.67×10^{-5} - 6.67×10^{-5}	(1.0 – 4.0)
F-376LH8	2.67×10^{-5} - 1.33×10^{-4}	(1.6 – 8.0)

The three meters were connected in parallel with individual shut-off valves, such that a single meter was operated at any given time depending on the flow rate requirements. (A fourth high flow capacity meter was also present, as shown in **Figures 2.6** and **2.7**, but was never used due to head limitations of the chiller pump). From the flow meters, the cooling water entered the test assembly, and upon leaving the assembly, returned directly to the chiller.

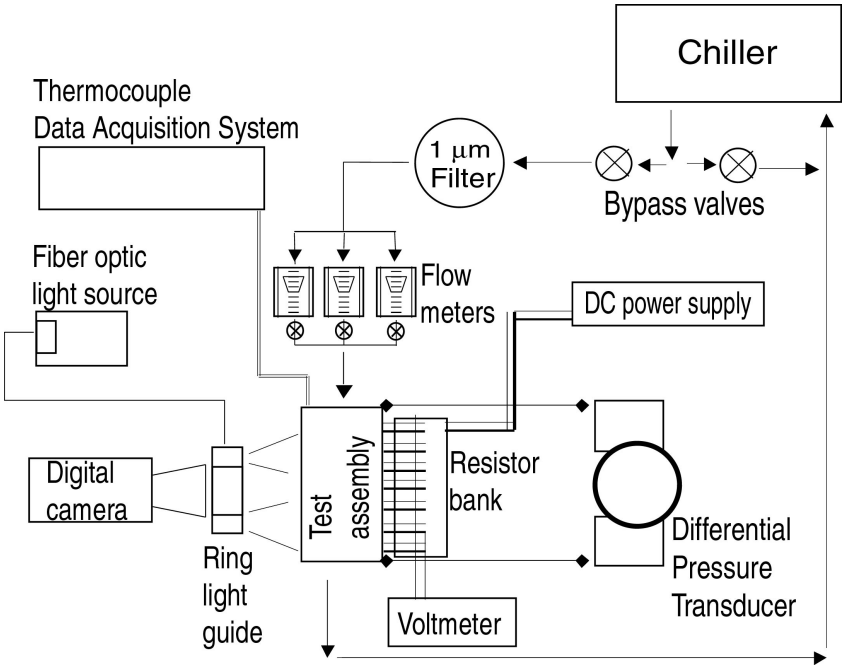

Figure 2.5: Schematic of closed loop test facility

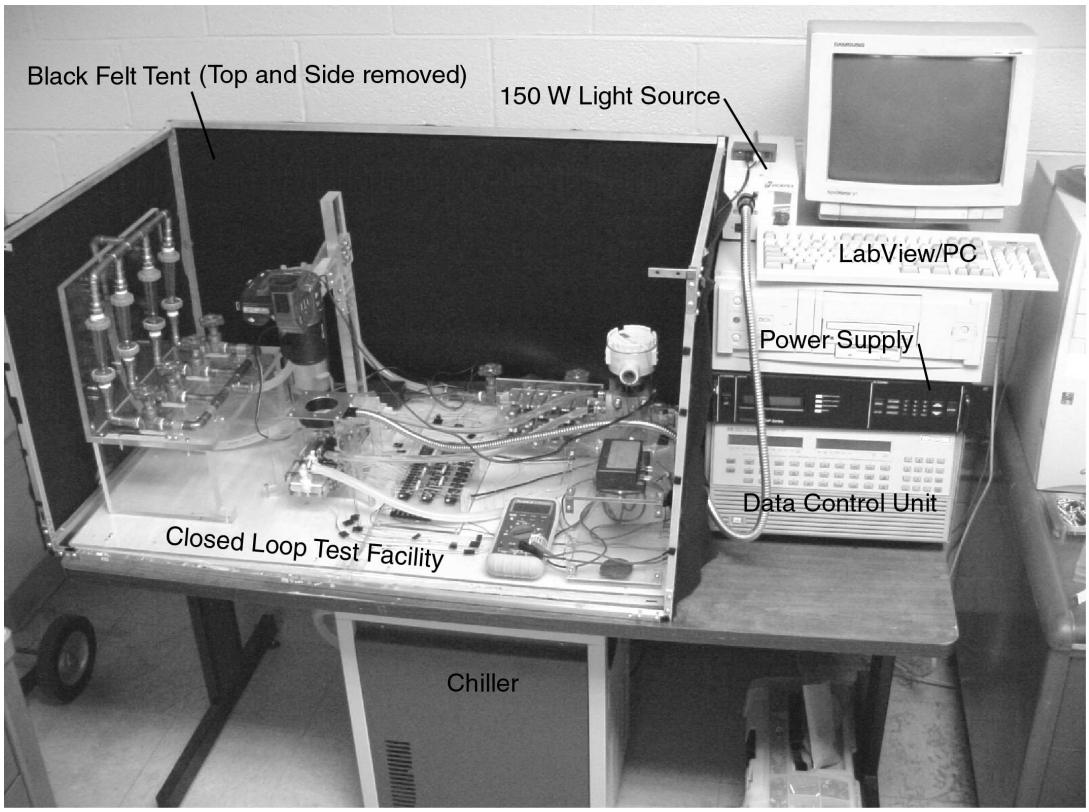

Figure 2.6: Photograph of full experimental set-up.

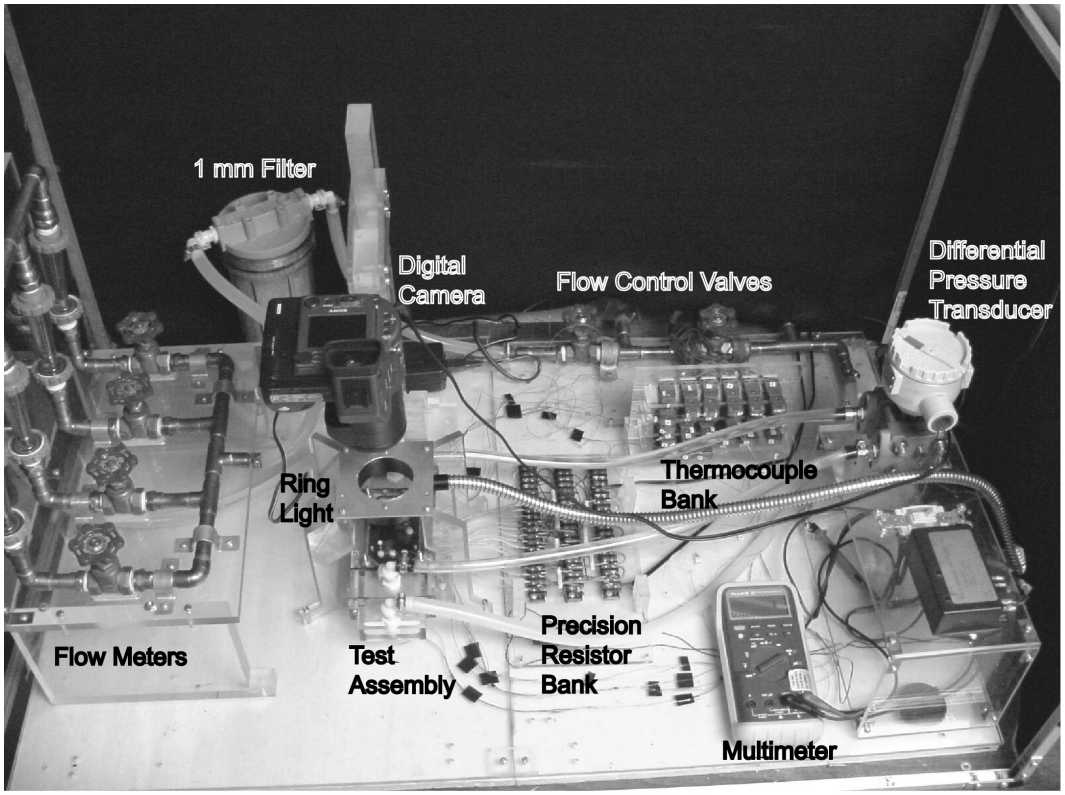

Figure 2.7: Close-up view of closed loop test facility and liquid crystal imaging set-up

A Sorensen DHP200-10 DC power supply provided electrical power to the heaters. A 1 Ω (±1 %) precision resistor was connected in series between the power supply and each cartridge heater. The current through each heater was determined by monitoring the voltage across its resistor. This, combined with the voltage measured across each heater was used to determine the total electrical power dissipation within the copper block as:

$$Q_H = \sum_{n=1}^{7} V_n I_n \tag{2.1}$$

Surface temperature measurements were made through the application of thermochromic liquid crystals. A Moritex Inc. fiber optic light source and ring light guide (models MLF-150L and MRG61-1500S respectively) were used to illuminate the array from above. The light source included a built in infra-red filter to mitigate heating effects. A Sony MD-95, digital camera aligned along the axis of the ring light captured the color response of the liquid crystal coated pin fin array. Still images were stored on a removable storage disk for later analysis. A tent with black felt walls enclosed the majority of the test facility to ensure that the ring light was the only source of illumination during testing.

In addition to the liquid crystals, base plate temperature measurements were made using six thermocouples, located just prior to and just following the pin array, as depicted in **Figure 2.1a** They were cemented to the base plate endwall using thermally conductive epoxy (Thermalloy Inc., #4952). Each of the six thermocouple wires was passed through a threaded connection in the assembly housing and sealed using a hard setting two-part epoxy. Another two thermocouples were cemented to the top of the base plate, just upstream and downstream of the heater, and three thermocouples were embedded into the heater block itself (see **Figure 2.3**). Two thermocouples in the inlet section and three in the outlet section measured the bulk fluid temperature. An additional two thermocouples were suspended in air within the enclosure to measure the ambient temperature. The temperature of the lab in which experiments were run was controlled by an air conditioning unit and typically did not vary by more than ±3 °C during a given experiment. A Labview controlled PC data acquisition system in conjunction with a Hewlett Packard 3852A data controller

recorded thermocouple temperature data to disk. Additional photographs and mechanical drawings of the experimental facility and the details of the test assembly design are included in **Appendix C**.

2.3 Calibration of Measurement Facilities

Equipment and set-up calibration comprised a major effort in this study. This ranged from the typical requirements of ensuring that the equipment for measuring temperature, pressure and flow rate were within their designated accuracy, and the more involved process of insuring that the liquid crystal temperature-to-color relationship was known and consistent, to the calibration of heat and pressure losses due to non-idealities in the test assembly and its boundary conditions. Detailed descriptions of each calibration process are given in the following subsections.

2.3.1 Thermocouple Calibration

0.127 mm diameter (36 AWG/0.005 in) copper-constantan (type T) thermocouples, in conjunction with a Hewlet Packard 3852A data acquisition system, were used to measure temperatures at discrete points within the test assembly. Calibration of the thermocouple-data acquisition system pair was performed at 0 ^{o}C using an ice bath. An insulated container was filled with a mixture of crushed ice and distilled water. A NIST traceable precision thermometer was used to monitor the temperature of the ice bath to within ± 0.05 ^{o}C. Thermocouples were placed into the ice bath with care taken to insure that all thermocouple beads were in contact with the ice-water mixture and not the sides of the container. Upon reaching steady state, measurements were taken at intervals of every five seconds over several minutes,

with a thermocouple attached to each channel of the data acquisition system. Results of the uncertainty analysis are provided in **Chapter 3**, with additional details provided in **Appendix B**.

2.3.2 Differential Pressure Transducer Calibration

The differential pressure transducer used to measure the pressure drop across the pin fin array employs a piezoelectric membrane between dual pressure ports that deflects when exposed to a differential pressure and produces a voltage signal proportional to the pressure difference. For calibration, one port of the transducer was exposed to a water column of known height, while the other port was exposed to atmospheric pressure. The pressure produced by the water column was calculated according to:

$$\Delta P = \rho_f g H_{wc} \tag{2.2}$$

where: ΔP = gauge pressure (Pa) = $(P - P_{atm})$

ρ_f = density of water (997 kg/m^3)

g = gravity constant (9.81 m/s^2)

H_{wc} = height of water column (m)

Measurements were performed at various water column heights and a highly linear relationship between differential pressure and the voltage signal from the transducer was observed as shown in **Figure 2.8**.

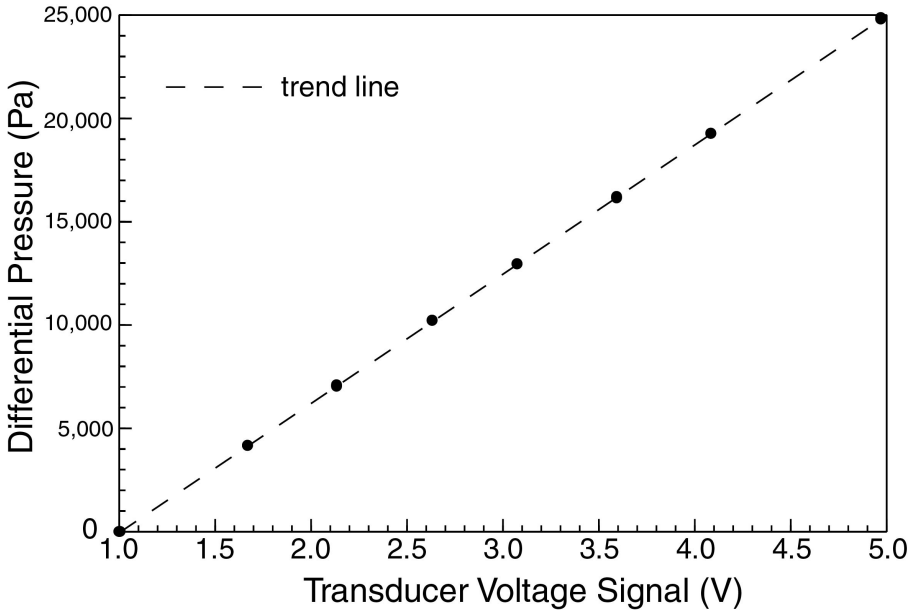

Figure 2.8: Differential pressure transducer calibration curve

During subsequent adiabatic pressure drop tests of the pin arrays, the transducer voltage was measured with a multimeter and the corresponding pressure was determined according to the relationship:

$$\Delta P = -6318 + 6257 V_{xdcr} \tag{2.3}$$

where: ΔP is the measured differential pressure (Pa)

V_{xdcr} is the transducer voltage (V).

Associated uncertainty in the differential pressure measurements is detailed in **Chapter 3** and **Appendix B**.

2.3.3 Flow Meter Calibration

Calibration of the three variable area flow meters was conducted with the cooling water at room temperature and no power applied to the base plate. With the

chiller pump active and the bypass valves set to obtain a specific flow rate through the test loop, cooling water was redirected downstream of the meter and collected in a separate container for a specific time period, ranging from 15 s to 120 s depending on flow rate. A graduated cylinder with an accuracy to within ± 5.0 ml was then used to measure the total flow volume (V) collected during the given period (t) and the apparent flow rate ($\dot{V}$) was determined as:

$$\dot{V} = \frac{V}{t} \tag{2.4}$$

A minimum of three trials was conducted for each major graduation mark on each flow meter. The average of each set of trials was then taken to be the representative flow rate for that mark. The calibration data for the three flow meters is presented in **Figure 2.9**. Least square linear curves were fit to each data set as follows:

Flow Meter	Calibrated Flow Rate Curve	
F-44250LH8	$\dot{V} = 0.97\dot{V}_{fm} - 0.020$	(2.5a)
F-375LH8	$\dot{V} = 1.122\dot{V}_{fm} - 0.27$	(2.5b)
F-376LH8	$\dot{V} = 1.043\dot{V}_{fm} - 0.037$	(2.5c)

$\dot{V}$ is the calibrated flow rate and $\dot{V}_{fm}$ is the flow rate reading based on the flow meter graduation marks. The given curve fits were used to determine flow rate during heat transfer and pressure drop trials. Calculations of volumetric flow rate uncertainty were made by the method of **Kline and McClintock (1953)**. The uncertainty analysis is summarized in **Chapter 3,** with additional details provided in **Appendix B**.

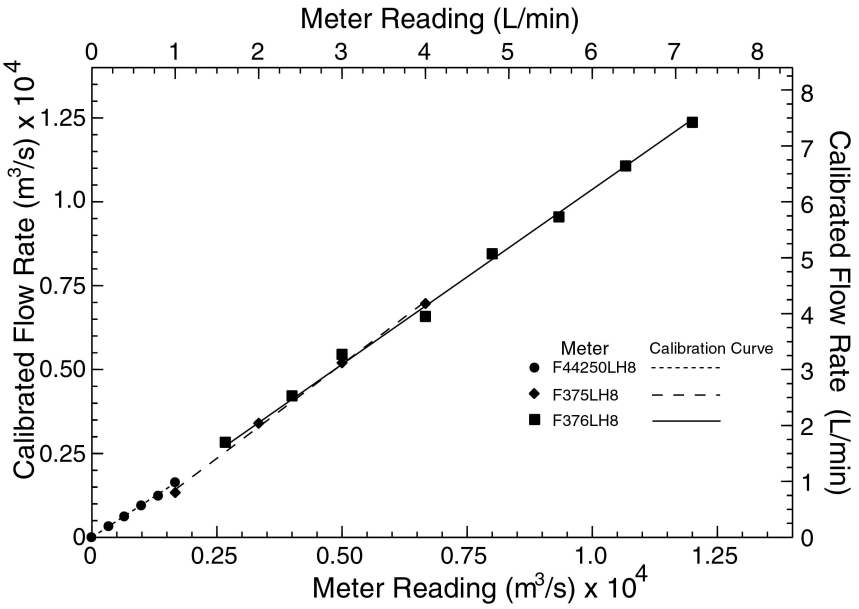

Figure 2.9: Calibration data for the three flow meters

2.3.4 Liquid Crystal Calibration

Thermochromic liquid crystals (TLC) are materials that exhibit a color change in response to a change in temperature. During the transition from a solid to a liquid state, the liquid crystal molecules twist and untwist, and in the process alter their reflective properties, causing a continuous change in observed color. Prior to and following this phase transition, the TLC are essentially transparent. Therefore, by applying a thin layer of liquid crystals with an appropriate transition range onto a heated surface, a global temperature field of that surface can be visualized and quantified through the color play of the coating.

However, the intensity of the illuminating light, the angle of illumination, the viewing angle, and even the age of the liquid crystal coating can all have a significant

effect on the color observed at a given temperature. For example, if viewed from directly above, the coated surface may be a dark blue, only to appear a definite shade of green when viewed from an oblique angle. To insure accurate temperature measurements, **Baughn et al. (1999)** strongly recommend that the temperature to color relationship of the liquid crystals be calibrated *in-situ* during an experiment such that these variables remain relatively constant between the calibration process and the actual experimental trials.

There are primarily two calibration procedures that are most often followed in the available literature. The first, known as the Successive Isotherm Method **(Hollingsworth et al., 1989)**, involves passing the calibration surface, which includes an array of thermocouples, through a series of temperature steps, with care taken to insure that the surface closely approximates an isothermal body at each temperature. The surface color is recorded at each step, and a calibration curve is generated defining the relationship between surface color response and the known surface temperature. The other primary method of choice is the Linear Gradient Method as employed by **Akino et al. (1989)** and others. In this approach the two ends of a plate are held constant at the high and low end of the TLC's temperature response range, thereby producing the full color spectrum across the plate in a single step. A line of thermocouples, embedded along its length is used to confirm the temperature profile across the plate. An image of the heated plate taken at steady state is then compared with that profile to determine an appropriate color vs. temperature relationship.

While this second approach is perhaps more elegant than the successive isotherm method, it is not well suited to the given scenario in this work due to the

geometry involved. That is, while it may be reasonable to treat heat transfer along the length of a flat plate as one dimensional, the same is not necessarily true in the case of a plate with an integral pin fin array as is considered here. For this reason, the first calibration approach was adopted.

In all cases, calibration was performed immediately prior to and immediately following a given experimental trial, with the illumination level, illumination angle, and viewing angle remaining effectively invariant during the entire process. The base plate pin fin array was first exposed to room temperature cooling water by operating the chiller for approximately one minute. This expelled air from the loop and charged the entire system with water at approximately 25 °C to 27 °C. After the pump was turned off and the array exposed to quiescent water, the heater block was powered on at a low level and the base plate temperature allowed to slowly rise from room temperature up to 36 °C – 38 °C over a period of approximately two minutes. At this point the heater was turned off and the base plate was allowed to slowly cool back towards room temperature.

Because the baseplate and heater block were well insulated, the vast majority of the stored heat must dissipate to the quiescent water via conduction and natural convection, or to the foundation by conduction. With the relatively low convection coefficients and fluid conductivities involved, the plate slowly cools through the liquid crystal activation range over a period of approximately 30 to 60 minutes. Under these conditions, the Biot number (Bi) is on the order of 0.01 or less, so the plate was expected to be highly isothermal during the cooling process. During this time, a series of digital photographs of the array was taken at approximately every 0.3 °C of

temperature drop, while the six thermocouples (locations shown in **Figure 2.1**) simultaneously recorded the plate temperature. The images and temperature data were then stored for later post-processing, the details of which are presented in **Chapter 3**.

2.3.5 Heat Loss Calibration

The ultimate goal of the thermocouple and liquid crystal temperature measurements was to characterize the heat transfer rates within the pin fin array through a range of flow conditions. In order to isolate the heat transfer specific to the array itself, it was necessary to quantify rates of heat transfer via all other thermal pathways including:

- Conduction to the foundation of the test assembly
- Natural convection from the test assembly walls
- Radiation from test assembly surfaces to the environment
- Forced convection from wetted surfaces of test assembly (other than the base plate)
- Forced convection from wetted surfaces of base plate outside the array

The first three were expected to be relatively minor with the final two somewhat more significant. To quantify the above losses, a series of calibration tests specifically intended to isolate these extraneous thermal pathways was performed. The following is a brief description of each calibration procedure. Details regarding the analysis of heat losses and the corresponding results are addressed in **Chapter 3**.

2.3.5.1 Extraneous Conduction, Natural Convection, and Radiation Losses

The test assembly was designed to minimize heat losses to the foundation through the use of low thermal conductivity materials such as Plexiglas and Styrofoam, and the inclusion of air gaps between sections of the assembly. This set of calibration tests involved operating the assembly in a dry state, with no fluid flowing through the system. In this configuration, the preponderance of heat input into the base plate must be dissipated by conduction through the foundation, by natural convection from the outer walls of the assembly, or by radiation from the surfaces of the assembly to the environment. Tests were conducted with the 2 mm pin fin base plate in place, through a range of input power levels (0.9 - 5.2 W). At each power level, the test was allowed to run for six hours or more to insure the system attained a steady state condition. This provided a known relationship between the average temperature rise of the heater block relative to ambient room temperature, and the total heat lost through conduction and natural convection from the assembly. Results of these tests are presented in **Chapter 3**.

2.3.5.2 Forced Convection Losses

Forced convection heat transfer was not limited to the pin fin array alone. The dotted line depicted in **Figure 2.1** represents the general location of the O-ring seal between the base plate and the lower section of the test assembly. The area inside this line is the wetted area of the base plate during testing. A portion of this area is outside the perimeter of the array itself. In addition, all wetted surfaces of the test assembly represent potential thermal pathways for the heat to convect directly to the cooling

fluid without passing through the pin fin array. This is particularly true of the aluminum housing section, which is in direct contact with the base plate. It has a high thermal conductivity and a significant amount of surface area which is exposed to the cooling fluid. To isolate the effect of these areas, a second series of calibration tests was performed using a specially constructed aluminum base plate with a relatively non-conducting pin array as illustrated in **Figure 2.10**.

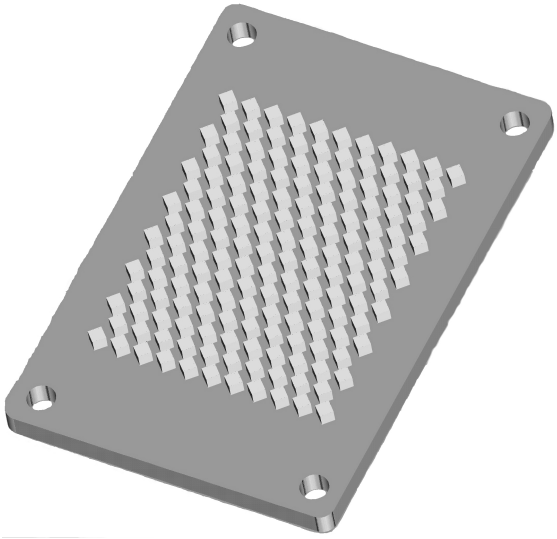

Figure 2.10: Model of forced convection heat loss calibration plate

A flat base plate of aluminum was fabricated and a 2 mm deep volume of material was milled away from the center section of the plate corresponding to the location of the pin fin array. The hollowed out section was then partially filled in with a hard setting epoxy of low thermal conductivity, which was subsequently milled flat. A pin fin array, machined from Plexiglas was then attached to the aluminum plate

using silicone adhesive. Constructing tapered cylindrical pin fins like those of the AlSiC base plates was not feasible. Therefore, an array of diamond shaped pin fins of approximately equivalent geometry was milled from a Plexiglas block. While not an exact replica, it was felt that this would produce a similar flow field as seen with the AlSiC base plate while excluding heat transfer from the array, thereby isolating heat transfer to the rest of the wetted surfaces of the test assembly. Because of differences in thermal conductivity between the AL6063 aluminum alloy plate (200 W/m^2K, J.E Sergent, A. Krum, 1998) and the AlSiC baseplate (160 W/m^2K), the calibration plate was made 6.25 mm thick, compared to the 5 mm thickness of the AlSiC base plate. This provided a consistent overall thermal resistance between the two plates. To limit the number of calibration runs required, a set of three experimental runs was conducted. Trials were completed for the following combinations:

- H/D = 1.1, C = 25 %
- H/D = 0.8, C = 12 %
- H/D = 0.5, C = 0 %

with the first and last cases representing the extremes in flow area. The same Plexiglas array was used by re-machining it to a lower pin height after each trial. The tests produced a set of calibration curves relating heat transfer rate to the temperature rise of the heater block relative to the mean cooling fluid temperature, as a function of fluid flow rate. Results from the calibration procedure are presented in **Chapter 3** along with details on how the information is applied to correct for heat losses.

2.3.6 Pressure Loss Calibration

As depicted in **Figure 2.3**, the pressure ports were located upstream and downstream of the base plate. Bends and constrictions in the flow path contributed to the overall pressure drop measured between the two ports in addition to that generated by the array itself. This necessitated another set of calibration trials as well. A series of runs was made employing a flat aluminum base plate mounted onto the test section in place of the AlSiC base plate. The measured pressure drop in this case is due exclusively to constriction and frictional losses associated with the open channel itself. These results were then used to distinguish between the total pressure drop measured during primary testing, and the portion that was attributable to the array itself. As with heat transfer calibration, data reduction details and the calibration curves themselves are provided in **Chapter 3**.

2.4 Experimental Procedures

The following subsections detail the procedures followed during specimen preparation and the implementation of experimental trials.

2.4.1 Liquid Crystal Preparation and Application

A formulation of C20-10 microencapsulated liquid crystals, AQB-3 binder, and BB-M1 black backing paint from Hallcrest Inc. was used. These particular formulations were chosen because both the liquid crystal slurry and the black backing paint are purported by the manufacturer to have moderate water resistance.

The process of liquid crystal preparation and application employed here is based on that used by **Farina et al. (1993)**. The liquid crystal slurry and binder were combined using a hand-held motorized mixer. A standard paper coffee filter was then used to filter out any large clumps of liquid crystals not fully mixed into the liquid binder. Several studies have noted that such a filtering technique is insufficient. However, it proved to be adequate in this study as is evidenced by the quality of images produced. The filtration process typically took several hours, and resulted in the fine suspension of liquid crystals needed for a streak-free TLC image. In addition, the black backing was diluted at approximately 1:1 (by volume) with distilled water.

The base plates were first cleaned with soap and water and then with pure Ethyl alcohol using a toothbrush. Once dry, the base plates were coated first with the black backing paint using an artist's airbrush (Aztek Inc., model A320) with a 0.40 mm nozzle installed. The black backing is used to provide a uniform, low hue value background, against which the liquid crystal color reaction can be viewed. A smooth, even motion was used to apply a consistent and uniform coating on the base plates. This consisted of passing the brush over the base plate from left to right, then right to left. This was followed by motions from top to bottom and vice versa. Finally, a diagonal motion from corner to corner was used to coat the plates from all angles so that all sides of the pin fins and endwall would be coated relatively equally. This process was repeated until each plate was uniformly covered, waiting several minutes between each coating to allow the paint to dry. In a similar manner, the liquid crystal suspension was applied over the black backing. A total of four coats each of black backing paint and liquid crystal were applied to each plate to maintain consistency.

No attempt was made to characterize the actual thickness of the coatings. Once the base plates were again fully dry, they were protected with bubble wrap, placed in individual zip-lock plastic bags and stored out of the light until they were needed.

2.4.2 Heat Transfer Measurements

Heat transfer tests were conducted on each base plate through a range of operating conditions as summarized in **Table 2.2**. Each of the three base plates was tested at a nominal tip clearance (C) of 0, 6, 12, 18, and 25 percent, where C is expressed as a percentage of pin fin height.

Table 2.2: Heat transfer test conditions

Pin non-dimensional height – H/D:	0.5, 0.8, 1.1
Nominal clearance – C (%):	0, 6, 12, 18, 25
Nominal Reynolds number - Re:	$2 \cdot 10^2$ - $1 \cdot 10^4$
Flow rate - $\dot{m}$ (kg/s):	$3.3 \cdot 10^{-3}$ - $1.2 \cdot 10^{-1}$ [$\dot{V} = 0.2$ – 7.2 L/min]
Heater input - Q_H (W):	59 - 888
Heat flux $\dot{q}''_H$ (W/cm^2):	1.6 – 24.4

Prior to each trial, the test assembly was adjusted to achieve the desired clearance. The insert depth (z), which is shown in **Figure 2.4**, was measured at nine points on the assembly using a Mitutoyo series-229 depth micrometer. This depth is the distance between the lower face of the aluminum housing section upon which the endwall of the base plate is mated, and the face of the plexiglas insert. The difference between this distance and the height of the pins is the tip clearance. The average of the nine clearance measurements was taken to be the representative clearance for the

plate. These average clearances (C) and the standard deviation (σ) among the nine measurements are given in **Table 2.3** and are reported as percent of pin height.

Table 2.3: Measured tip clearances during heat transfer tests

H/D	Nominal Clearance (%)	6	12	18	25
0.5	Average Measured Clearance -C_{meas} (%):	7.2	12.6	18.4	25.5
	Standard Deviation -σ (%):	±0.6	±0.5	±0.6	±0.6
0.8	Average Measured Clearance - C_{meas} (%):	5.5	11.1	18.2	25.2
	Standard Deviation - σ (%):	±0.7	±1.2	±0.9	±0.7
1.1	Average Measured Clearance - C_{meas} (%):	6.2	12.2	18.2	27.2
	Standard Deviation - σ (%):	±0.6	±0.7	±1.0	±1.5

Each clearance case was tested at ten flow rates within the given Re range at a constant nominal inlet temperature of 27 °C (± 1 °C). For each flow rate, a heat flux was applied which resulted in a 3 °C - 9 °C base plate temperature rise, thereby producing a base plate temperature within the observed 31 °C to 36 °C color band of the liquid crystal coating. For each combination of heat flux and flow rate, thermocouple measurements were used to determine when steady state had been achieved. In reality, this was a quasi steady state, since the inlet fluid temperature would change periodically by ± 1 °C, as the chiller turned on and off around its set point. This period was approximately on the order of five to ten minutes. Upon reaching this steady state, a series of three digital photographs was taken of the pin fin array, once every thirty seconds. For each image, corresponding thermocouple measurements were recorded, including inlet and outlet fluid temperature, ambient room temperature, eight discrete points on the base plate, and three points within the heater block.

During each test run, half the flow rates were repeated in random order at heat fluxes approximately ten percent higher or lower than used initially, to confirm repeatability of heat transfer results. In addition, twenty percent of the clearance cases were repeated after completing the initial test matrix.

2.4.3 Differential Pressure Measurements

Adiabatic pressure drop measurements were performed separately from the heat transfer tests. Trials were conducted at room temperature (25 °C to 27 °C), through the full range of Reynolds numbers and tip clearance shown in **Table 2.2**. Tip clearances used during pressure measurements were similar but not exactly the same as those during heat transfer testing due to limitations in set-up precision. The actual measured values are shown in **Table 2.4.**

Table 2.4: Measured tip clearances during differential pressure drop tests

H/D	Nominal Clearance (%)	6	12	18	25
0.5	Average Measured Clearance - C_{meas} (%):	6.6	13.0	18.8	25.8
	Standard Deviation - σ (%):	±1.1	±1.1	±0.9	±0.9
0.8	Average Measured Clearance - C_{meas} (%):	6.4	12.6	17.9	24.9
	Standard Deviation - σ (%):	±0.2	±0.4	±0.3	±0.4
1.1	Average Measured Clearance - C_{meas} (%):	6.2	12.1	18.3	25.1
	Standard Deviation - σ (%):	±0.1	±0.5	±0.3	±0.4

Chapter 3: Data Analysis and Reduction

Because of the basic nature of much of the collected data, a significant effort in data reduction and analysis was required. This included post-processing of the liquid crystal image data to obtain corresponding temperature results, as well as incorporating test assembly calibration data to accurately discriminate between actual pin fin array behavior and outside influences. The following sections provide detailed descriptions of the data analysis and reduction methods used, concluding with an analysis of uncertainties in the data to be reported in **Chapter 4**.

3.1 Liquid Crystal Image Processing

There are a number of different ways in which color can be represented analytically. The images produced by the digital camera in this study are based on the RGB system of color representation. In this system, all colors are represented by a combination of three primary colors; Red, Green and Blue. Each primary color is assigned a relative strength ranging from 0 to 255, with 0 indicating a complete absence of that color, and 255 the maximum concentration. When none of the three primaries is present [(R(0), G(0), B(0)], the resulting color is pure black. When all three colors are present in full concentration [R(255), G(255), B(255)], the result is pure white. In all, this system can produce 256^3 or nearly 16.8 million combinations of red, green and blue. However not every combination results in a unique color. Very different combinations of the three primaries can be combined to produce what appears to be the same color as discerned by the human eye. This makes the RGB

system a poor choice for characterizing the temperature verses color response of liquid crystals.

Another way of representing color is the HSV or HSI system. Like RGB, it relies on a combination of three primaries; in this case Hue, Saturation and Value (Intensity). In this system, Hue corresponds to the dominant wavelength of light associated with a given color, which spans the spectrum from red, through orange, yellow, green, blue, indigo, and violet. Saturation describes the level of purity of hue, while Value defines the "lightness" or degree of whiteness and blackness. This approach was common to the broadcast industry prior to the digital age. For instance, looking at the back of an older model color television set, one will generally find a set of three knobs enabling one to adjust the Hue, Saturation, or Intensity (Value) of the picture to fine tune color quality.

What makes HSV a more appropriate system for the characterization of TLC color-to-temperature behavior is the fact that under controlled conditions, the saturation and intensity components remain relatively invariant throughout the color play of the liquid crystals. In other words, only the hue value changes. This is not the case in the RGB system. More importantly, hue has long been shown to vary monotonically through this range. As a result, a given color within the TLC color band can be associated with a unique hue value. Through careful calibration, a hue verses temperature relationship can be generated so that any given TLC color can be related to a corresponding temperature.

While there are other approaches that can be used to generate the color verses temperature relationship, the hue based calibration technique has become the most

prominent means of calibrating and analyzing liquid crystal images. To employ this approach here, it was necessary to convert the RGB data of the digital images that were recorded during the experimental trials, into corresponding HSV values.

The RGB system is based on a rectangular coordinate system as shown on the left-hand side of **Figure 3.1,** while the HSV system is defined through a cylindrical or conical coordinate system illustrated on the right-hand side of **Figure 3.1**.

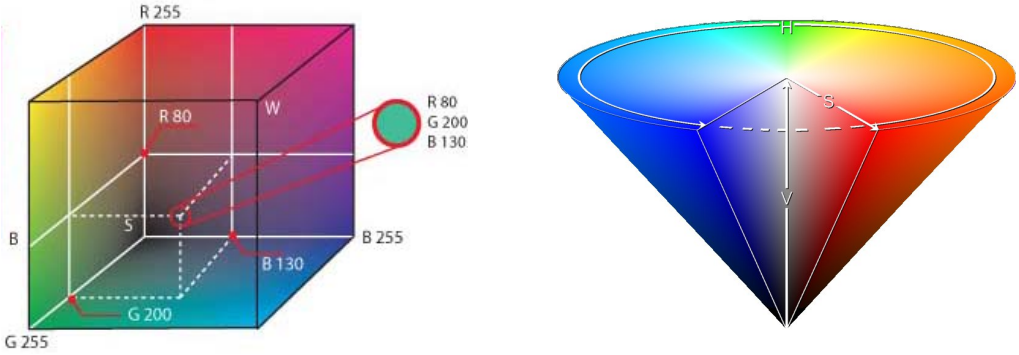

Figure 3.1: RGB rectangular color space[1](left), HSV conical color space[2](right)

The relationship between the two systems, while not intuitively obvious, can be described geometrically as shown in **Figure 3.2**. The illustration on the left shows a point P located somewhere in RGB space. Triangle (abc) represents a plane with normal in the (R = G = B) direction and which intersects point P. If a line normal to the plane is extended out from the origin O, it will intersect the plane at point (n) as shown in the illustration on the right. The angle between line (np) and line (na) is the hue angle.

[1] Image obtained from open-source internet based wikipedia entry "RGB Color Space".
[2] Image obtained from open-source internet based wikipedia entry "HSV and HSL"

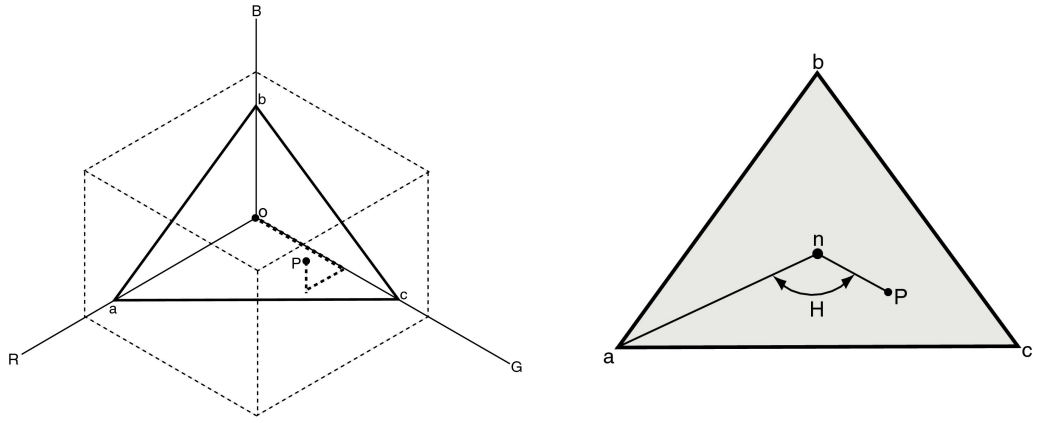

Figure 3.2: Relation between RGB color space and Hue angle. [Ireland and Jones, 2000]

According to **Ireland and Jones (2000)**, the hue angle (H) can be calculated by:

$$\cos(\mathsf{H}) = \frac{2R - G - B}{\left\{ 6\left[(R-V)^2 + (G-V)^2 + (B-V)^2 \right] \right\}^{1/2}} \tag{3.1}$$

A number of different definitions have been employed in the open literature which take advantage of the intensity (Value) being relatively invariant in TLC applications, modeling the hue angle as a function of R, G, and B values only. Separate definitions of hue have been proposed by **Hollingsworth (1989)**, **Farina (1993),** and **Baughn (1999)**, to name a few. But no one definition has been shown to be universally more appropriate than the others. **Hay and Hollingsworth [1996]** examined three candidate definitions and based on the combination of test results and computational simplicity, they recommended:

$$H = \tan^{-1}\left(\frac{\sqrt{3}(G-B)}{2R-G-B}\right) \tag{3.2}$$

In this study, a similar definition was employed using the scientific computing software package Matlab. The image-processing library of Matlab includes the function RGB2HSV. As described by **Baughn et al [1999]**, this function is based on the algorithm:

If R > G and G > B $$H = \frac{G-B}{6(R-\min(R,G,B))} \tag{3.3a}$$

Else if G > B $$H = \frac{2+B-R}{6(G-\min(R,G,B))} \tag{3.3b}$$

Else $$H = \frac{4+R-G}{6(B-\min(R,G,B))} \tag{3.3c}$$

which compares to within 0.3 percent of equation (3.2).

3.1.1 Processing Of Calibration Data

In this study, only nine interior rows (out of 15) and nine columns (out of 21) of the base plate, consisting of 49 individual pin fins are considered. This area is depicted in **Figure 3.3** as the light-shaded pins. All test data and subsequent analyses were restricted to this region of the base plate. This helps to insure that leading edge, trailing edge, and sidewall effects were minimized by a substantial degree. The results

obtained here are therefore expected to correspond to the fully developed region of a pin array.

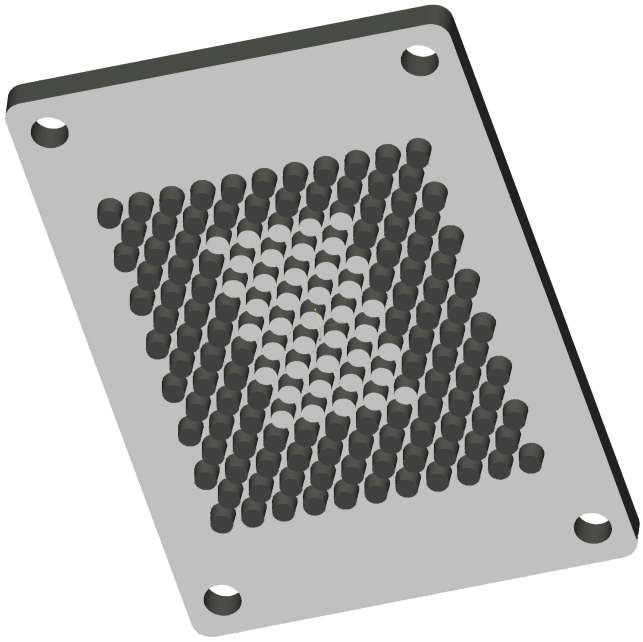

Figure 3.3: Pin array region included in analysis (lighted area in center). Flow direction is from bottom to top

As noted in **Chapter 2**, each heat transfer trial was proceeded by and ended with a calibration period to obtain a unique relationship between liquid crystal hue values and corresponding surface temperature. Each recorded image was post-processed using a series of Matlab based software routines. **Figure 3.4** shows a typical, raw TLC image (unheated array) depicting the pin fin array as viewed by the digital camera. A dashed line, overlapped onto the image depicts the region of interest (ROI) from which liquid crystal data is processed and analyzed. This region corresponds to the light-shaded pins depicted in **Figure 3.3.**

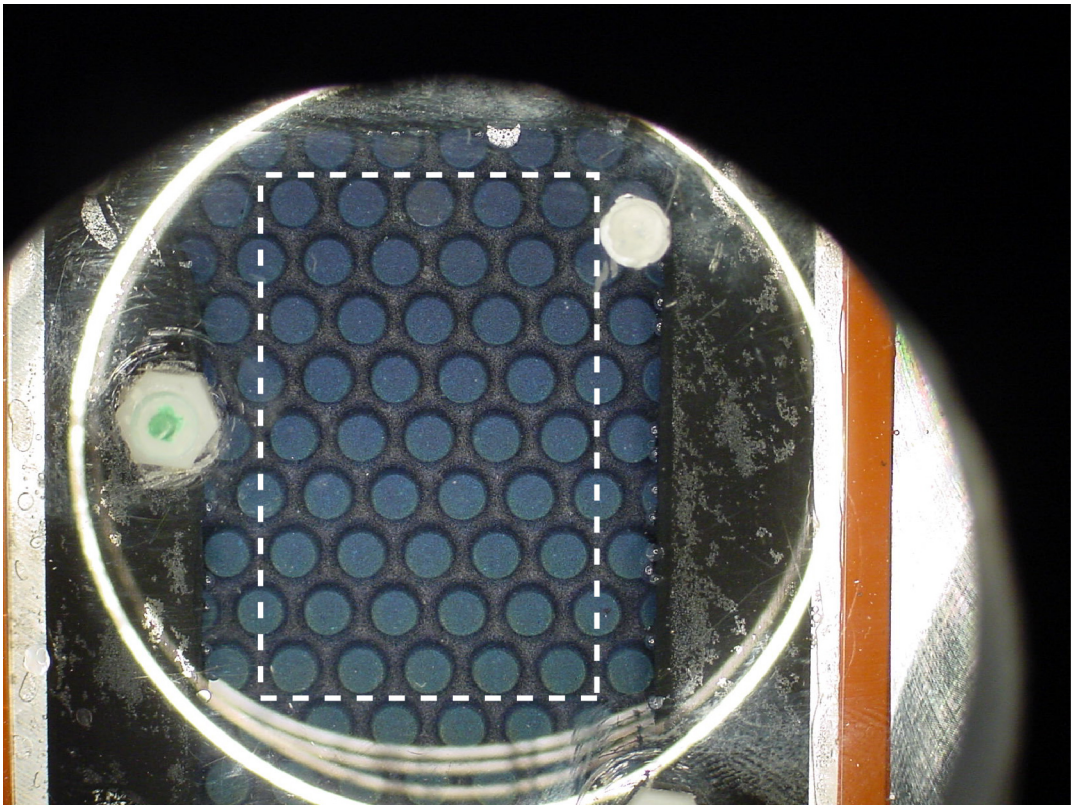

Figure 3.4: Typical liquid crystal image with demarcated region of interest

Each such image was processed by first cropping the image so that only the ROI remains. **Figure 3.5** presents one such typical image. The ROI is then partitioned into (49) separate "unit cells", each consisting of a single pin fin along with its associated endwall area. Those cells are depicted in **Figure 3.5** shown with an "x" drawn thru them for highlighting purposes. The partial unit cells on the left and right hand sides without an "x" are not included in the TLC based analysis. A row and column mapping convention is also shown in **Figure 3.5** for the purpose of identifying individual unit cells within the array.

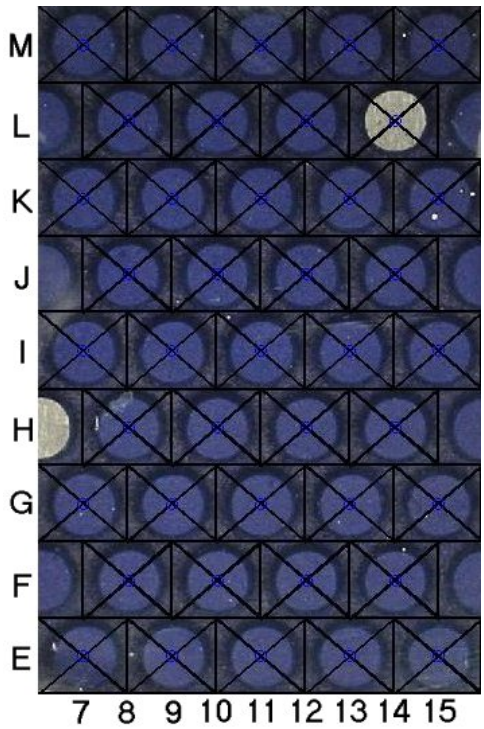

Figure 3.5: Typical ROI during calibration, subdivided into 49 separate "unit cells"

Separate binary masks are then applied to segregate endwall areas from pin tip areas and to eliminate "visual anomalies" from the field of view prior to analysis. Two such example masks are shown in **Figure 3.6**. The left-hand image is a pin tip mask. It is overlaid onto the ROI image and only pixels corresponding to white regions of the mask are considered in subsequent pin tip analysis. Each tip area within the mask is slightly smaller than the corresponding tip area in the ROI image to insure that only regions perpendicular to the line of sight are included, thus eliminating edge effects. The mask is also used to eliminate regions that are uncoated or exhibit some other anomaly. For example, in **Figure 3.5**, unit cell L-14 contains a pin tip that was left uncoated by liquid crystals or black backing paint in order to act as a point of reference within the array. It can be seen that the corresponding pin tip mask in **Figure 3.6** does not include a tip region in this cell, thus eliminating the uncoated pin

from consideration. In addition, each set of ROI images contain a limited set of anomalies. For instance, unit cell K-15 in **Figure 3.5** contains a number of bright white dots, as do several of the other unit cells. These dots are the result of air bubbles. These bubbles are not traveling within the cooling fluid, but rather are trapped within the region between the Insert and the Plexiglas housing as shown in **Figure 2.4**. While care was taken to mitigate the occurrence of these bubbles during the initial charging of the closed loop system with water, they could not be eliminated entirely. Similarly, unit cell H-8 exhibits a "smudge" near the top of the pin tip due to a stray deposit of silicone adhesive on the face of the insert. These anomalies, if included in subsequent processing would bias the hue analysis significantly, and thus are eliminated by way of the mask, which is custom constructed for each set of trial data.

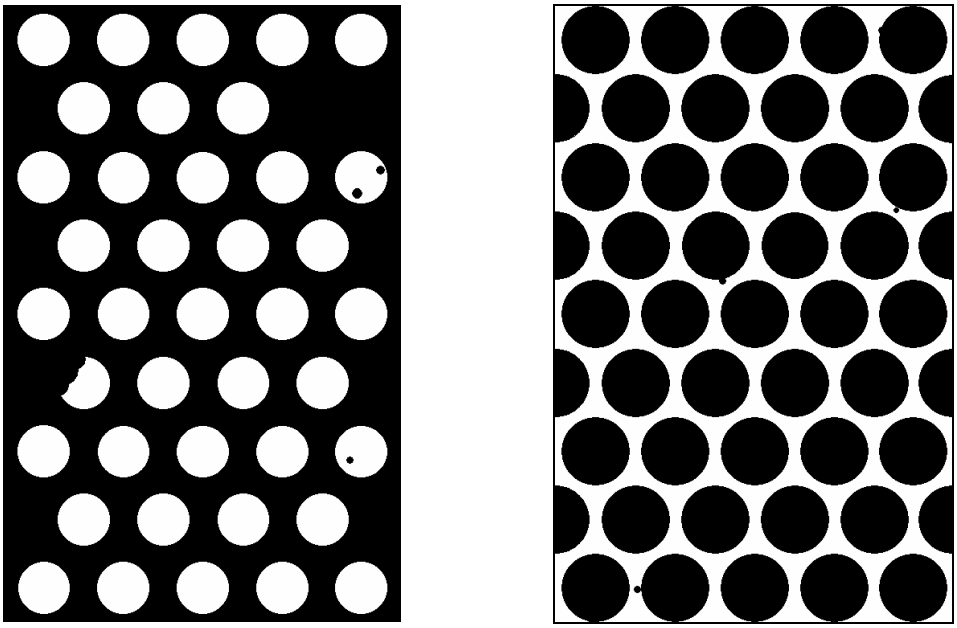

Figure 3.6: Binary masks for the pin tip regions (left) and endwall regions (right).

In like fashion, an endwall mask as shown on the right-hand side of **Figure 3.6** is applied to define the relevant endwall area for analysis. In this mask, the eliminated (black) areas are slightly larger than the base of the pin fins in order to avoid shading effects or analysis of surfaces not perpendicular to the line of sight.

Based on the partitioning and the binary masks, mean hue values are calculated separately for the endwall area and the tip area for each unit cell, converting RGB values of each pixel to a corresponding hue value by employing the algorithm described in **Equations 3.3a – 3.3c**. On average, each pin tip area, after the application of the binary mask, consists of approximately 3500 pixels while each endwall region contains roughly 1200 pixels, with each pixel being roughly 50 μm square. By comparison, the typical unit cell contains about 8500 pixels in total, prior to the application of the mask sets. This conversion is performed on each calibration image, which in turn is associated with a mean baseplate temperature as defined by the six endwall thermocouples. The result is a set of (98) calibration curves (one endwall and one pin tip curve for each of 49 unit cells) associated with each heat transfer test trial. Given that tests were conducted for three values of H/D and five values of C for a total of fifteen test trials, this resulted in a total of 1470 individual calibration curves for the full study.

Figures 3.7 – 3.9 present sample calibration curves for H/D = 0.5, 0.8, and 1.1 respectively. While the center pin (I-11) has been used to illustrate the calibration data, these results are not unique. The other 48 pins within the array produced similar results to those shown.

The graph on the upper-left of each figure shows the raw data for both the initial and the final calibration runs across the full temperature range of the liquid crystal coating. In each case, there is excellent agreement between the runs, indicating the calibration data to be relatively invariant over the duration of the given heat transfer experiment. As is common with liquid crystal behavior, the calibration curves exhibit a relatively flat plateau towards the upper temperature range of the TLC, transitioning to a steeper decline in hue with decreasing temperature. Near the low end of the temperature range, a fairly abrupt reversal in hue values occur as the TLC transitions back to its transparent state and the background hue value of the black backing dominates.

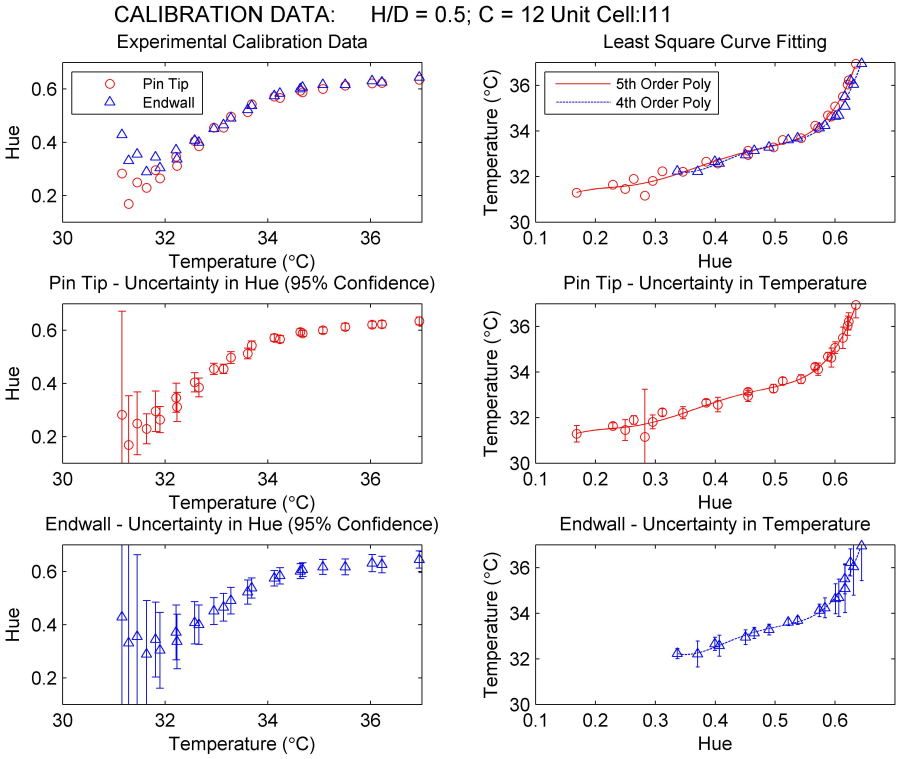

Figure 3.7: Sample Calibration curves and least square curve fits to data H/D = 0.5

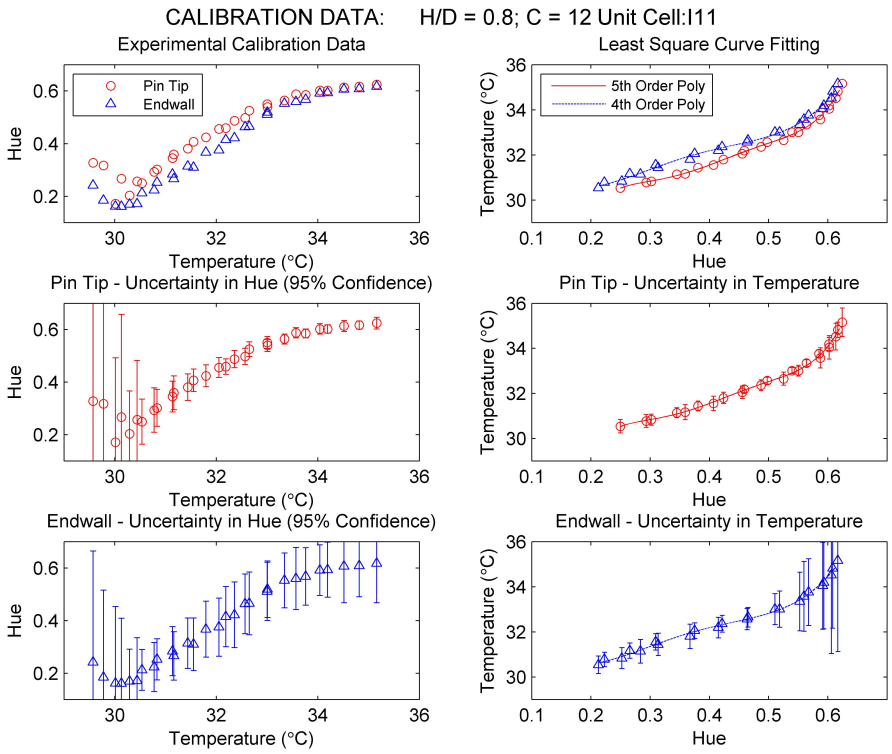

Figure 3.8: Sample Calibration curves and least square curve fits to data H/D = 0.8

For the case of H/D = 0.5, the pin tip and endwall data follow the same behavior, overlapping one another. However, as H/D increases to 0.8 and 1.1, the calibration tests produce increasingly separate profiles between the pin tip region and the endwall region. It is believed that this is due to differences in the quality and uniformity of TLC coverage along the endwall between aspect ratios. While care was taken to try and coat the entire pin fin array evenly and uniformly as noted in **Chapter 2**, it is evident from these results that the process was not adequate to fully overcome the shadowing effect of the taller pins, thus resulting in a less than complete coverage of the endwall areas at the higher aspect ratios. One would expect the consequence of such an incomplete coverage to be an increasingly downward bias in mean hue value as the number of pixels exhibiting TLC based hue responses

decreases, and the number of pixels exhibiting the black backing based hue response increases. This is in fact what was observed with increasing H/D.

This coverage issue is also reflected in the increasing level of uncertainty in hue level with aspect ratio as shown in the center-left and lower left graphs of **Figures 3.7- 3.9**. These graphs depict separate re-plots of the pin tip and endwall data, with estimated uncertainties based on the 2σ variation in hue calculated for all pixels within the given region. The pin tips exhibit relatively little change in uncertainty between aspect ratios as would be expected since they would not be subject to shadowing effects. The endwall region on the other hand, exhibits a strong relationship between aspect ratio and the degree to which hue varies from pixel to pixel. While these variations reduce the ability of the TLC technique to predict accurate local temperatures with pixel level resolution, it does not impact the studies ability to produce accurate unit-cell level temperature measurements, as the mean value of hue across a given unit cell remains uniform and consistent, being a strong function of temperature.

The graph at the upper-right of each figure presents the calibration data with hue as the independent variable and a least square polynomial curve fit to each set of data. A fifth order polynomial was found to provide an excellent match to the pin tip data. In some cases, such as that shown in **Figure 3.7**, the viable range of hues for the endwall regions was somewhat limited, which in turn reduced the number of data points. In these cases, the limited amount of data was ill-suited to produce a fifth order polynomial. For this reason, and in order to remain consistent between test trials, all endwall data was fit with a fourth order polynomial. In both cases, the

degree of data scatter relative to the polynomial fit is extremely low. Also, in order to maintain the highest level of accuracy possible, the application of each polynomial is limited to the central section of the Hue-Temperature curve, above the hue reversal point at the low end of the temperature range, and below the plateau that occurs at the high end of the temperature range.

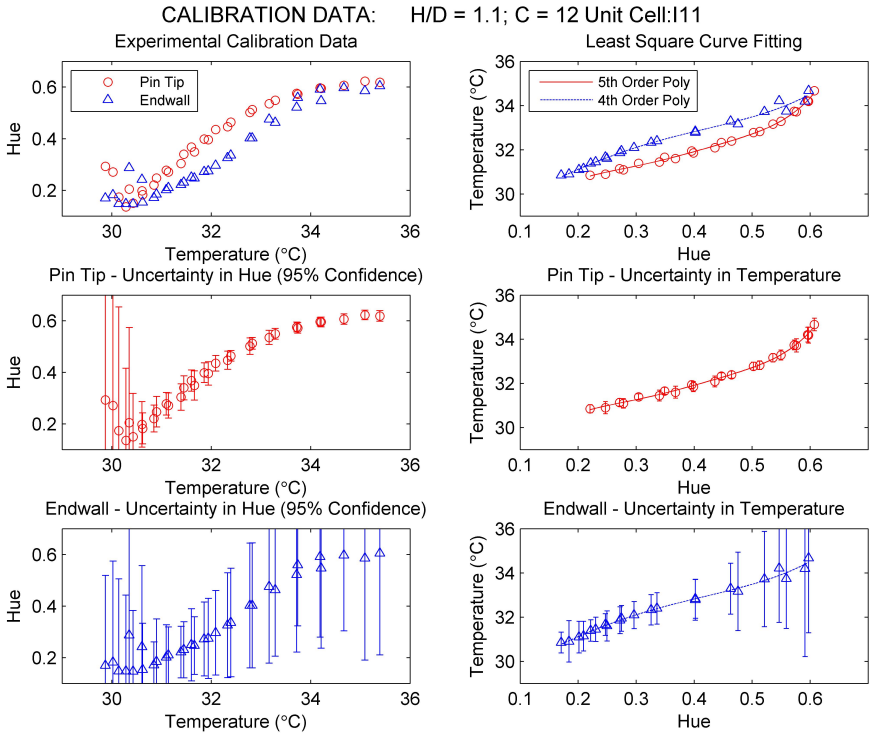

Figure 3.9: Sample Calibration curves and least square curve fits to data H/D = 1.1

The center-right and lower-right graphs re-plot the pin tip and endwall calibration data separately, along with estimated uncertainties in temperature. These temperature uncertainties were determined by applying the limits of hue uncertainty to the assumed curve fits. Because uncertainty in pixel level temperatures increased significantly with an increase in H/D, quantitative results in this study have been

limited to the resolution of the unit-cell and the averaged hue values of that cell rather than individual pixel level hue values. As such, the uncertainty associated with the reported results is comprised of the temperature uncertainty associated with the thermocouples used to determine the baseplate temperature for each calibration point, and the Standard Estimate of Error (SEE) associated with the use of a least square curve fit to represent the hue vs. temperature behavior across the entire temperature range, where SEE is defined as:

$$SEE = \sqrt{\frac{\sum (Y - Y')^2}{N - P}} \tag{3.4}$$

where: Y = experimental value

Y' = predicted value from polynomial

N = Number of observations

P = Order of polynomial fit

The maximum level of liquid crystal based temperature uncertainty is summarized in Section 3.5.

3.1.2 Background Color Shift

As noted earlier, each heat transfer test trial was comprised of an initial calibration run, followed by the primary heat transfer tests performed through a range of flow rates and associated heat fluxes, and finally a second calibration run to reconfirm the TLC hue-temperature behavior. This series of tests typically took between three to four hours to complete. During that time, the black backing paint was observed to take on a subtle milky blue tint when in the non-heated state. It is believed that this was due to the absorption of water into the black backing layer

which was described by its manufacturer as moderately water tolerant, but not water-proof. While this color change did not have a significant impact on the test results, as is evidenced by the calibration data, steps were taken to record this behavior in order to quantify the degree to which this color shift was affecting the underlying hue behavior of the baseplates. The background color shift was tracked through time by photographing the baseplate in the unheated state. Upon taking three photos of the array at a given flow rate and heat flux, the power to the heater block was cut off and the plate was allowed to cool well below the limit of the liquid crystal color range, and then the array was photographed. This was repeated at each flow rate, throughout the course of the given test trial.

The degree to which this color shift occurred, varied from trial to trial. However in each case, the end result was a modest upward shift in background hue. **Figure 3.10** depicts a typical case of background color change (H/D = 0.5; C = 0). Over the length of the heat transfer trial, the baseplate experienced an average increase in background hue of approximately ten percent. This increase was not strictly monotonic over time, but on average appears to be roughly linear in nature. While this shift was not overly detrimental in this particular study, care would have to be taken in studies of longer duration.

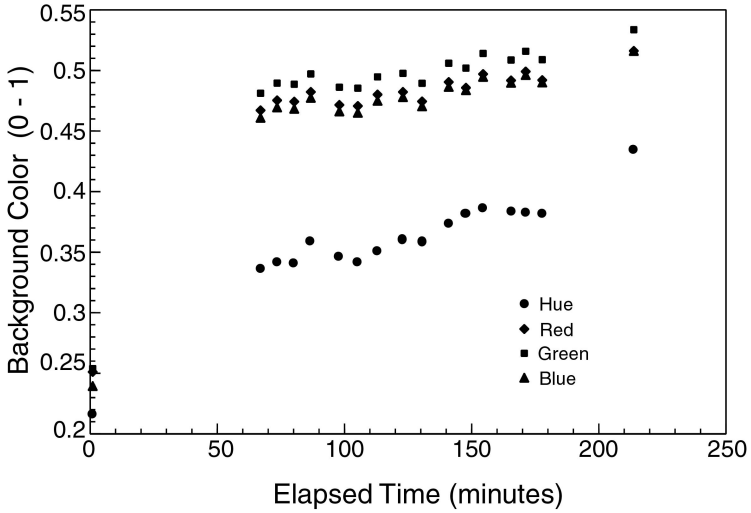

Figure 3.10: Variation in pin array background color over time

3.2 Correcting for Thermal and Hydrodynamic Losses

In order to arrive at meaningful results regarding heat transfer from the pin fin array, it was necessary to account for the various heat and pressure drop losses inherent in the test facility. To quantify the actual amount of heat being dissipated through the array, the test assembly was considered as a thermal circuit, with a trio of parasitic thermal resistances acting in parallel as illustrated in **Figure 3.11**.

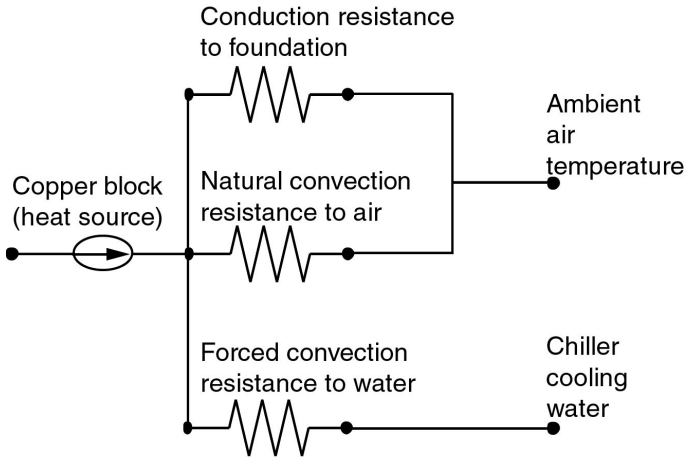

Figure 3.11: Schematic depiction of thermal losses from the test assembly

The heat loss associated with conduction, natural convection, and radiation ($Q_{L,cond}$) was determined through calibration tests as outlined in **Section 2.3.5**. The results of these tests are presented in **Figure 3.12**. A least square linear curve fit to the conduction loss calibration data gave:

$$Q_{L,cond} = 0.242(T_H - T_{amb}) \tag{3.5}$$

where: T_H is the average heater block temperature

T_{amb} is the average recorded ambient air temperature

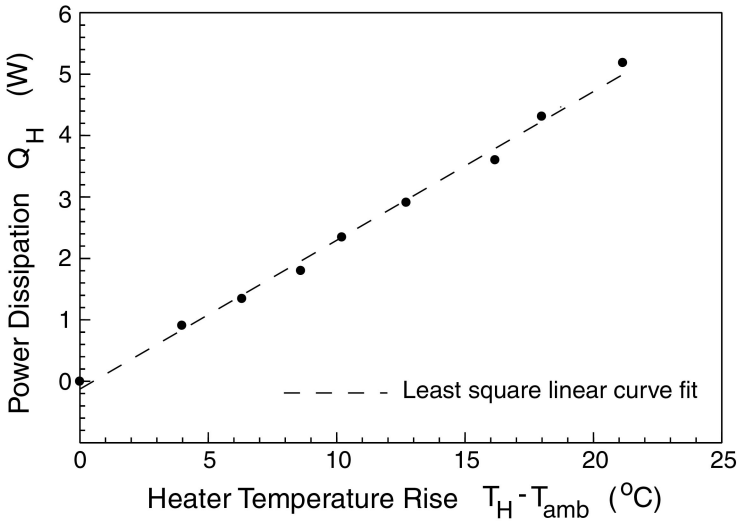

Figure 3.12: Conduction and natural convection heat loss calibration curve

From the calibration tests discussed in **Section 2.3.5.2**, forced convection losses ($Q_{L,conv}$) were found to be an extremely linear function of the difference between heater block temperature and average fluid temperature for a given flow rate. Results for each of three test cases considered are shown in **Figure 3.13**.

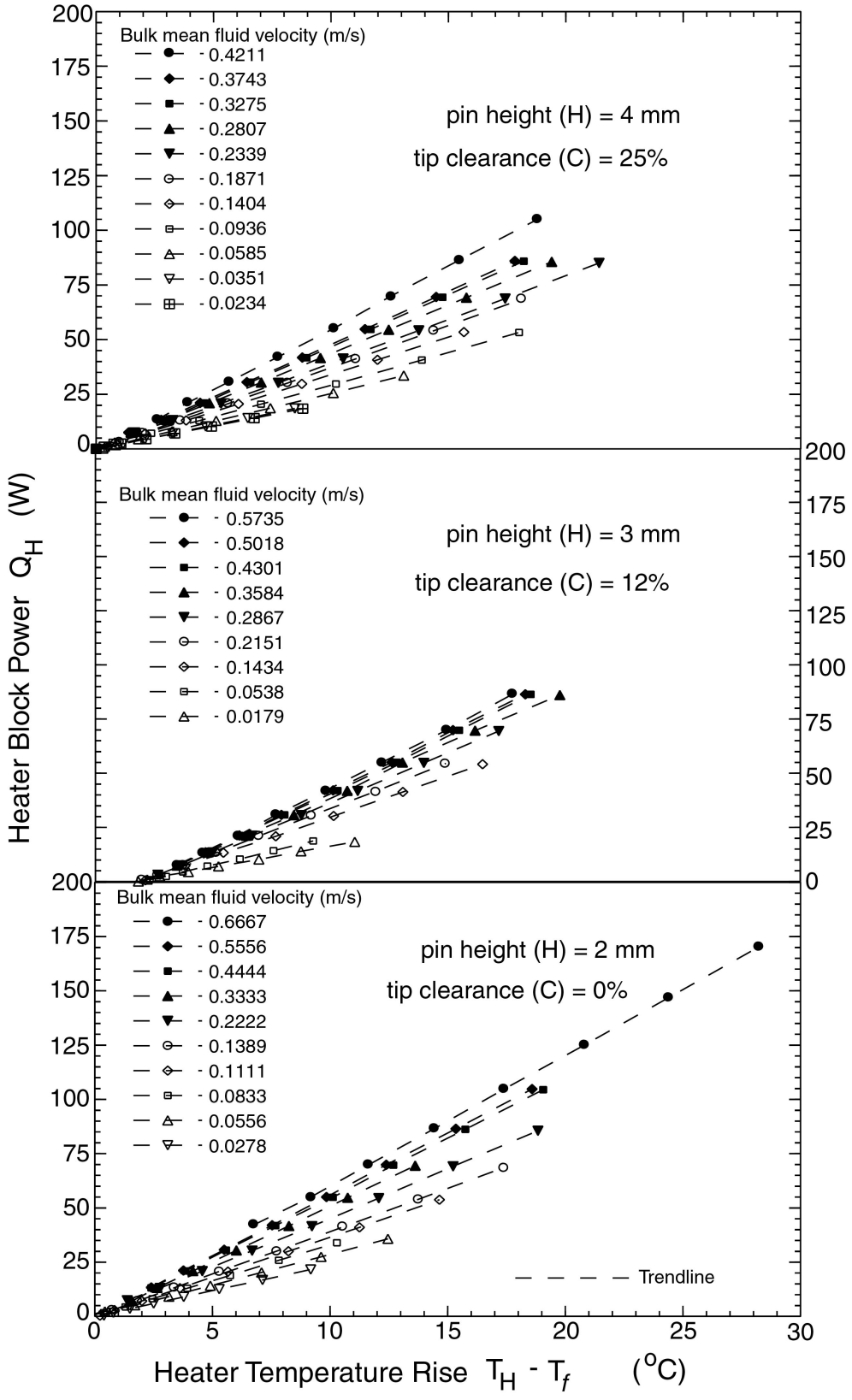

Figure 3.13: Results of forced convection loss calibration tests

The data shows the rate of heat loss to be similar in all three cases. It is also noted that as the bulk mean fluid velocity increases, it causes the characteristic loss curves to essentially rotate through an angle (θ) with respect to the abscissa of the graph as illustrated in **Figure 3.14.**

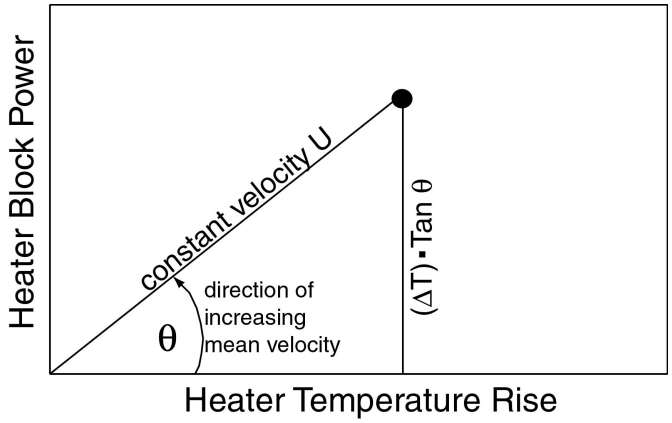

Figure 3.14: Characteristic behavior of convective heat transfer losses

That angle (θ) has been plotted as a function of mean fluid velocity (U) in **Figure 3.15** for each of the calibration curves of **Figure 3.13**. Based on the fact that θ does not vary considerably among the three test cases for any given fluid velocity, a fifth order least square polynomial was fit to the data and is used to calculate the forced convection losses for all test cases presented in this study. The resulting model of convective heat losses is of the form:

$$Q_{L,conv} = \left(T_H - T_f\right)\tan\theta - Q_{L,cond} \tag{3.6}$$

where θ is measured in radians and is calculated from:

$$\theta = 1.06 + 3.71U - 21.33U^2 + 63.13U^3 - 88.85U^4 + 47.05U^5 \tag{3.7}$$

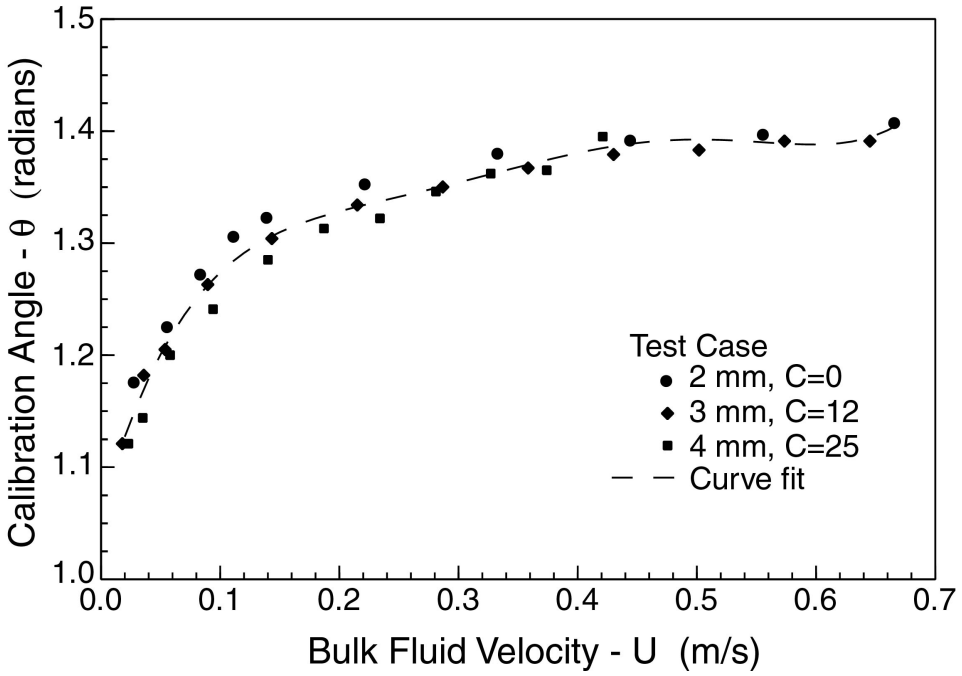

Figure 3.15: Calibration angle (θ) vs. channel flow rate

The term $Q_{L,cond}$ in **equation (3.6)** accounts for conduction losses present during the calibration of forced convection losses and is calculated from **equation (3.5)** using the corresponding heater and ambient temperatures for each given calibration point. The use of this single calibration curve to model forced convection heat losses for all pin lengths and tip clearances introduces a maximum uncertainty in predicted convective heat loss of 8.3 percent. This corresponds to a maximum of 1.2 percent error in modeling the total array heat load (Q_A).

The heat dissipated by the pin fin array itself is then calculated as:

$$Q_A = Q_H - Q_{L,cond} - Q_{L,conv} \tag{3.8}$$

where: Q_H is the total electrical heat generated in the copper block

$Q_{L,cond}$ represents conduction, natural convection and radiation based losses

$Q_{L,conv}$ represents losses from forced convection outside the array

Q_A is the actual heat dissipated by the pin fin array itself

Similarly, the pressure drop ascribed to the array itself was determined from the difference between the pressure drop measured with a given base plate in place and that produced when a flat calibration plate is installed:

$$\Delta P_A = \Delta P_{bp} - \Delta P_{fp} \tag{3.9}$$

3.3 System Energy Balance and Estimation of T_f

Mean heat transfer rates are based upon the difference between the average local base plate endwall temperature and the local average fluid temperature (a formal definition will be defined in **Section 3.4**). The average local base plate temperature is determined for each of (49) unit cells by way of the liquid crystals. For the estimation of the local bulk fluid temperature, the initial intent was to use data from the two thermocouples suspended in the inlet flow stream, and the three thermocouples suspended in the outlet flow stream.

To judge the propriety of this approach, an energy balance was performed on the fluid stream to compare the temperature rise of the water as measured by the thermocouples, to that which is expected based on the total energy imparted to the fluid by the heater. The expected temperature rise is determined through calorimetry according to the equation:

$$\Delta T_{cal} = \frac{Q_{cal}}{\dot{m}cp} \tag{3.10}$$

where:

$$Q_{cal} = Q_H - Q_{L,cond} \tag{3.11}$$

The relative difference between the two temperature rises is then defined as:

$$\varepsilon = \frac{\Delta T_{cal} - \Delta T_{meas}}{\Delta T_{cal}} \tag{3.12}$$

where:
$$\Delta T_{meas} = T_{f,out} - T_{f,in} \tag{3.13}$$

Figure 3.16 depicts the results of the energy balance for all trials. In all but two cases, the measured fluid temperature rise is within 20 percent of the expected value, with the discrepancy being largest at low Reynolds number and tending towards zero with increasing Re. The higher discrepancy at low Re suggests that the flow remained thermally stratified in this regime despite the use of turbulator screens upstream and downstream of the array. The three thermocouple measurements taken at the downstream location were therefore not sufficient to characterize the true mean value of the exiting fluid temperature, with the temperature being underestimated in the majority of cases. The level of discrepancy decreases at the upper range of Re. This can be attributed to increasing levels of turbulence at higher Re and the resulting mixing that occurs. In the majority of cases for Re > $2x10^2$, the energy balance is within 5 percent.

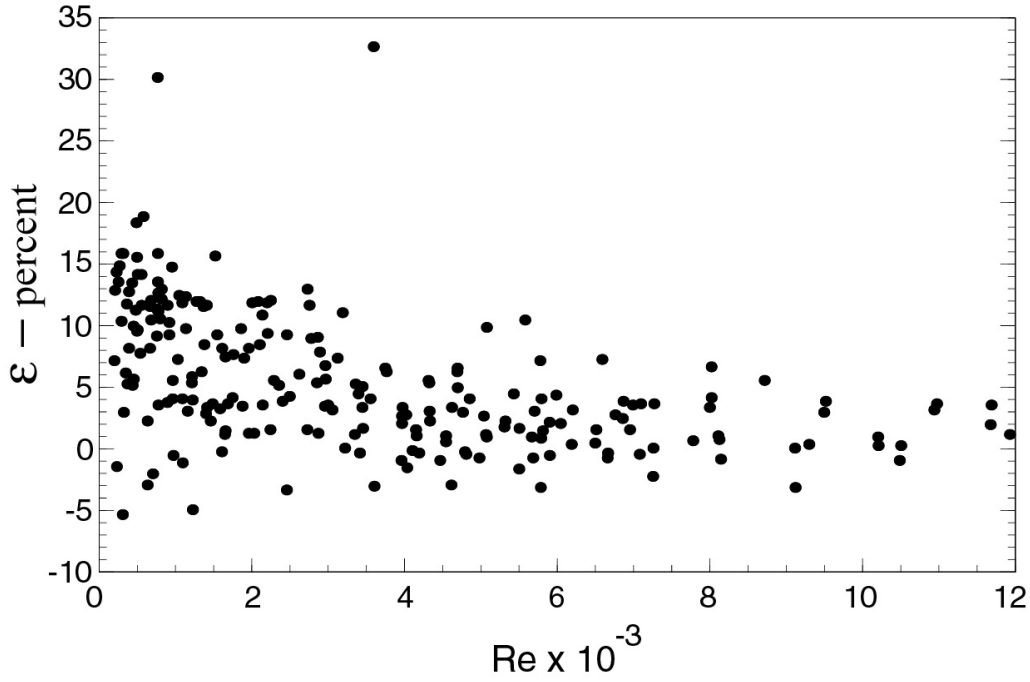

Figure 3.16: Energy balance between measured and expected fluid temperature rise

To remedy this deficiency in the fluid temperature measurements, the value of mean bulk fluid temperature used to calculate heat transfer rates (h and Nu) is based on calorimetry estimates exclusively. Predicted mean bulk fluid temperature at a given row within the array is calculated as:

$$T_f = T_{in} + \frac{\frac{Q_{L,conv} + Q_A}{2} \pm \frac{10.5}{158} Q_A Nr}{\dot{m} cp_f} \tag{3.14}$$

where Nr is the number of rows from the centerline of the array with the second term in the numerator being additive for rows downstream of the centerline and subtractive for rows upstream of the centerline. T_{in} is the average inlet fluid temperature as measured by the inlet thermocouples and the specific heat (cp_f) of the fluid is estimated as:

$$cp_f = 4.22 - 2.96 \cdot 10^{-3} T_{in} + 7.73 \cdot 10^{-5} T_{in}^2 - 8.01 \cdot 10^{-7} T_{in}^3 + 3.28 \cdot 10^{-9} T_{in}^4 \qquad (3.15)$$

Mass flow rate is calculated based on a fluid density estimated by:

$$\rho_f = 999.92 + 1.07 \cdot 10^{-1} T_{in} - 1.09 \cdot 10^{-2} T_{in}^2 + 9.61 \cdot 10^{-5} T_{in}^3 - 4.03 \cdot 10^{-7} T_{in}^4 \qquad (3.16)$$

The above property models are based on data for water from **Incropera & Dewitt (1985)**.

Because the fluid is mechanically mixed within the chiller prior to entering the test section, the inlet temperature measurements at the test section are expected to be much more representative of the bulk fluid temperature than was achieved by the outlet measurements. Therefore reliance on the inlet thermocouple measurements is considered justified.

3.4 Data Reduction

In the analysis of pin fin array performance, a multitude of definitions is possible in terms of how one non-dimensionalizes the results. This is evidenced by a summary of previous definitions used in the literature as provided in **Appendix A**. Wherever possible, those definitions most widely used in the field have been adopted here to aid in direct comparisons.

3.4.1 Hydrodynamic Pressure Performance

Dimensionless pressure drop results are reported in terms of the friction factor:

$$f = \frac{\Delta P_A}{2\rho_f V_{\max}^2 N} \tag{3.17}$$

where N is the number of rows in the array. Two forms of the friction factor are commonly used in the pin fin literature, with the alternate version being a factor of four greater than (**3.17**). The above form was adopted in this study primarily to correspond with the results presented by **Armstrong and Winstanley (1988)** who attempted to summarize the work of others done to date on the performance of short pin fin arrays.

Of practical concern in using forced liquid cooling is the relative amount of pumping power required for a given scenario. In general, pumping power can be defined as:

$$Power = \left(\Delta P_A\right)\left(\dot{V}\right) \tag{3.18}$$

3.4.2 Thermal performance

Heat transfer results are presented primarily in dimensionless form as the Nusselt number (Nu). Mean heat transfer from the pin fin array is determined as:

$$Nu = \frac{hD}{k_f} \tag{3.19}$$

where the characteristic length scale of the array is taken to be the pin diameter (D), as is standard in the pin fin literature, and the heat transfer coefficient (h) is defined as:

$$h = \frac{Q_A}{A(T_{ew} - T_f)} \tag{3.20}$$

The area (A) is either the total wetted surface area of the pin array (A_w), which includes all surface area within the borders of the array that is in contact with the cooling fluid and which changes when clearance is introduced above the array, or the projected area of the array (A_p), which is defined as the product of the transverse width of the array and the streamwise length of the array, and which does not change with clearance. Results based on A_p reflect the practical impact of clearance on array heat transfer performance, as would be of interest to a system designer whose primary concern is to maximize heat transfer for a given array footprint. Results based on A_w on the other hand, help to provide insight into the effect that clearance has on local heat transfer behavior.

The fluid thermal conductivity (k_f) is assumed constant along the length of the array and is based on the inlet temperature according to the model:

$$k_f = 0.57 + 1.77 \cdot 10^{-3} T_{in} - 5.39 \cdot 10^{-6} T_{in}^2 + 8.92 \cdot 10^{-9} T_{in}^3 - 4.27 \cdot 10^{-11} T_{in}^4 \tag{3.21}$$

which is a least-squares polynomial curve fit to thermo-physical data for water at atmospheric pressure as defined by **Incropera & Dewitt (1985)** and is in units of W/mK.

Both heat transfer and pressure drop results are presented as a function of Reynolds number (Re). Many forms of Re have been used in past studies of shrouded pin fin arrays. In the current study, the form of Re is based on that originally recommended by **Zukauskus (1972)** for the analysis of flow across tube banks:

$$\mathrm{Re} = \frac{\rho_f V_{\max} D}{\mu_f} = \frac{V_{\max} D}{\nu_f} \tag{3.22}$$

where $V_{\max}$ is the maximum estimated bulk velocity within the array based on the minimum cross-sectional flow area along the channel, and is the greater of:

$$\mathrm{V}_{\max} = U \frac{\mathrm{S_T}(H + Cg)}{(\mathrm{S_T}(H + Cg) - \mathrm{HD})} \quad \underline{\text{or}} \quad \mathrm{V}_{\max} = U \frac{\mathrm{S_T}(H + Cg)}{2(\mathrm{S_D}(H + Cg) - \mathrm{HD})} \tag{3.23}$$

This dual nature arises from the fact that, depending on the relative magnitudes of the streamwise and transverse pin spacing, the minimum cross-sectional area can occur at either of two points in the array. **Equation 3.23** differs from the definition used by **Zukauskus** in that it introduces the concept of having a clearance gap (Cg) above the array. **Figure 3.16** provides a cross-sectional view of an array unit cell to illustrate how the minimum flow area changes when a clearance gap is present. For the case of zero tip clearance, **equation 3.23** simplifies to the classical definition of maximum velocity as defined by **Zukauskus**.

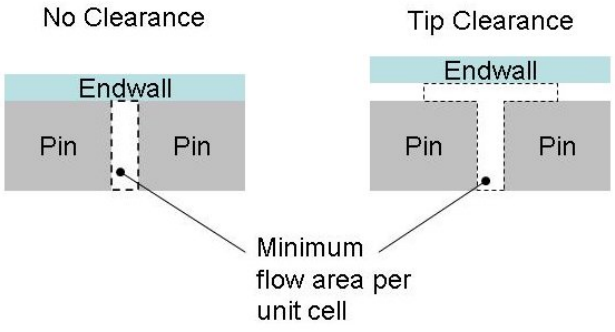

Figure 3.17: Unit cell based minimum flow areas

3.4.3 Fin Efficiency

Some of the heat transfer results reported in **Chapter 4** have been modified to account for differences in fin efficiency to better compare the performance between the various fin heights. This also facilitates more meaningful comparisons between the results of the current study and those of past or future studies, particularly in cases where naphthalene sublimation is employed; a common technique in pin array studies that by its nature produces results corresponding to 100 percent fin efficiency. Where indicated, the reported data has been prorated to 100 percent fin efficiency according to the relationship:

$$h_{100} = \frac{h}{\eta} \tag{3.24}$$

Assuming the temperature profile along the length of the pin fins to be approximately linear, and using the average endwall and pin tip temperatures as determined from the TLC analysis, the efficiency η is calculated as:

$$\eta = \frac{\theta_{pt} + \frac{1}{2}\left(T_{ew} - T_{pt}\right)}{\theta_{ew}} \tag{3.25}$$

where:

$$\theta_{ew} = T_{ew} - T_f \tag{3.26}$$

$$\theta_{pt} = T_{pt} - T_f \tag{3.27}$$

3.4.4 General Correlations

The primary aim of this study is to experimentally ascertain the basic impact and behavior associated with the introduction of tip clearance to an array of short pin fins in cross-flow. Also of interest is the potential establishment of general correlations that can be used to predict array performance as a function of tip clearance. To this end, empirically based models are developed for both pressure drop and heat transfer.

In the case of pressure drop, a correlation is expressed in the form of the dimensionless pressure drop or friction factor (f), For the given staggered array geometry as illustrated in **Figure 3.17**, it can be shown that:

$$f = \mathrm{f}\left[\left(\frac{\rho_f \mathrm{V}_{\max} D}{\mu_f}\right),\left(\frac{H}{D}\right),\left(\frac{Cg}{D}\right),\left(\frac{S_L}{D}\right),\left(\frac{S_T}{D}\right)\right] \tag{3.28}$$

where pin diameter (D) has been chosen as the characteristic length upon which to normalize the geometry variables.

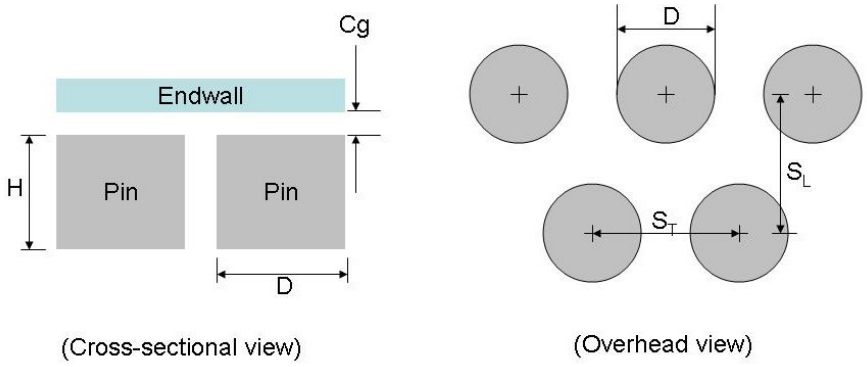

Figure 3.18: Staggered array geometry variables

In the current study, the fourth and fifth terms on the right hand side of the above relationship vary by a maximum of four percent across all cases considered. By comparison, the first three terms are varied by 6000 percent, 220 percent, and 27 percent respectively. As such, the last two terms, which represent pin pitch effects are considered to be constant in this study and thus are not covered by the proposed correlations. Based on previous works (**Metzger 1982, Olsen 1992, Short 1994**), the presumed form of a general correlation is that of a power law relationship, which in this case will be of the form:

$$f = \alpha_0 \left(\frac{\mathrm{H}}{\mathrm{D}}\right)^{\alpha_1} \left(1 + \frac{\mathrm{Cg}}{\mathrm{D}}\right)^{\alpha_2} \mathrm{Re}^{\alpha_3} \tag{3.29}$$

In the case of heat transfer, for the dimensionless form as represented by the Nusselt number (Nu), it can be shown that:

$$Nu = \mathrm{f}\left[\left(\frac{\rho_f \mathrm{V}_{\max} D}{\mu_f}\right), \left(\frac{H}{D}\right), \left(\frac{Cg}{D}\right), \left(\frac{S_L}{D}\right), \left(\frac{S_T}{D}\right), \left(\frac{cp_f \mu_f}{k_f}\right), \left(\frac{\theta_{pt}}{\theta_{ew}}\right)\right] \tag{3.30}$$

Based on the fact that fluid properties are referenced at inlet conditions, the sixth term, which by definition, is the Prandtl number (Pr) for the flow, varies by no more than ± 3 percent. As such, this term is also considered to be essentially invariant for the purpose of correlating the results. The last term above represents the effect of temperature reduction along the length of the pin due to conduction losses. Because both the endwall and pin tip temperatures are known this parameter can be effectively eliminated as a variable by adjusting the observed heat transfer coefficients as a

product of the apparent fin efficiency so that the results correspond to $\theta_{pt}/\theta_{ew} = 1$ for all cases.

Again assuming a power law relationship based on previous pin fin array works (Metzger 1982, Chyu 1990, Jubran 1993, Short 1994, Chyu 1998, Hwang 1999), a general correlation for heat transfer is taken to be of the form:

$$Nu = \alpha_0 \left(\frac{\mathrm{H}}{\mathrm{D}}\right)^{\alpha_1} \left(1 + \frac{\mathrm{Cg}}{\mathrm{D}}\right)^{\alpha_2} \mathrm{Re}^{\alpha_3} \tag{3.31}$$

3.5 Estimated Uncertainties

A summary of uncertainties is provided here to a confidence level of 95 percent. Thermocouple based uncertainty measurements were determined through direct calibration using an ice bath and a precision thermometer with a 1/20 °C gradation. Repeated measurements on all (20) available data channels of the Hewlett Packard data acquisition system produced an estimated uncertainty of ± 0.125 °C. Liquid crystal based temperature uncertainties associated with each unit cell are taken to be a Root Mean Square (RMS) combination of the thermocouple uncertainties and the Standard Estimate of Error (SEE) associated with each polynomial curve fit to the liquid crystal calibration data. For the 1230 individual calibration curves employed in this study, the estimated maximum uncertainty was ± 0.39 °C, with the mean being ± 0.23 °C.

All other reported uncertainties have been determined using the approach of **Kline and McClintock (1953),** assuming uncertainties associated with array and channel dimensions to be negligible. The overall uncertainties in differential pressure,

mass flow rate, power, and the derived dimensionless values of Re, Nu, and f were estimated and are summarized in **Table 3.1**. The highest uncertainties in heat transfer occur at the low end of the Re range (Re < 1000). Through the majority of the flow range, uncertainties in Nu are typically on the order of 6 to 8 percent. Details of the uncertainty calculations are provided in **Appendix B**.

Table 3.1: Summary of estimated experimental uncertainties

Variable	Maximum Uncertainty (95 percent confidence level)
T (thermocouples):	± 0.13 °C
T (liquid crystals):	± 0.39 °C
ΔP:	± 1.1 %
$\dot{m}$:	± 2.4 %
Q_H :	± 0.4 %
Re:	± 3.6 %
Nu :	± 13.0 %
f :	± 4.5 %

Chapter 4: Experimental Results and Discussion

Results from the experimental and analytical work discussed in Chapters 2 and 3 are presented here. The first section of this chapter focuses on the hydrodynamic pressure loss experiments. This is followed then by a look at the quantitative effects that tip clearance has on the mean heat transfer of the array. Where available, comparisons to existing data are made and relative performance metrics for heat transfer and pumping power are presented. Finally, local quantitative as well as qualitative behavior of the array heat transfer is illustrated by way of the full field liquid crystal images and measurements.

4.1 Adiabatic Pressure Drop

As stated in **Section 2.4.3**, the pressure drop measurements were conducted separately from the heat transfer trials, with zero heat flux applied to the assembly. In this section the effects of tip clearance on array pressure drop are considered and a correlation for its estimation is proposed. This is followed by a comparison of the current non-clearance data with that of existing data from the literature.

4.1.1 Effects of Tip Clearance

Net pressure losses vs. flow rate across the pin array are shown in **Figure 4.1**. For a given flow rate, the data shows a decrease in overall pressure drop with each successive increase in tip clearance as expected. An exception to this trend occurs at

(C = 25%, H/D = 0.5 mm), which produced essentially the same pressure drop as the 18 percent clearance case.

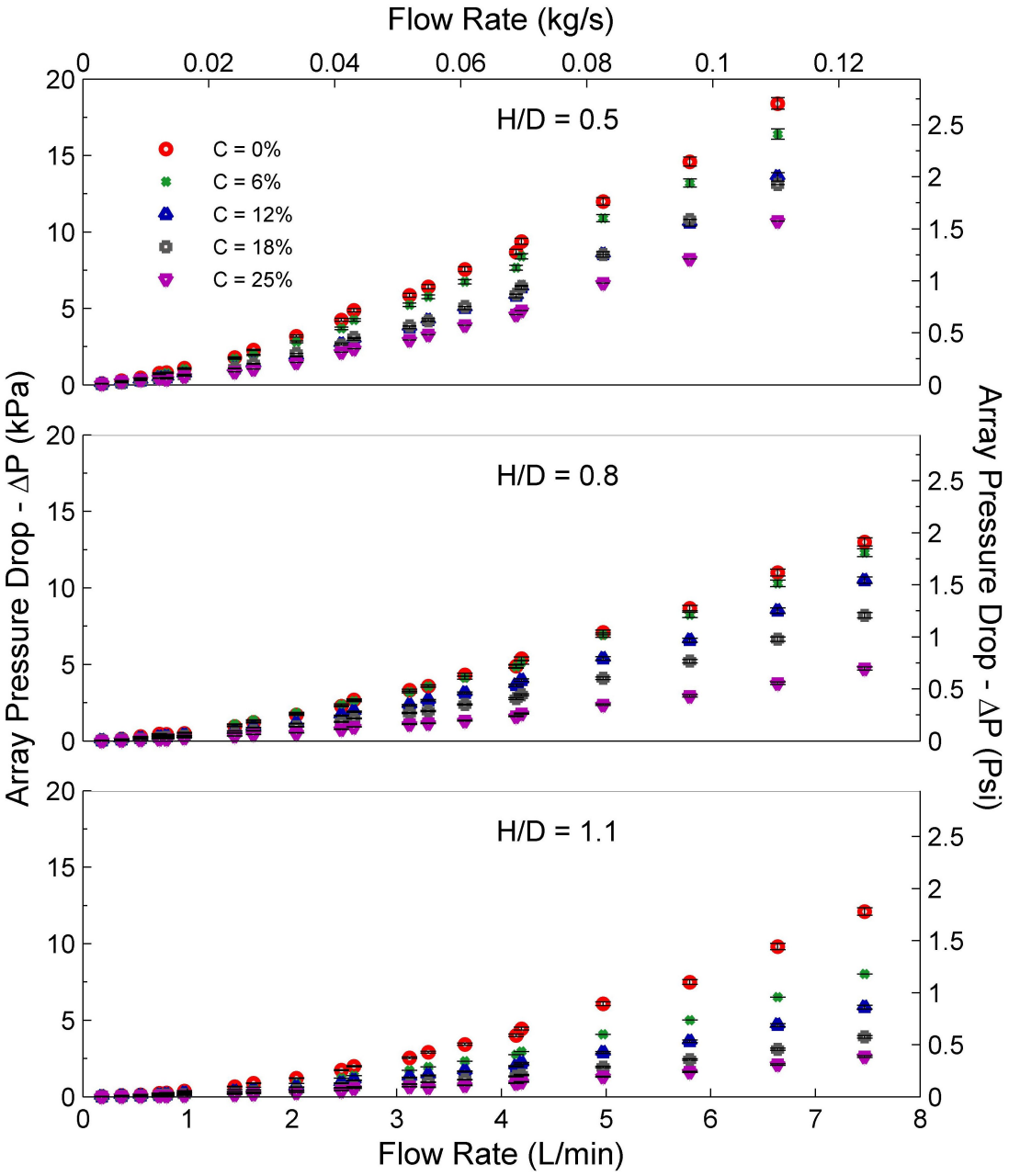

Figure 4.1: Array pressure drop vs. flow rate

Pressure drop is presented in **Figure 4.2** as a function of Reynolds number, which allows comparison between the various clearance levels by accounting for changes in flow area.

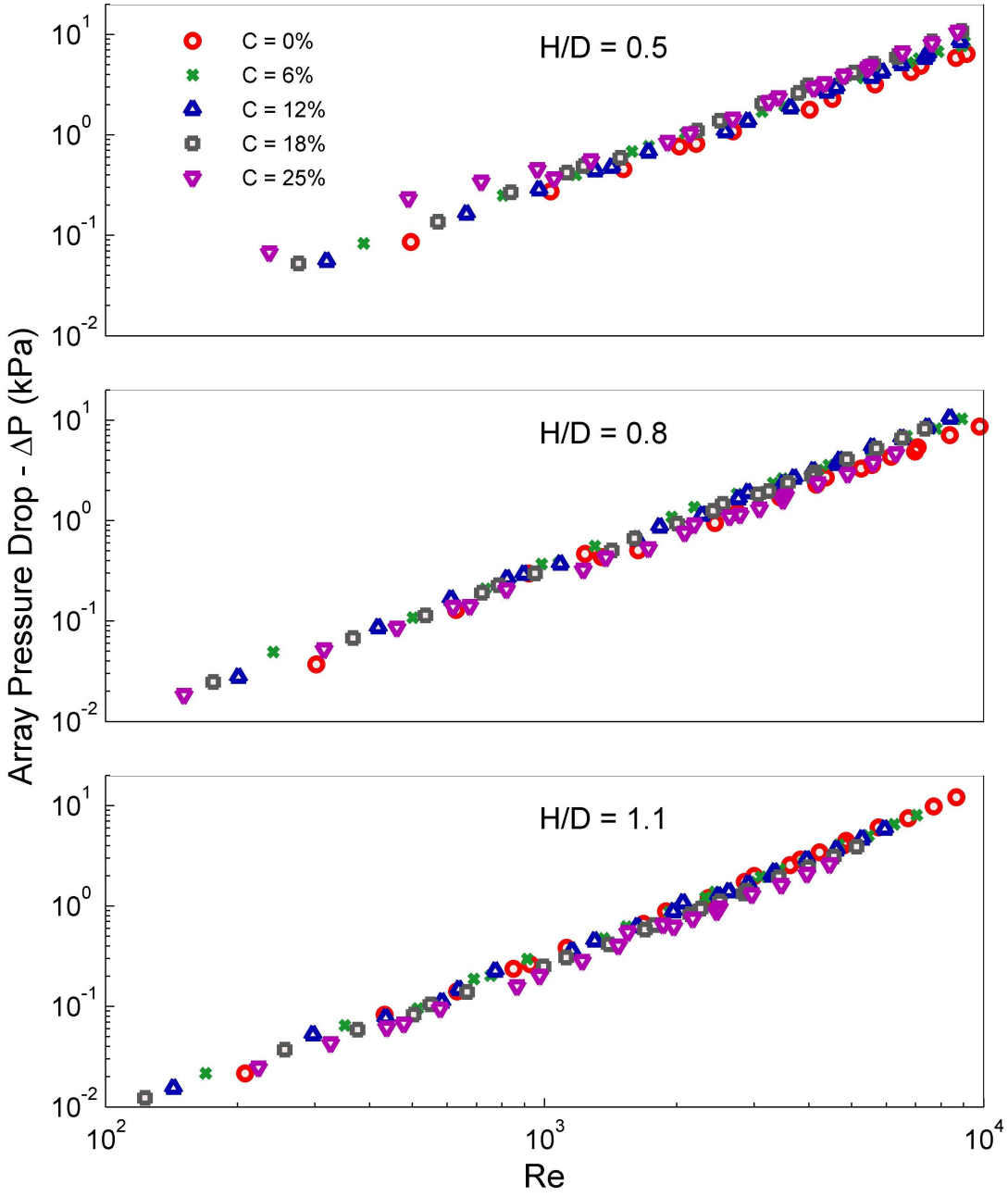

Figure 4.2: Array pressure drop vs. Re (based on V_{max})

As a general rule, the data for each combination of H/D and C closely follows a power law relationship to Reynolds number. Considering the dimensionless form of pressure drop as defined in **equation 3.17**, the data is fit according to the power law relationship:

$$f = \alpha_0 \, \mathrm{Re}^{\alpha_1} \tag{4.1}$$

where the specific values of α_0 and α_1 are listed in Table 4.1.

Table 4.1: Power law coefficients

H/D	C (%)	α_0	α_1
0.5	0	5.67	-0.52
0.5	6	9.02	-0.54
0.5	12	6.72	-0.52
0.5	18	6.29	-0.48
0.5	25	36.5	-0.70
0.8	0	3.30	-0.44
0.8	6	7.77	-0.51
0.8	12	4.17	-0.44
0.8	18	5.42	-0.48
0.8	25	8.42	-0.57
1.1	0	1.72	-0.33
1.1	6	4.07	-0.44
1.1	12	3.96	-0.45
1.1	18	5.46	-0.52
1.1	25	2.32	-0.41

Employing these relationships, the general pressure drop behavior for each case of H/D can be depicted simultaneously as a function of Re and Cg/D as shown in **Figure 4.3**. In both cases of H/D below unity, a maxima is evident and occurs at Cg/D of approximately ten percent, with the relative increase to the non-clearance case being greatest for H/D = 0.5. For aspect ratio greater than 1.0, the maximum

occurs at the non-clearance case. This behavior suggests that, at least for very short pin fins, a pressure drop penalty exists when small clearance gaps are present.

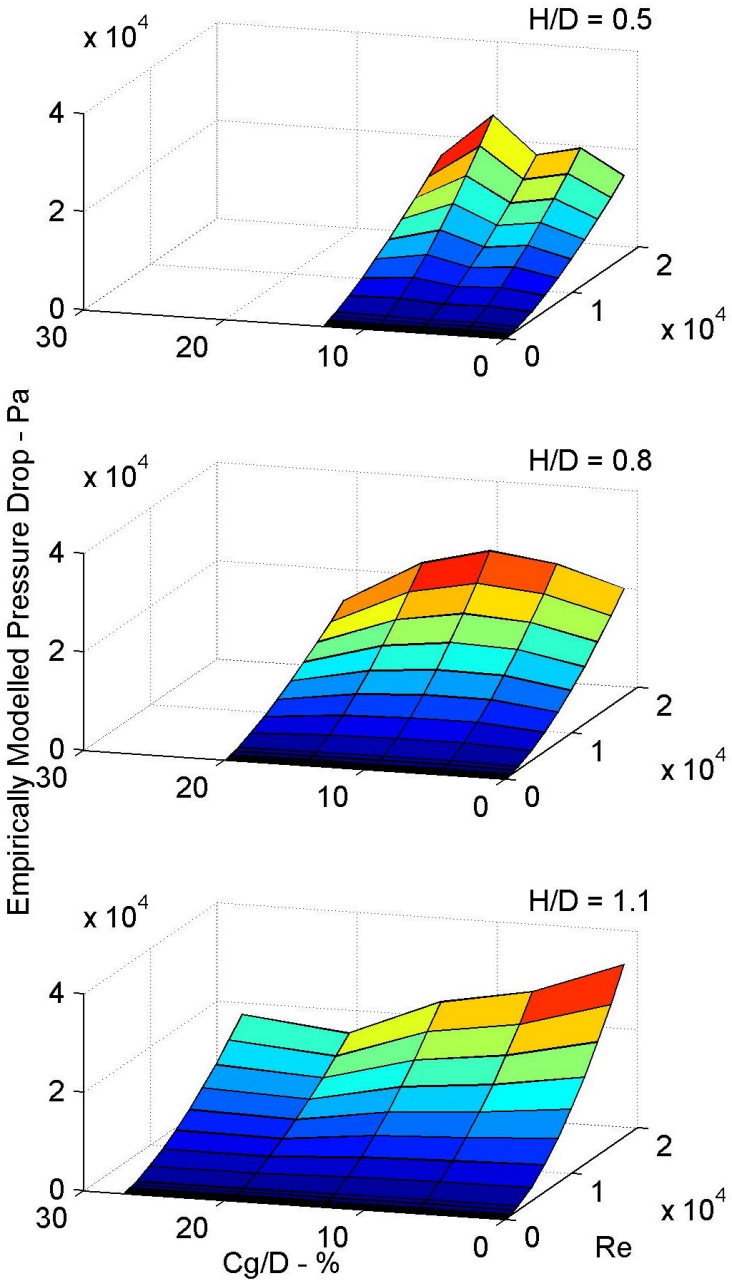

Figure 4.3: Pressure Drop behavior as a function of clearance gap and Reynolds number

Aside from pressure losses, a metric that is of particular interest to designers and engineers is the amount of power required to pump the fluid through the array. Pumping power, defined by **equation 3.18**, is shown in **Figure 4.4** for each case H/D.

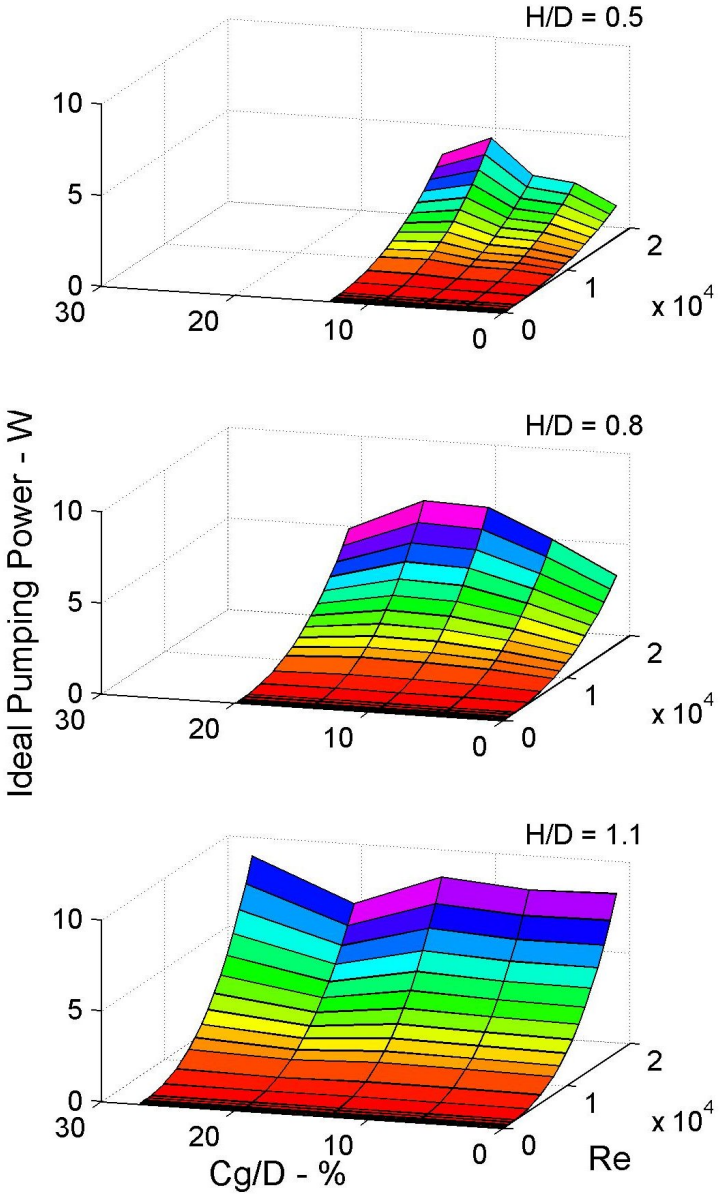

Figure 4.4: Ideal Pumping power as a function of clearance gap and Reynolds number

Pumping power is of course a strong function of Reynolds number. Similar to the pressure drop results, a distinct maximum occurs when a clearance gap is present for both H/D = 0.5 and 0.8, with the relative maximum being larger at higher values of Re. However, it is interesting to note that for H/D 1.1, the pumping power is relatively invariant with clearance as the rate of change in volumetric flow rate associated with an increase in clearance appears to be offset by an equivalent reduction in pressure drop.

4.1.2 General Correlation of Pressure Drop

In an effort to generalize the experimental results, an empirical correlation which considers all relevant variables is sought. As discussed in **section 3.3.4**, the anticipated form of this correlation is:

$$f = \alpha_0 \left(\frac{H}{D}\right)^{\alpha_1} \left(1 + \frac{Cg}{D}\right)^{\alpha_2} Re^{\alpha_3} \qquad (4.2)$$

To fit all data to a single model, a non-linear multiple regression analysis was performed using NLREG [**Sherrod, 2001**] in which the parameters α_0, α_1, α_2, and α_3 are determined by a least squares fit for the full range of pressure data for $2 \cdot 10^2 < Re < 1.8 \cdot 10^4$.

Figure 4.5 provides a comparison between the experimental data and the resulting correlations. The data is plotted with Reynolds number along the independent x-axis and the non-Reynolds dependent terms of the correlation along the y-axis. In this format, the correlation is represented by the line $2.63Re^{0.39}$.

For the case of no tip clearance, the correlation does a fairly good job, with the data for all values of H/D closely grouped along the correlating line throughout the Re range. For this case, the correlation predicts the pressure loss to within ± 21.3 percent with a confidence level of 95 percent. However, given the spread of data where clearance is present, it is clear that the assumed power law relationship is not sufficient to capture the impact of tip clearance. Overall, the correlation predicts all cases to within ± 42.3 percent.

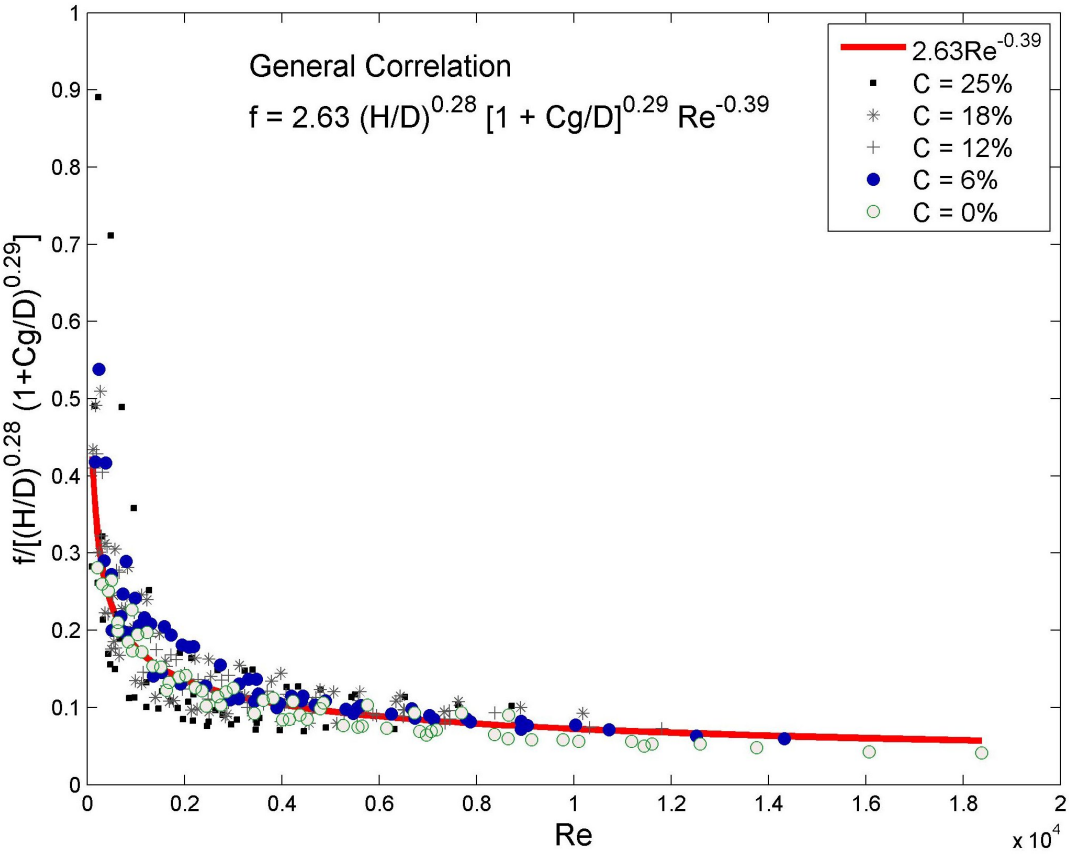

Figure 4.5: General Power Law Correlation of non-dimensional pressure loss data

The data of **Figure 4.5** shows for a given Re that the friction factor initially increases relative to the non-clearance case, with data for C of 6 and 12 percent generally above the curve, and data for C of 18 and 25 percent below the curve. The initial increase may be the result of the flow having to navigate through and around the relatively tiny gaps between the shroud and the array. For the amount of added flow area that these gaps provide, they likely contribute relatively higher surface friction losses to the flow than the array does as a whole. But as the gap continues to increase, it begins to contribute flow area that is not dominated by surface effects, thus causing the overall friction factor of the array to decline at a given Re.

Given the poor performance of **Equation 4.2** to predict the impact of clearance, separate correlations for each set of C were considered next. They are of the simplified form:

$$f = \alpha_0 \left(\frac{H}{D} \right)^{\alpha_1} \mathrm{Re}^{\alpha_2} \tag{4.3}$$

Separate non-linear multiple regression analyses produced the parameters shown in **Table 4.2.** With the exception of C = 6, the correlation parameters exhibit a relatively consistent and monotonic relationship with increasing values of C. More specifically, close examination of these trends indicated that each parameter behavior could be modeled closely as an exponential function of Cg/H.

Table 4.2: Regression parameters for C-independent correlations

C	α_0	α_1	α_2
0	2.63	0.28	-0.39
6	5.87	-0.18	-0.49
12	4.39	-0.08	-0.46
18	5.06	-0.46	-0.49
25	7.92	-1.50	-0.61

Based on this, the general correlation as given in **Equation 4.4** is proposed.

$$f = 2.63\kappa_1 \cdot \left(\frac{H}{D}\right)^{0.28+(1-\kappa_1)} \mathrm{Re}^{-0.39+(1-\kappa_2)} \tag{4.4}$$

Where:

$$\kappa_1 = e^{4.3(Cg/H)} \tag{4.4a}$$

$$\kappa_2 = e^{0.8(Cg/H)} \tag{4.4b}$$

$$Cg/H \leq 0.26$$

This model, illustrated in **Figure 4.6**, successfully predicts the experimental data to within ± 21.3 percent at a confidence level of 95 percent for $C \leq 19$ percent, which is roughly a 2-fold improvement over the general correlation of **equation 4.2**. For larger clearances below 26 percent, **equation 4.4** predicted the data to within ± 31.7 percent, or a fifty percent improvement over **equation 4.2**. It is extremely important to note

that **equation 4.4** is not a physically based model and should not be extended beyond the limits considered in this study without prior verification.

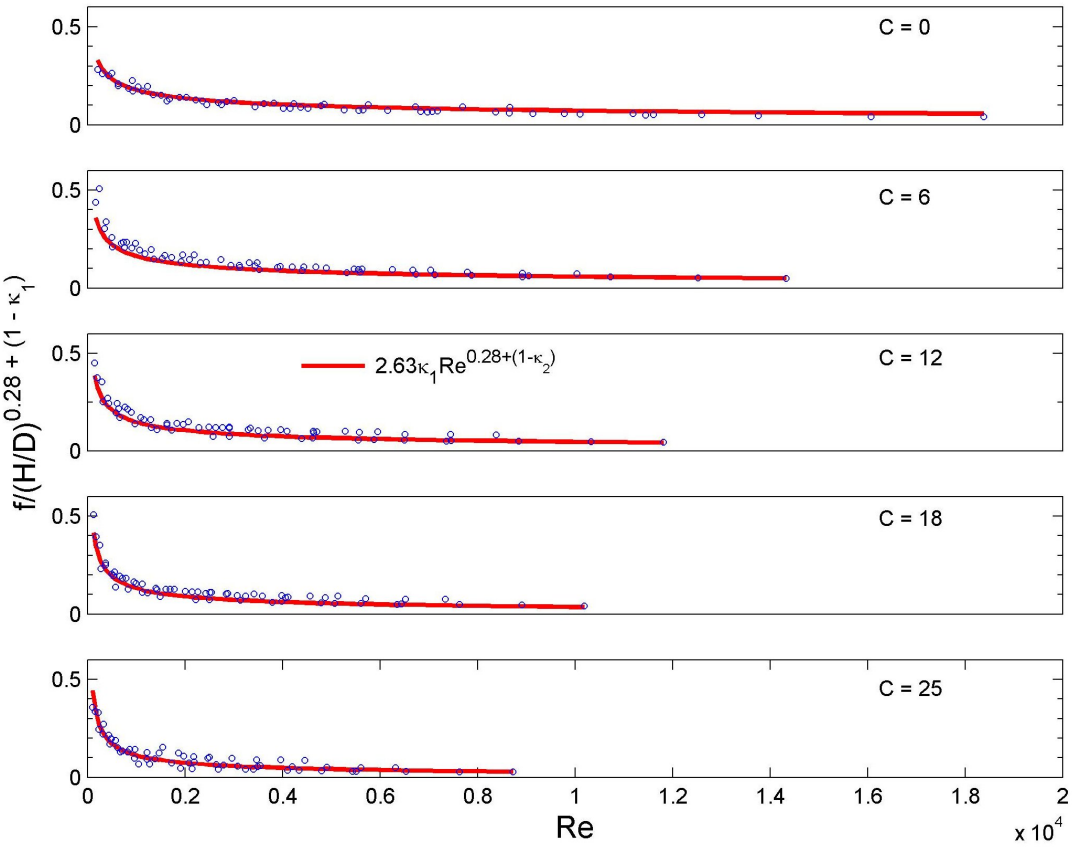

Figure 4.6: Modified general correlation of friction factor (*f*) vs. Re, Cg/H, H/D

4.1.3 Comparisons with Literature

There is unfortunately no experimental pressure drop data available in the literature that encompasses the effects of tip clearance within the ranges considered here. However, a very recent numerical study conducted by **Rozati et al. (2008)** did investigate the role of tip clearance in pin fin arrays. Using periodic boundary conditions and a unit-cell domain, they modeled the geometry of a staggered pin fin array with H/D ranging from 0.6 to 1.0, Cg/D from 0 to 0.4, S_T/D of 2.12 and S_L/D of

1.06. With the exception of the somewhat larger transverse pin pitch, the geometry of **Rozati** compares quite closely to that of the current study, though due to the difficulty of accurately modeling highly turbulent flows, the authors limited their analysis to Re of 5 - 400, which is at the low end or below that considered here.

Figure 4.7 is a reprint of Rozati's data in which he depicts the effect of clearance (t = Cg/D) on the friction factor of a pin fin array, relative to that of an open channel. The model predicts an initial increase in friction factor at low levels of tip clearance relative to the non-clearance case, with (*f*) dropping below that of Cg = 0 as clearance is increased further. This is precisely the behavior observed in the current study (**Figure 4.5**).

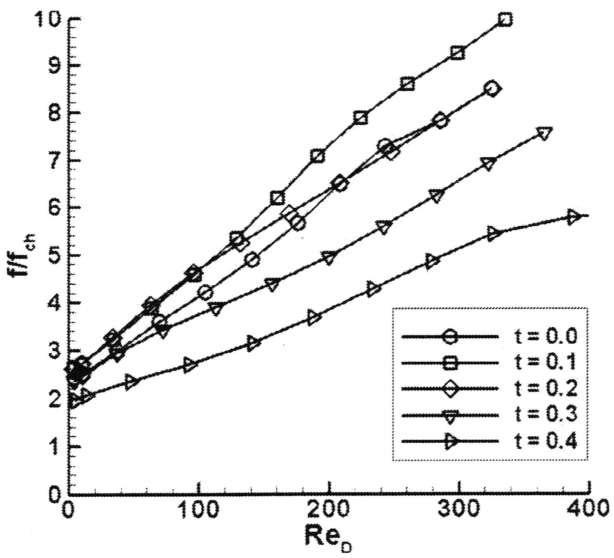

Figure 4.7: Numerically modeled friction factor as a function of tip clearance and Reynolds number (**Rozati et al., 2008**)

Rozati attributed this behavior to a balance between wall shear stresses and form drag. As small amounts of clearance are first introduced, a relatively large increase in wall shear stresses is introduced, with only modest reductions in form

drag, resulting in a greater overall friction factor. At higher levels of clearance, form drag is substantially reduced, resulting in an overall drop in friction factor.

Beyond this one numerical study, there appears to be no data based on tip clearance with which to compare. There is a limited amount of existing data for the non-clearance case however. To make this comparison, the current experimental data for C = 0 is considered, and is fit to a reduced friction factor power law correlation that is a function of Re only ($f = \alpha_0 \mathrm{Re}^{\alpha_1}$) so as to be of the same format as employed in most of the earlier works. The results of this least squares fit is depicted in **Figure 4.8** which shows f to increase with increasing ratios of H/D, with the difference being the greatest at the higher Reynolds numbers.

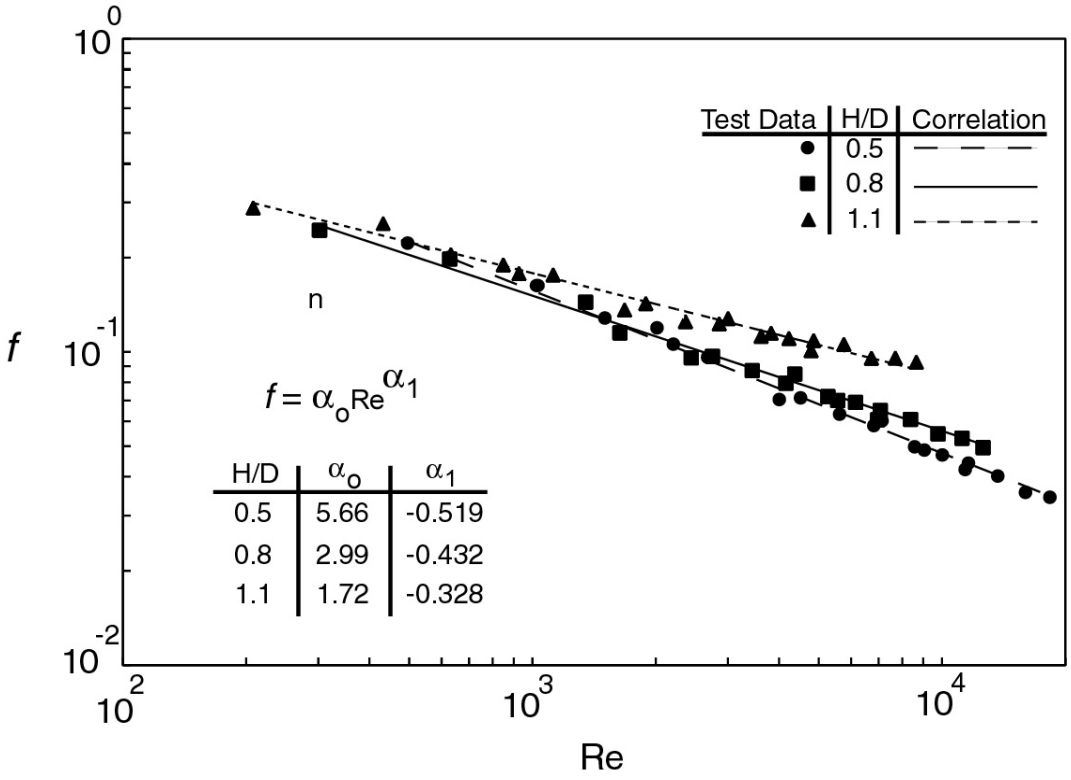

Figure 4.8: Standard power law correlation of friction factor for non-clearance cases only

A comparison of the current non-clearance results with available data from the literature is provided in **Figure 4.9**. While similar, none of the arrays considered in previous studies are identical in geometry to those in the current study. For the purposes of this comparison, the current results for H/D = 0.5 and 1.1 are displayed. The majority of available data from the literature corresponds to H/D of approximately 1.0. Transverse and longitudinal pin pitch differs somewhat between the various cases however. Where necessary, the original form of the literature data has been modified to account for differences in the definition of friction factor employed by the various authors.

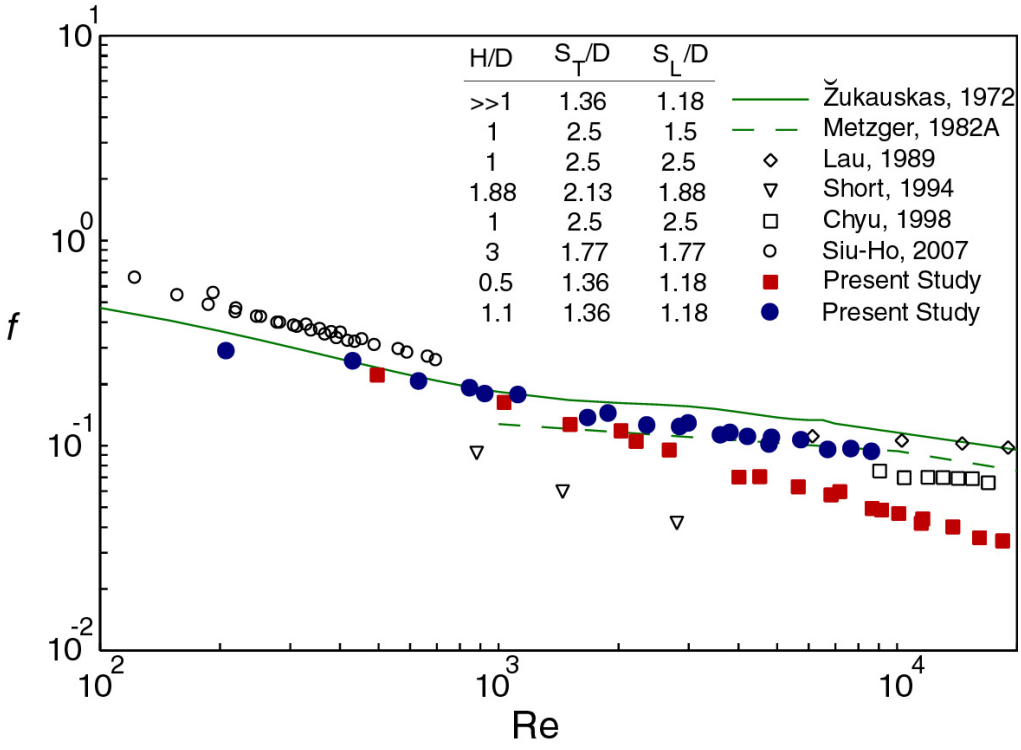

Figure 4.9: Comparison of pressure loss results to existing literature data

The Zukauskas correlation for pressure drop, which is the only known general purpose correlation available in the open literature, was developed from tube bank performance data with H/D typically on the order of 100. Given this and the trends depicted in **Figure 4.8**, one would not expect this correlation to compare well with short pin fin data at high Reynolds numbers where the large differences in H/D ratio should have a significant impact. And in fact, this is precisely the behavior that is seen. In the laminar region, the Zukauskas correlation matches the experimental data very well for all values of H/D. As the flow transitions to turbulence at approximately $Re = 10^3$, the general correlation over-predicts all the short pin fin data as would be expected based on **Figure 4.8**.

Metzger et al. (1982A) studied a series of seven cylindrical pin fin array configurations. All arrays were based on H/D of 1.0 and S_T/D of 2.5, with stream-wise pin pitch (S_L/D) varying from 1.05 to 5.0. They proposed essentially the same dependence on Reynolds number ($f = 1.76Re^{-0.318}$) as the current study, but only for $Re > 10^4$. Below this, they found an exponent of ($\alpha_1 = -0.13$) to be more appropriate. This can be seen in **Figure 4.9** where the current data, particularly for H/D = 1.0 which is essentially the same as that of Metzger's arrays, is in quite good quantitative agreement, particularly through the upper half of the Re range considered in this study.

The data of **Short (1994),** on the other hand, demonstrates essentially the same slope as the current data for H/D = 0.5, despite the fact that Short's data was based on an aspect ratio of almost 2.0. Quantitatively however, Short's data is

considerably different from the current data as well as from the other previous studies.

The most recent data presented is that of **Siu-Ho et al. (2007)**. Their data differs from the others in that it was generated from a micro-array of square pin fins, approximately one twentieth the scale of the current arrays. This data also exhibits approximately the same Reynolds exponent, though it exhibits somewhat higher magnitude as compared to the current data and that of the Zukauskas correlation. Given that the Siu-Ho array consists of square rather than circular pins, this somewhat larger pressure loss appears reasonable and consistent with what one would expect.

4.2 Array Heat Transfer

The mean heat transfer results presented here are derived from endwall liquid crystal measurements except where noted. The mean endwall temperature and bulk fluid temperature are used as the basis for calculating the heat transfer according to the procedures set forth in **Sections 3.3 – 3.5**.

4.2.1 Observed Mean Heat Transfer

Figures 4.10 depicts the dimensional performance of the three arrays in terms of the projected area based mean heat transfer coefficient (h_{Ap}) verses mass flow rate ($\dot{m}$). It must be noted that for the case of H/D = 0.5, liquid crystal based data is not available at C = 0 and C = 6. At these conditions, array temperatures under test fell

outside the liquid crystal calibration range, and therefore did not produce valid results.

In this form, the heat transfer coefficient is based on a constant footprint area (A_p) of 3570 mm^2 regardless of the clearance or pin height. This definition reflects the behavior of the overall performance of the array as would be experienced by a heat source, such as a power semiconductor chip, mounted on the base plate. Though there are a handful of exceptions, the general trend is towards a lower rate of heat transfer at each successive increase in tip clearance. This occurs despite an increase in actual heat transfer area when the tips become exposed. This suggests that, on a flow rate basis, the reduction in local fluid velocity caused by the added flow area above the pins is the dominant factor in determining the overall heat transfer rate.

Figures 4.11 presents the heat transfer results in terms of wetted area (A_w). This form of the data reflects conditions locally within the array, rather than the "far-field" perspective represented by h_{A_p}. While the general trend is the same, because the associated heat transfer area increases significantly when clearance is introduced due to the addition of tip area, the heat transfer rate appears to be reduced more significantly when clearance is added. When considering the results in these terms, it is important to recognize that while mass flow rate remains constant, the cross-sectional area of the channel increases with introduced tip clearance. This results in lower local velocities within the array which in turn will promote lower heat transfer rates and lower pressure losses. Therefore, in order to compare the impact of clearance across equivalent hydrodynamic conditions, it is necessary to formulate the heat transfer and flow rate in non-dimensional terms.

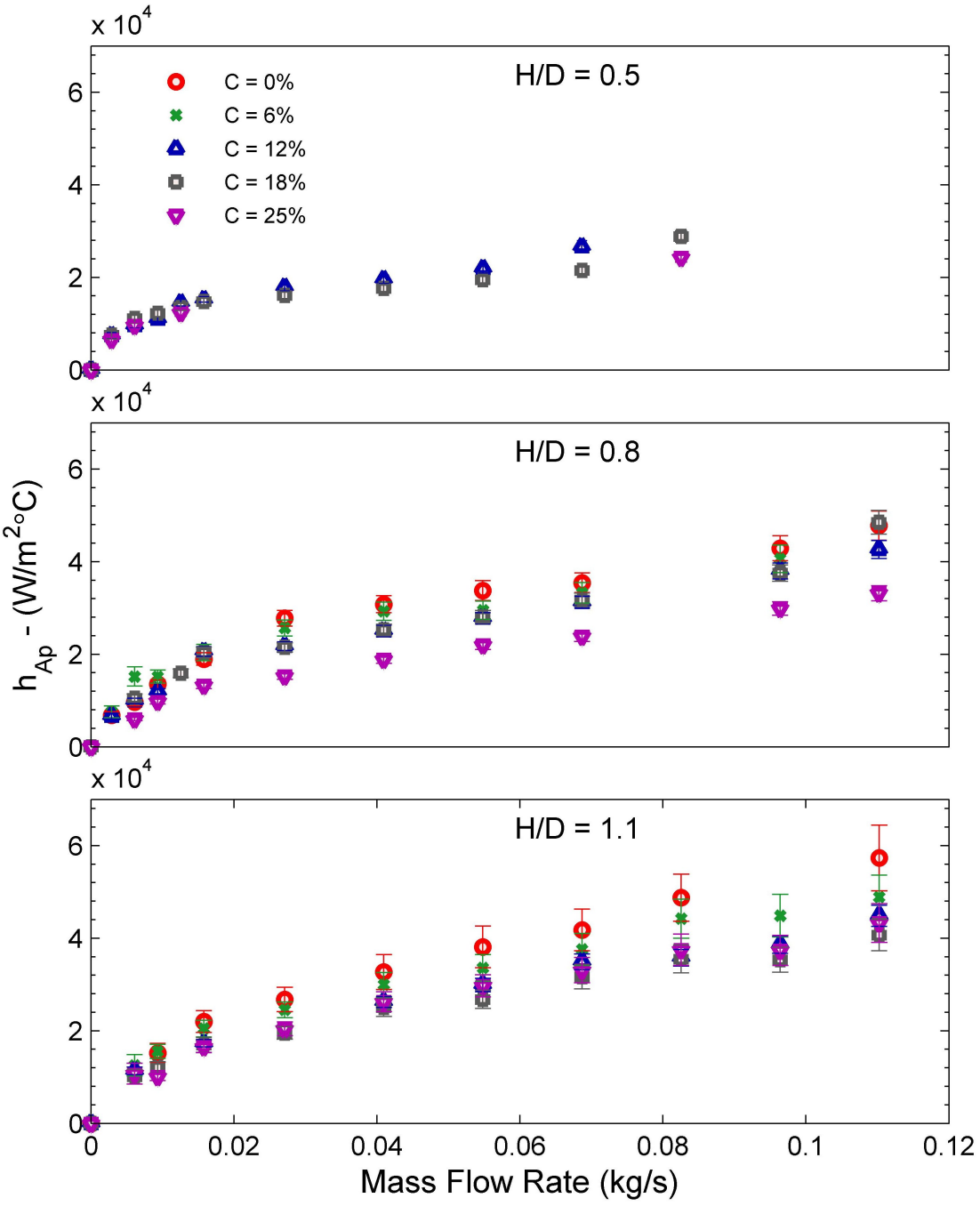

Figure 4.10: h_{A_p} *vs.* $\dot{m}$ for each value of H/D and C

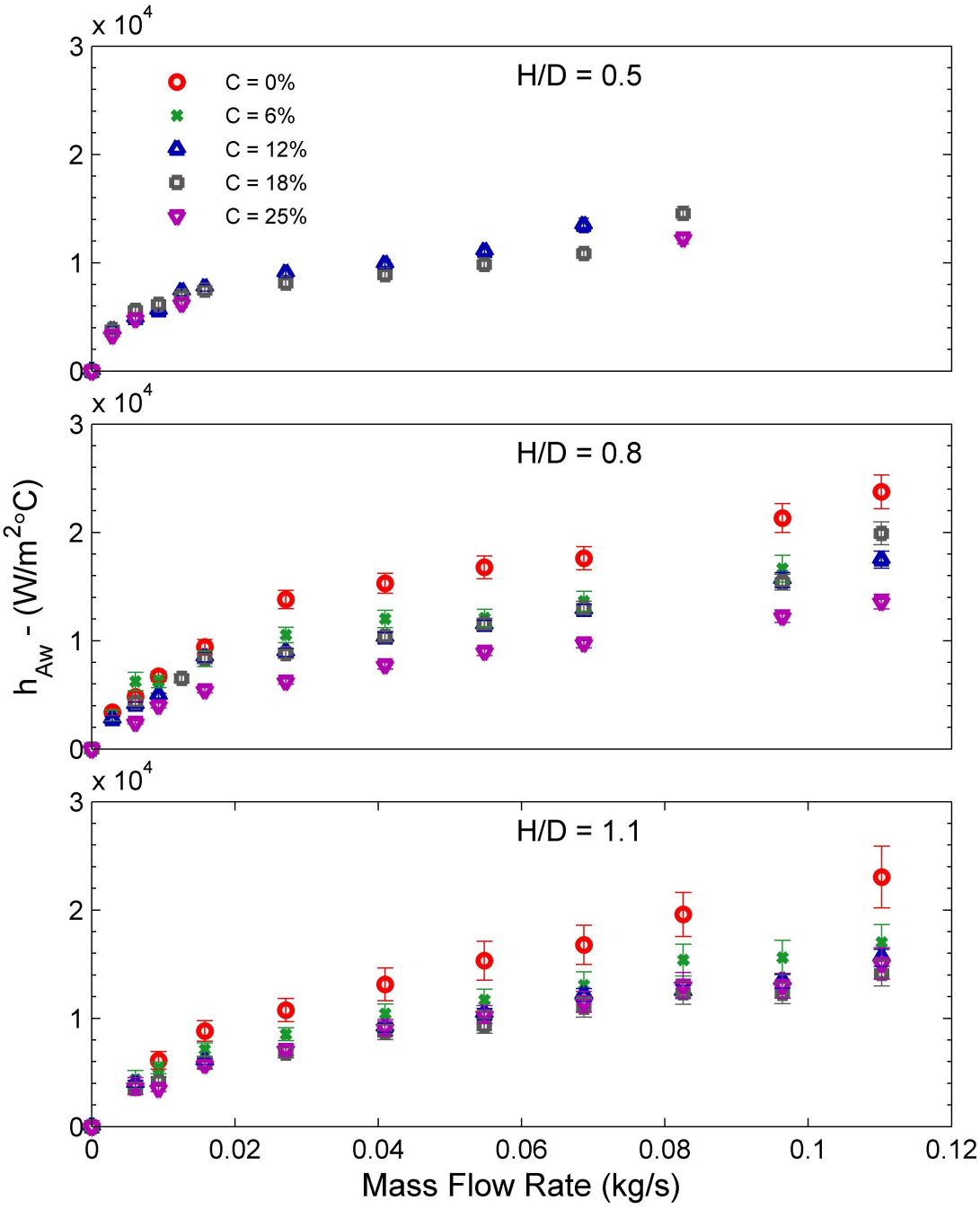

Figure 4.11: h_{A_W} *vs.* $\dot{m}$ for all H/D and C

Figures 4.12 presents Nu_{A_P} as a function of Re through a range of tip clearances for each case of H/D. While the results do show an increase in heat transfer over the non-clearance case in some instances, a clear and consistent

relationship is not apparent. In the case of H/D = 0.8, improvements in heat transfer were seen for all cases except for the highest level of clearance, while for H/D =1.1, C = 25 % out performs the non-clearance case.

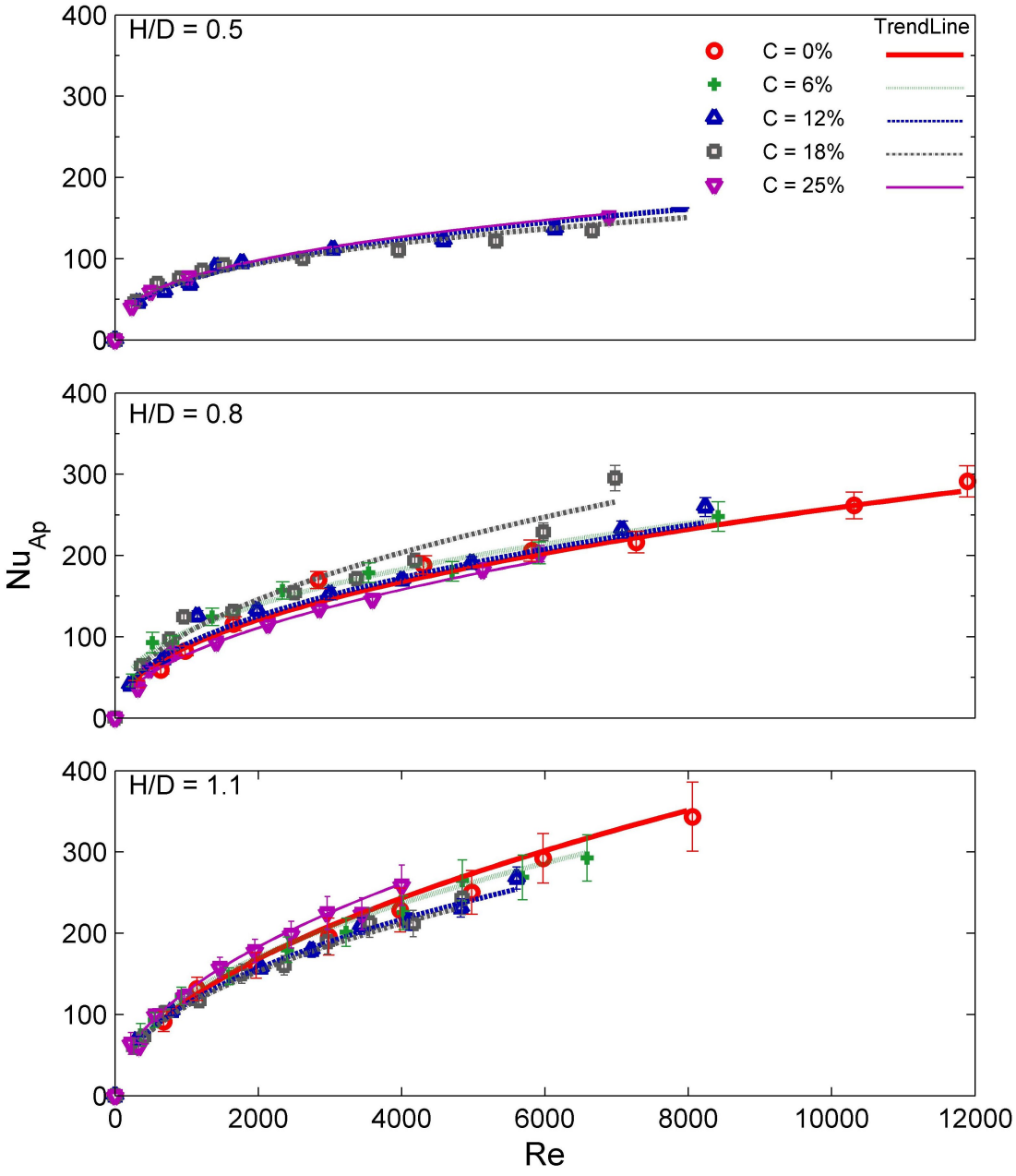

Figure 4.12: Nu_{A_P} *vs.* Re for all H/D and C

Figure 4.13 depicts dimensionless heat transfer based on wetted surface area as a function of Reynolds number. In theory, a step change in wetted area occurs between the non-clearance case and those with tip clearance. However, realistically, with a sufficiently small tip clearance, the tip area will remain effectively shrouded,

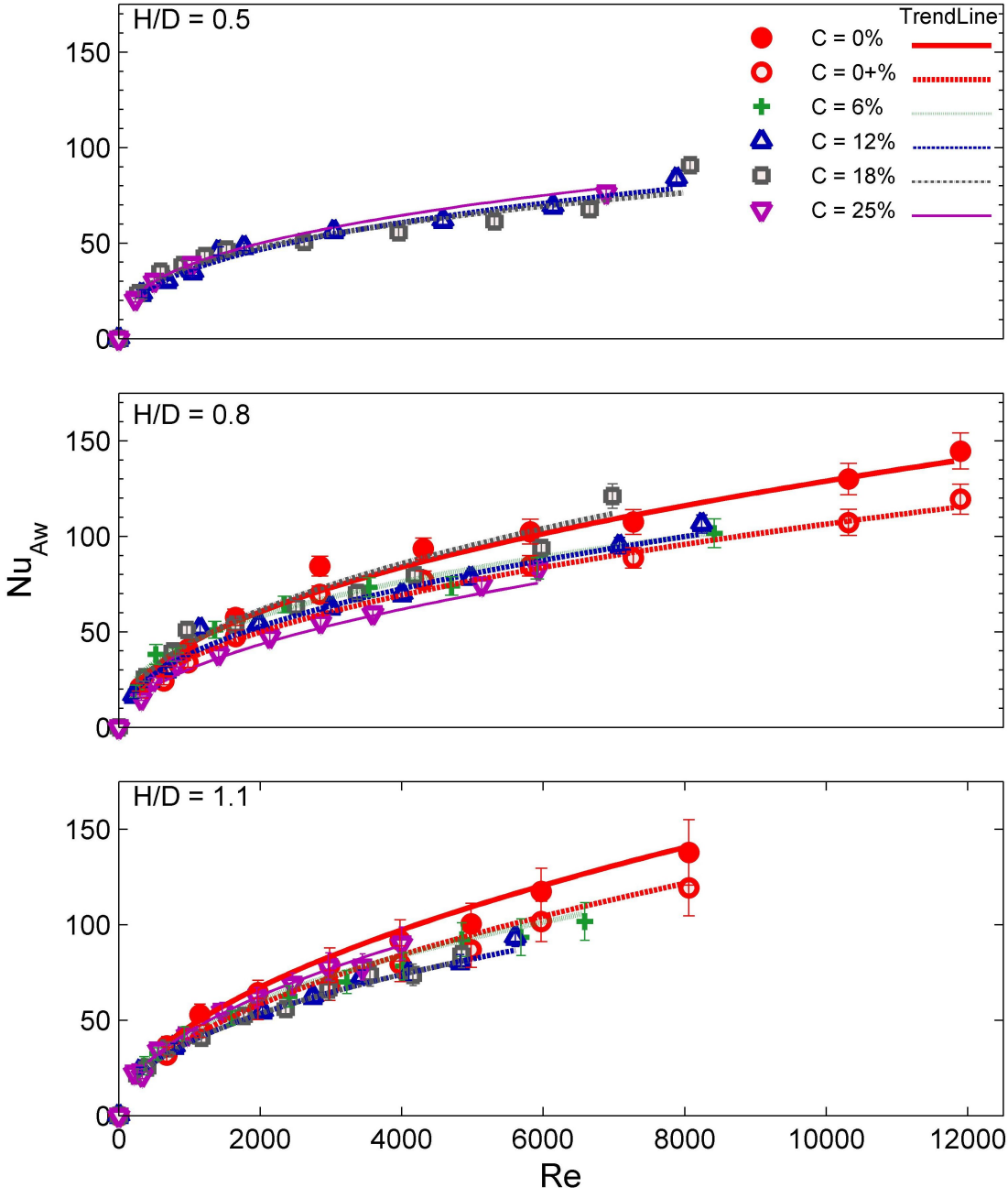

Figure 4.13: Nu_{A_w} *vs.* Re for all H/D and C

with the tip area producing little or no heat transfer to the cooling fluid. To illustrate the limits of this behavior, two separate performance curves are depicted in the figure for the non-clearance case. The C = 0 data points are based on a wetted area that does not include the tip area, while the C = 0+ data points are based on a wetted area that does include the tip area. The C = 0+ case therefore based on the same area as the clearance cases. In all but one case, the addition of clearance produces reduced heat transfer relative to the C = 0 case. Only for H/D = 0.8 and C = 18 percent is an increase indicated, and the magnitude of this increase is well within the margin of uncertainty for the data. If the C = 0+ data is used as the basis of comparison, then the same trends as were observed in Figure 4.12 hold true.

Taken as a whole, the results of **Figures 4.10 – 4.13** suggest that while improvements in heat transfer can be achieved on an equivalent Re basis by employing a clearance gap, the primary contributor to this enhancement is the introduction of more heat transfer area to the array. There is little or no evidence that the gap produces any significant changes in the characteristic of the flow to produce an increase in the local rate of heat transfer.

4.2.2 General Correlation of Array Mean Heat Transfer

To generalize the results further, additional post-processing of the data is performed to account for conduction related temperature gradients along the lengths of the pins. The process outlined in **Section 3.4.3** was employed to estimate pin efficiencies for each individual test point. **Figure 4.14** depicts the calculated efficiencies for the three pin heights and five clearance sets.

Figure 4.14 presents some surprising results. Apparent efficiencies ranged from approximately 75 percent to 95 percent. However, the observed behavior of each array is considerably different from one another and in the case of H/D = 0.5 the results, at least at first glance, are rather counter-intuitive.

At an H/D of 0.5, all three clearance cases appear to exhibit a slight increase in pin efficiency with increasing Reynolds number, which is opposite what one would expect. This may be an indication that, for the given clearance set, all of which are relatively small for this case, the tip area, which represents a significant fraction of the overall heat transfer area of the pin, is able to contribute to the heat transfer at lower Re as the cooling fluid navigates between the shroud and the pin tip. At the higher flow rates, the flow constrictions of the pin gap may be causing the cooling fluid to bypass the exposed tip areas, thus reducing the tip region heat transfer. This in turn produces a decreased differential temperature across the pin. On the other hand, the observed efficiencies may simply be an artifact of the data, due to the relatively small pin aspect ratio and the fact that the temperature profile within the pin may vary significantly from the one-dimensional linear profile that was assumed for the purpose of analysis.

The behavior for H/D of 0.8 and 1.1 are more consistent with what one might expect, with a general decrease in efficiency with increasing Re, and a tendency for all clearance cases to converge at high Re, given that it has already been shown that the impact of clearance tends to diminish with increasing Reynolds number. The large disparity between the non-clearance case at H/D = 1.1 and all the clearance cases may

be indicative that the pin tip area becomes fully engaged in heat transfer at the lowest clearance setting for this case.

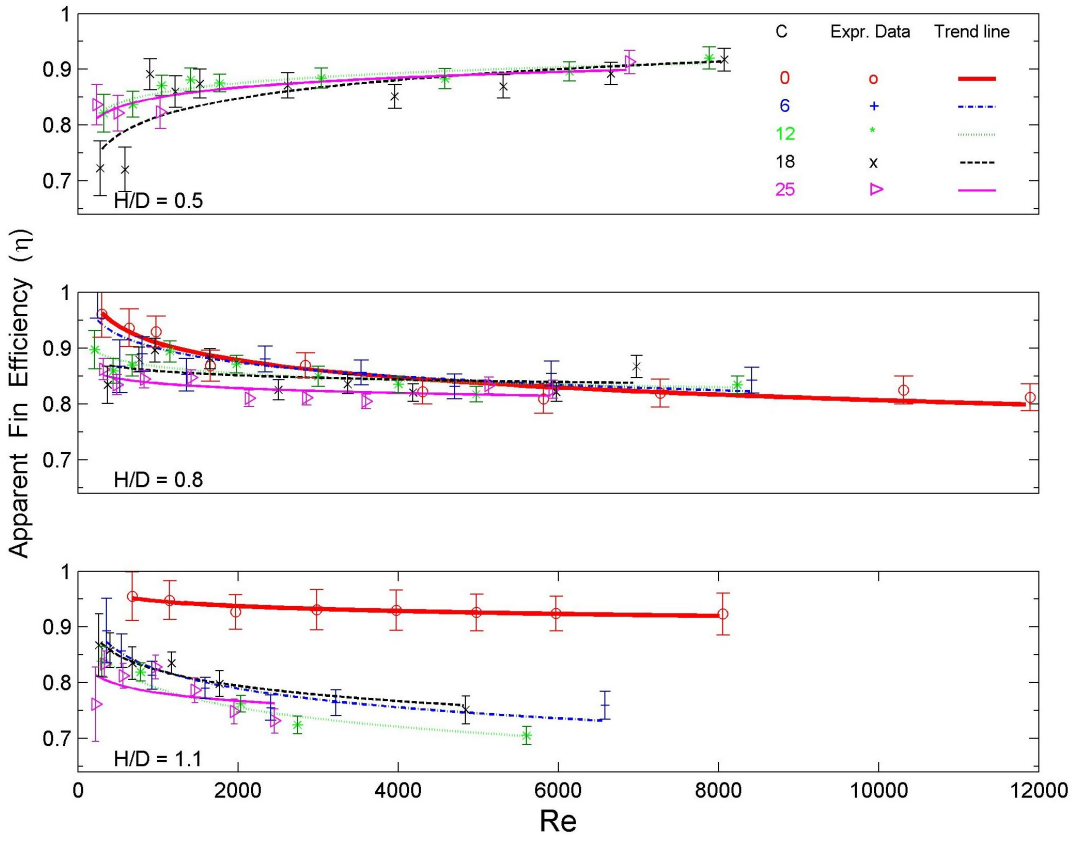

Figure 4.14: Estimated pin efficiencies

The data of **Figure 4.14** is next applied to the measured heat transfer results to determine equivalent performance for each operating point based on 100 percent pin efficiency. **Figures 4.15** and **4.16** show the efficiency corrected data for heat transfer based on the projected and wetted surface areas respectively. This serves several purposes. For one, it helps to de-convolute the effects of conduction temperature losses along the pin length from other convective effects that arise when tip clearance is present. Also, normalizing based on 100 percent efficiency brings the data in this

study in line with numerous other pin fin studies that employed naphthalene sublimation to infer heat transfer rates based on mass transfer results, as this approach, by its nature, corresponds to a 100 percent fin efficiency.

Figure 4.15 results, which are based on projected area, show clearance to have a consistently positive effect on overall heat transfer. This suggests that highly conductive pin fin arrays, such as those made of copper would benefit the most from tip clearance enhancements.

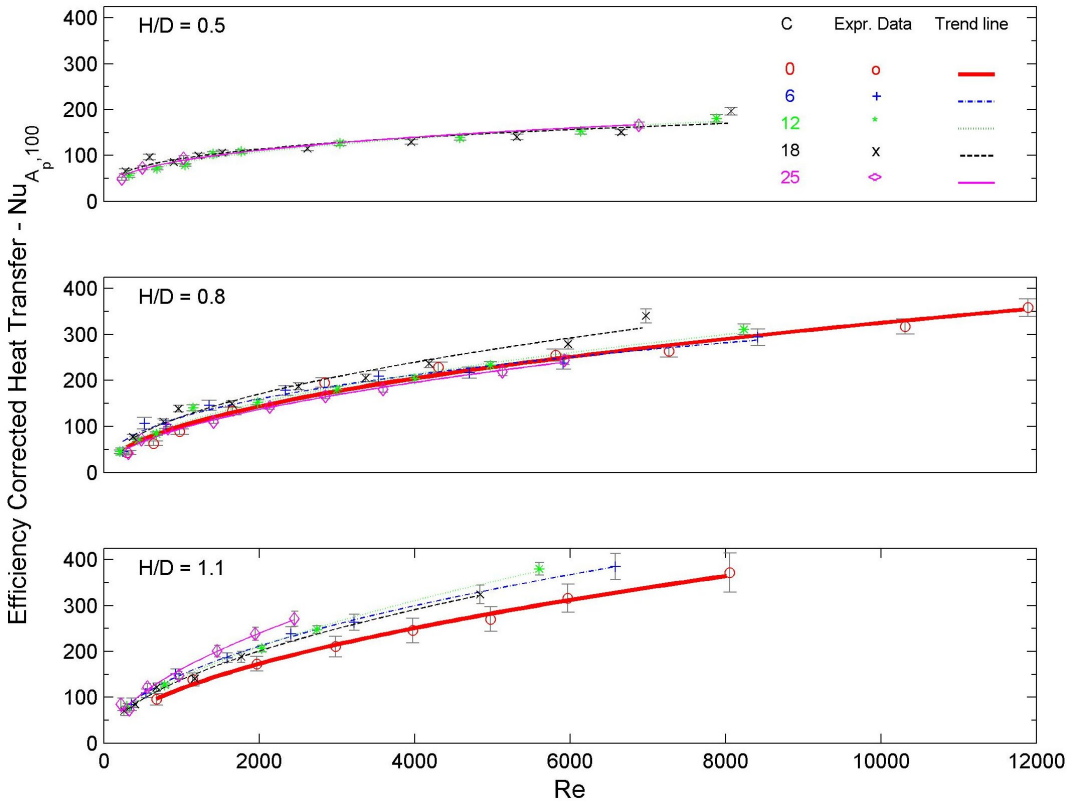

Figure 4.15: Efficiency corrected heat transfer results, A_p basis

The results of **Figure 4.16** on the other hand, display the impact of clearance on local heat transfer when conduction effects are accounted for. It is interesting to note that once area differences (both heat transfer area and flow area) and conduction

effects are accounted for, in the case of H/D = 0.5 and 1.1, the vast majority of the data collapses onto a single profile. This suggests that either the tip area contributes to the overall heat transfer at roughly the same rate as the lateral surfaces, and that no significant enhancements are imparted to the flow field as a result of the tip clearance, or if such enhancements do occur, they are roughly equivalent to any difference between the lateral surface contribution and that of the tip area. In either case, from a purely practical standpoint, any advantage that might be obtained from shroud gap appears to be, at best, directly proportion to the amount of heat transfer area added to the array as a result of the tip clearance.

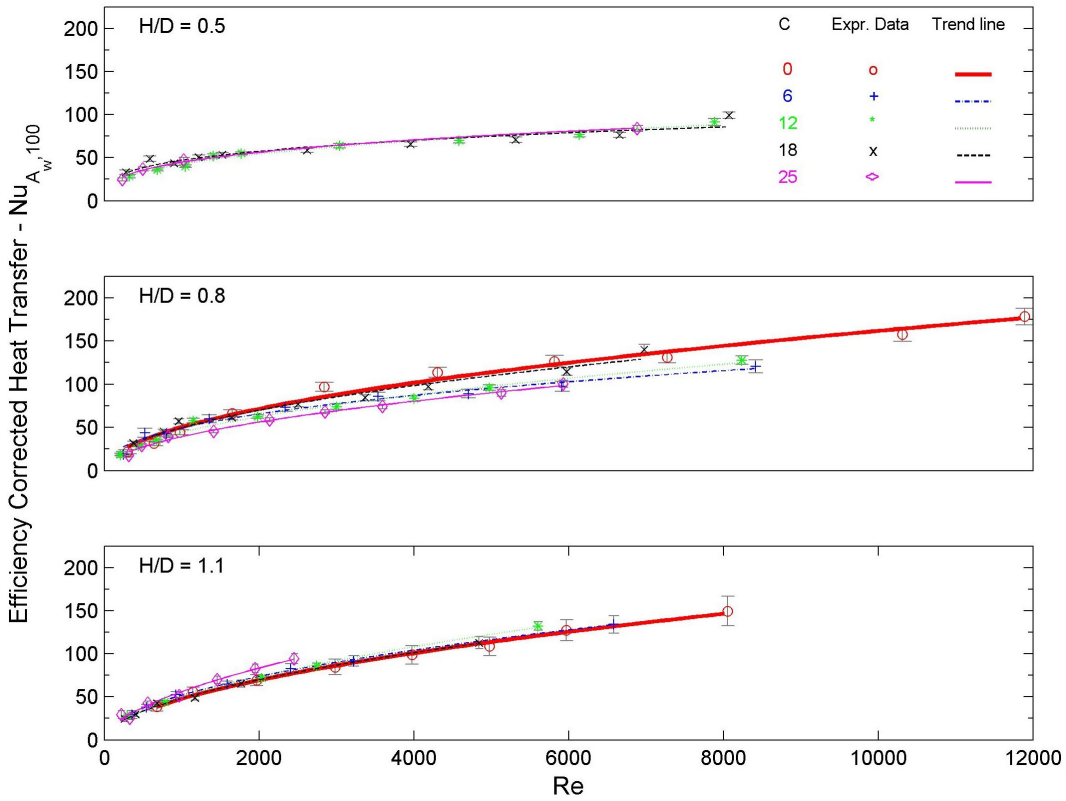

Figure 4.16: Efficiency corrected heat transfer results, A_w basis

Next, to correlate the data for all combinations of pin height and tip clearance, a nonlinear multiple regression analysis is performed using NLREG, **(Sherrod, 2001)**. As discussed in **section 3.4.4**, the presumed form for a general correlation for heat transfer is taken to be:

$$Nu_{A_w,100} = \alpha_0 \left(\frac{H}{D}\right)^{\alpha_1} \left(1+\frac{Cg}{D}\right)^{\alpha_2} \mathrm{Re}^{\alpha_3} \tag{4.5}$$

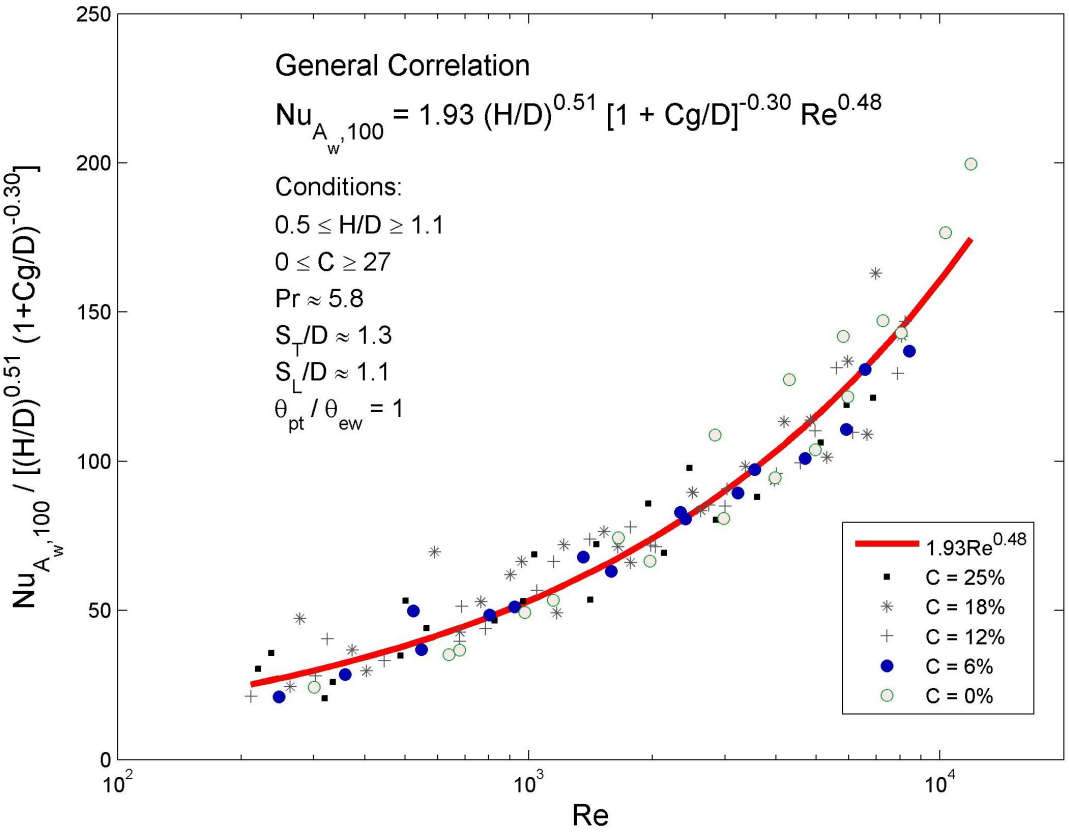

Figure 4.17: General correlation of heat transfer

Figure 4.17 illustrates the data spread relative to the assumed relationship. The empirical model predicts the experimental data to within ± 22.5 percent at a confidence level of 95 percent for all values of H/D and C, which is significantly

better than the same correlating form was able to achieve in terms of pressure drop (see **Figure 4.3**). Also, the heat transfer data does not exhibit a significant bias towards a particular clearance set as was seen with the pressure drop data. In this case, the relationship appears to perform equally well at all values of C.

Separate correlations to each set of clearance data was attempted to see if there was a similar relationship between the correlation exponents and tip clearance as was noted in **Table 4.2** for the friction factor correlation. However, no particular trends were indicated.

4.2.3 Heat Transfer vs. Pumping Power

The previous sections have illustrated the impact of clearance on overall pressure drop and heat transfer on both a constant flow rate basis as well as an equivalent flow field (constant Re) basis. Because forced convection liquid cooling systems require a pump, and because that pump can represent a significant portion of system cost both in terms of initial investment, operating costs, and even maintenance costs, a practical engineering consideration would be the behavior of heat transfer relative to tip clearance for a given pumping power. Employing the empirical correlations for *f* and Nu as defined in sections 4.1.1 and 4.2.2 respectively, **Figure 4.18** illustrates the expected relative change in heat transfer for each clearance setting when compared to the case with no clearance assuming the same pumping power in both cases. The results have been plotted on the basis of Re_{c0} which is the Reynolds number associated with zero tip clearance. Given that no heat transfer results were

available for Cg/H = 0 and 6 percent for H/D = 0.5, results could only be calculated for the arrays of H/D = 0.8 and 1.1.

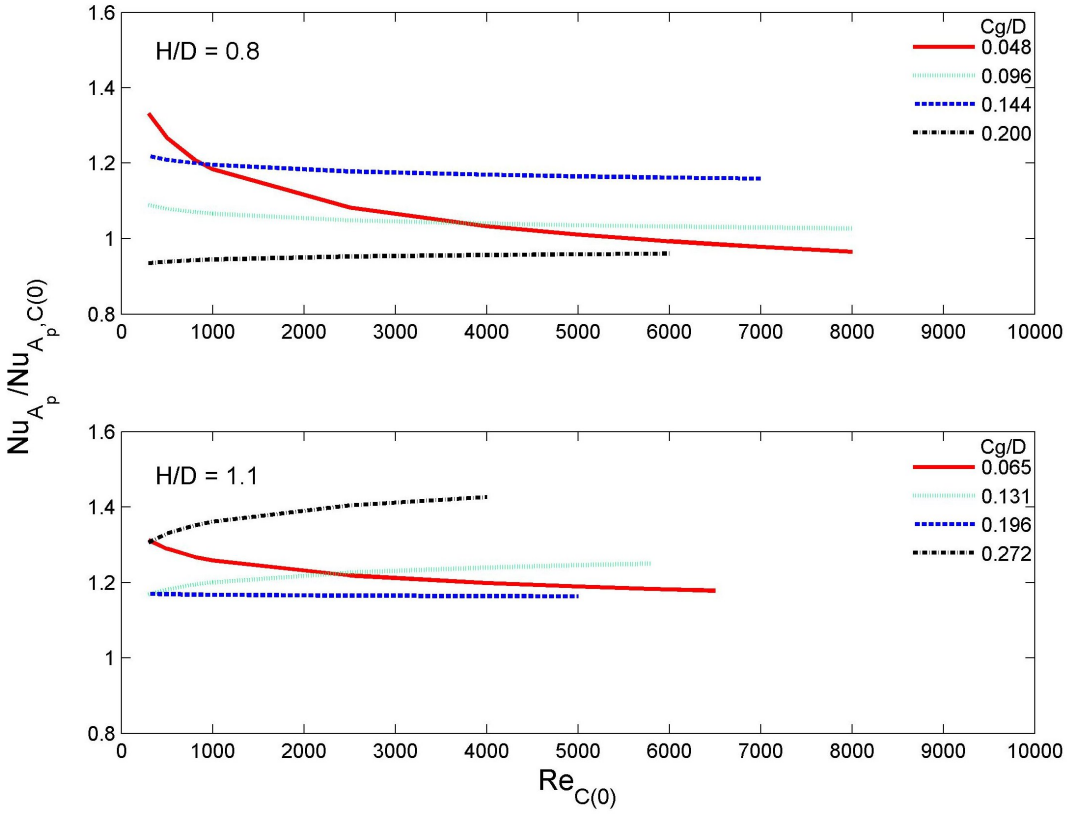

Figure 4.18: Impact of clearance given a constant pumping power

Figure 4.18 paints a complex picture, but several relationships are evident. In the case of H/D = 0.8, the minimum clearance gap results in an improvement in relative heat transfer up to 35 percent in the laminar region, but gradually decreases until it dips below unity around Re = 6000. Successive increases of Cg/D to 10 and 14 percent exhibit both a reduction in the rate of change in relative heat transfer across the given Re range, combined with a trend towards increased relative heat transfer for all Re. This is likely an indication that the tip area becomes fully engaged

in heat transfer between these two clearance gaps. At the maximum clearance of Cg/D = 0.2, a significant reduction is observed at all Re, with relative heat transfer slightly below unity. In the case of H/D = 1.1, similar trends are apparent with the exception of Cg/D = 0.27, which was observed to produce upwards of a 40 percent increase in $Nu_{A_P,100} / Nu_{A_P,100,C(0)}$ through the majority of the range.

4.2.4 Comparisons with the Literature

4.2.4.1 Nu vs. Re

As with the pressure drop performance, there is relatively little heat transfer data available in the literature based on arrays with tip clearance. The only work with which to compare is the recent numerical study of **Rozati et al. (2008)**. Based on the nature of their study, they were able to consider the local heat transfer rate at every point within the domain. They determined the change in thermal conductance K due to tip clearance relative to an open channel, with pumping power held constant and where K is the product of the local heat transfer rate and the computational cell surface area. The results of Rozati are depicted in **Figure 4.19**. While these results are not directly relatable to those of the current study, they do support the same basic conclusion. Through the majority of the Reynolds number range considered, the presence of a tip clearance on the order of 10 to 40 percent of pin diameter was predicted to produce increased overall heat transfer for a given pumping power, which is consistent with the results of this study as shown in **Figure 4.18**. Unlike the current study, Rozati's model, at low Re for Cg/D between 0.1 and 0.4, predicts

significant improvements in heat transfer on the order of 100 percent or more. Improvements in the current study were generally in the range of 20 to 40 percent.

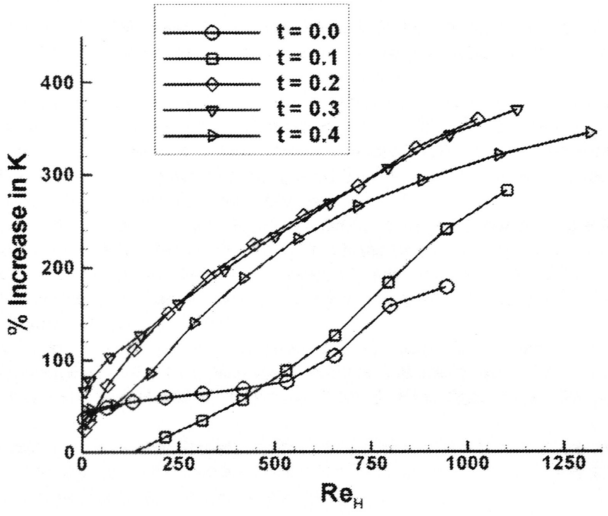

Figure 4.19: Increase in thermal conductance compared to a plane channel at the same pumping power (Rozati et al., 2008).

While Rozati's numerical work is the only effort with which to compare the effects of clearance, there are numerous empirical correlations for heat transfer from the literature that have been proposed for the non-clearance case. Appendix A.3 summarizes a series of 15 separate studies of proposed heat transfer correlations for short pin fin arrays. Some of these studies involved very specific scenarios, such as Hwang (1999A, 2001) who considered the effects of turning flow and lateral ejection which occur in turbine fin cooling scenarios, or those of Li (1996, 1998) who looked at non-traditional shaped pins including "teardrop" and elliptical shapes.

A relatively small number of these studies do present results based on staggered arrays of cylindrical pin fins with geometries similar to those considered in this study. In particular, the works of Metzger (1982A), Jubran (1993), Short (1994),

and Chyu (1999) each suggested correlations for heat transfer which can be readily compared, and they are shown in **Figure 4.20.** All four studies were based on air cooling. Therefore, key to this comparison is an assumption that the effect of fluid properties on the heat transfer within short pin fin arrays can be modeled according to a Prandtl number relationship of the form $Nu \approx Pr^{0.36}$. In order to make direct comparisons with the current data which is based on water cooling, each correlation has been modified according to this relationship assuming Pr = 0.7 in each case. This Prandtl number relationship is based on the work of Zukauskus, who determined that $Pr^{0.36}$ was the most appropriate model in accounting for the effect of fluid properties on the heat transfer across cylindrical tube bundles in cross-flow. In the absence of any definitive studies specific to pin fin arrays that suggest differently, adoption of the $Pr^{0.36}$ relationship is common practice among researchers. Data corresponding to H/D = 1.1 and C = 0 is used as it is the closest match geometrically, to the arrays considered in the previous studies.

Overall, there is very good agreement between the current study and the results of both Metzger and Chyu. In the case of Metzger et al., they observed a somewhat steeper Re relationship resulting in good agreement in the low Re range, but increasingly divergent results at higher Re. The results of Chyu on the other hand, exhibit essentially the same Re relationship, but suggest somewhat higher levels of heat transfer at a given Re. In both cases, the major geometrical difference between the current study and those of Metzger and Chyu is the pin pitch, which was moderately larger than those considered in this study. The fact that both studies observed higher rates of heat transfer given these larger pitches, is somewhat counter-

intuitive as one would expect a more densely packed array (ie the current study) to perform more effectively in terms of heat transfer.

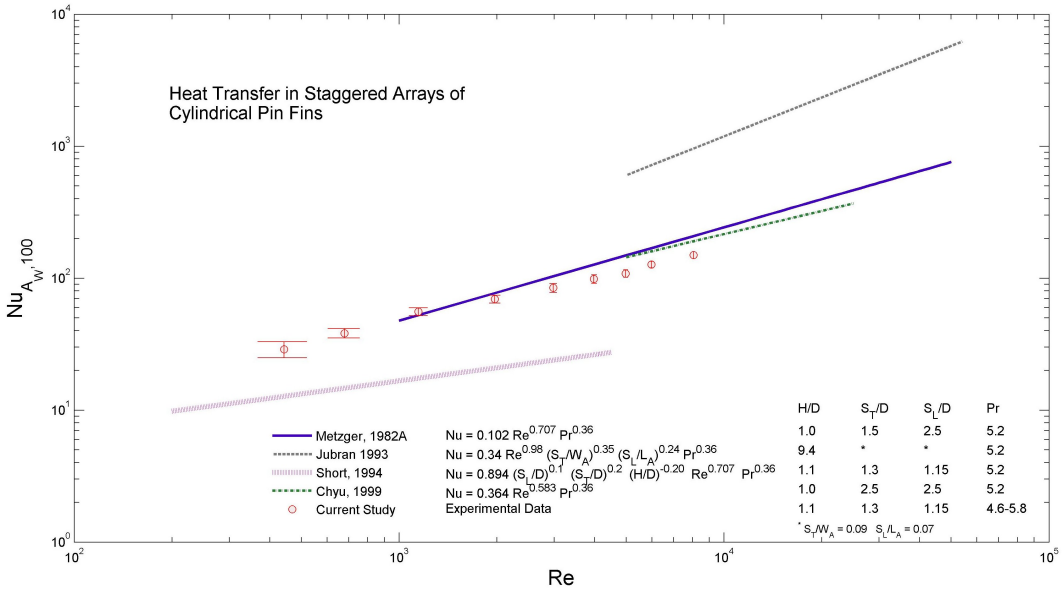

Figure 4.20: Comparison of current heat transfer results (no tip clearance) to available data in the literature.

Short considered a wide range of pin spacings and H/D values in his experiments. He was therefore able to propose a more general correlation that takes into account the effect of these variables, similar to what Zukauskas proposed for tube banks. However, when applying this correlation to the present array, the agreement is quite poor, with a 4 to 5 fold difference in some cases. It should be noted that while the H/D range employed in Short's work includes those used in this study, the pin pitch of the current arrays is outside what Short considered. So applying his correlation to this geometry may not be appropriate and may be contributing in part, to the large discrepancy.

Jubran also considered a wide range of pin pitches, though not down to the levels used in this study. As a result, their model has been extended beyond its original limits. Also, Jubran's arrays were at an H/D ratio of 9.44, which is significantly different than the current study or any of the other studies. As one would expect of a correlation based on larger aspect ratio fins, the correlation over-predicts the current low-aspect ratio pin data significantly.

4.2.4.2 Nu vs. H/D

The key performance characteristic of short pin fin arrays that differentiates them from tube bundles is the impact of aspect ratio on overall mean heat transfer rates. As noted in Chapter 1, Theoclitus (1966) was among the first to show that short pin fins underperformed relative to long tube bundles, particularly when H/D < 20. Brigham and Van Fossen (1984) also looked at this aspect and found consistent reductions in heat transfer with decreases in aspect ratio between H/D = 8.0 and H/D = 2.0, but found that heat transfer was not a strong function at smaller aspect ratios down to H/D = 0.5.

Table 4.3 summarizes the results of the current study showing the impact of H/D for the non-clearance case and for a typical tip clearance case. For the case of zero clearance, the results are consistent with previous studies. In both the laminar and transitional regions, the overall heat transfer is relatively unchanged with aspect ratio, varying by less than ten percent, which is well within the uncertainty limits of the experimental data.

In the case of 18 percent tip clearance, the heat transfer rates are all within ten percent of one another in the laminar region, but differ significantly in the transitional region, with Nu decreasing by 36 percent between H/D = 1.1 and H/D = 0.5. Because no data is available for the case of H/D = 0.5 in the non-clearance case, it is not possible to determine if heat transfer in general was lower at H/D = 0.5 in contrast to what Brigham and Van Fossen observed, or if the reduced performance is a consequence of tip clearance.

Table 4.3: Comparison of Nu vs. H/D

H/D	C (%)	Re	$Nu_{A_W,100}$ (W/m^{2}K)
0.5	**0**	**500**	**-**
0.8	**0**	**500**	**33.3**
1.1	**0**	**500**	**35.9**
0.5	**0**	**5000**	**-**
0.8	**0**	**5000**	**116.3**
1.1	**0**	**5000**	**115.3**
0.5	**18**	**500**	**38.7**
0.8	**18**	**500**	**34.9**
1.1	**18**	**500**	**33.3**
0.5	**18**	**5000**	**75.5**
0.8	**18**	**5000**	**107.8**
1.1	**18**	**5000**	**118.3**

4.2.5 Local Heat Transfer

As discussed in **Chapter 3**, the liquid crystal techniques employed in this study produced uniform and consistent hue-to-temperature relationships at the unit cell level, but exhibited significant variations in hue from pixel to pixel within a unit cell, at a given calibration temperature, especially at the larger values of H/D. Because of this, accurate heat transfer predictions were limited to unit-cell based

results and no attempt was made to quantify temperature or heat transfer with any greater spatial resolution. But while quantitative results were not supported, the visual nature of the liquid crystal technique provided some qualitative results worth reviewing.

Figures 4.21 – 4.23 illustrate the general character of the array temperature field with and without tip clearance. In each figure, the case corresponding to no clearance is on the left, while that with clearance is shown on the right. Details of the flow conditions are given in **Table 4.4**. Flow is from bottom to top in each image. The images of **Figure 4.21** are original liquid crystal color photographs for H/D = 0.8. The flow conditions (Re) are nearly identical and the heat flux ($\dot{q}''$) is comparable in both cases, although not exactly the same. The yellow regions correspond to lower temperatures, while the green and blue areas represent increasingly warmer regions. **Figure 4.22** depicts a false color image, which maintains the same basic patterns as the original, but with a color scheme that is perhaps more intuitive in terms of the local thermal conditions. In these images, the RGB value of each pixel has been transposed with its complimentary value, resulting in a color scheme in which blue represents cooler regions and red defines the warmer areas. These images have also undergone a tonal transformation intended to enhance the contrast between features. This brings to the foreground characteristics which appear more subtle in the original photographs due to the muted nature of the liquid crystal color response. Finally, the images in **Figure 4.23** in turn are grayscale hue images. The images were produced by converting the original RGB image to an HSV basis, normalizing the components of each pixel on a scale of 0 to 1, and generating a

gray scale bit image using only the hue component. Since the liquid crystal temperature is related to hue, this provides a 2-D mapping that is more directly proportional to the temperature field than the other sets of images.

Table 4.4: Specifications for Images in Figures 4.21 – 4.23

	Left Image	Right Image
Image ID	090301_607	081301_168
H/D	0.8	0.8
C	0	18
Re	1382	1384
$\dot{q}''_{A_P}$ (W/cm^2)	6.50	7.36

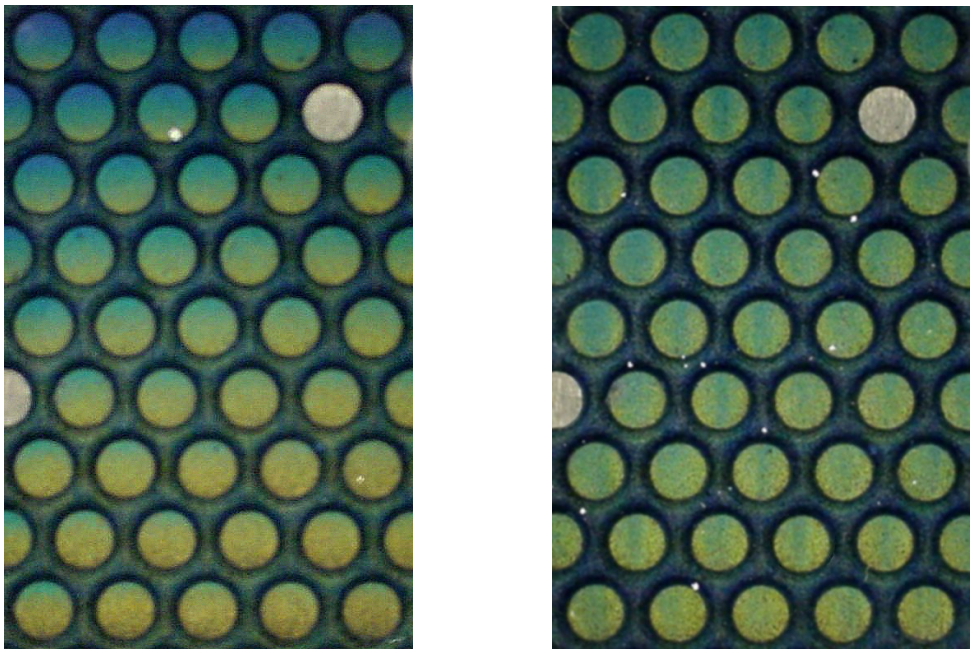

Figure 4.21: Original liquid crystal images at Re = 1380 for C = 0 (left) and C = 18 right. Flow from bottom to top.

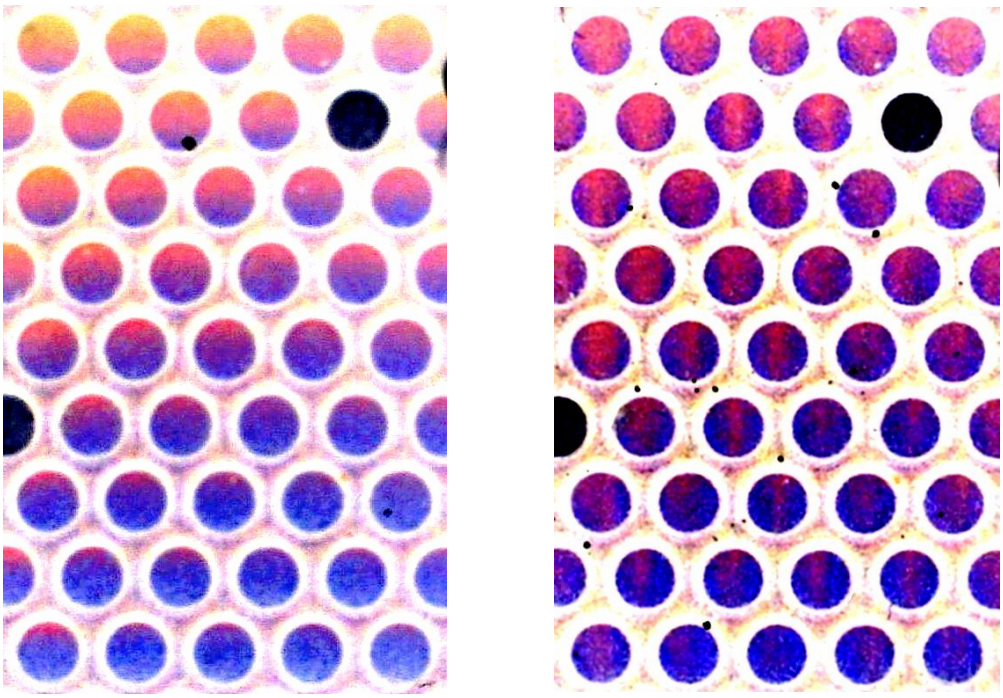

Figure 4.22: False color liquid crystal images at Re = 1380 for C = 0 (left) and C = 18 right. Flow from bottom to top.

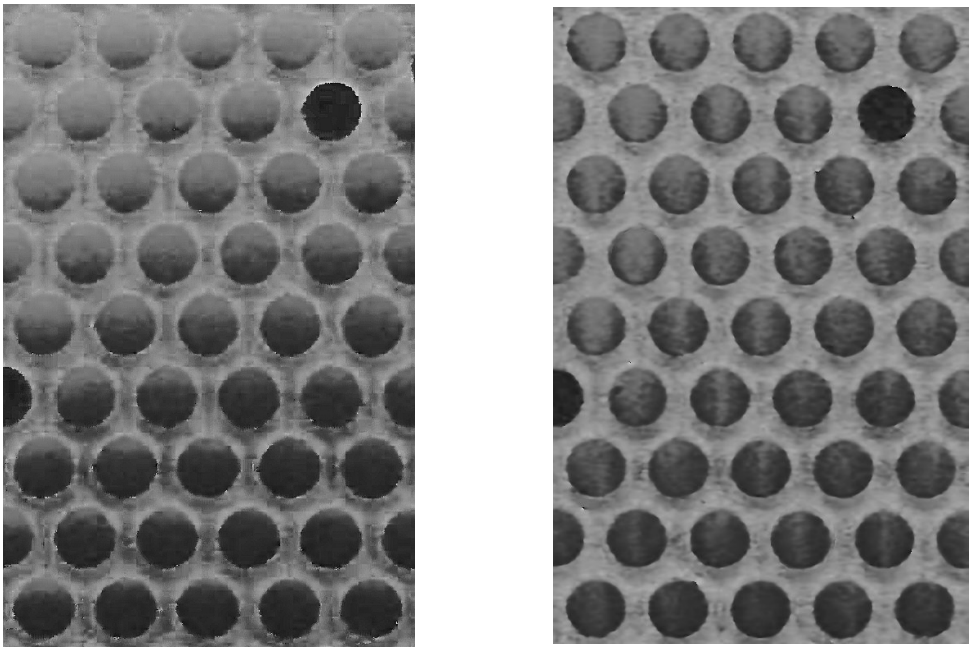

Figure 4.23: Grayscale hue based images at Re = 1380 for C = 0 (left) and C = 18 right. Flow from bottom to top.

When no tip clearance is present, it was observed that the hue profile of the pin tips tends to exhibit a horizontal nature. That is, the leading edge of each pin is cooled to the greatest extent and the pin temperature increases uniformly across the tip in the direction of mean flow. In contrast, the general character of the hue field with clearance present (C = 18) as shown in the image on the right, is vertical in nature with the left and right edges being cooled to a greater degree, while a central strip situated along the flow length of the tip is relatively hotter. In general, the temperature field in the case of C = 6 and C = 12 corresponded to that for C = 0, while the case of C = 25 was general similar to that of C = 18.

This indicates a basic difference in the nature of the flow field between the two cases. With no tip clearance present, the cooling fluid impinges on the leading edge of the pin, thereby providing the highest heat transfer rate and lowest temperature at that location. At C = 6 and 12, the gap above the tip is too narrow to allow significant amounts of flow across the top of the pin, and the exposed area remains essentially isolated from the flow. Beyond these gaps, the fluid begins to flow across the pin tips, although with less than complete coverage.

Figure 4.24 illustrates the calculated two-dimensional temperature field based on the liquid crystal data for a central region of the pin tip with no clearance present. The trailing edge, which is relatively sheltered from the stream, sees a lower rate of convective heat transfer and is hotter as a result. The uniformity of the temperature profile perpendicular to the mean flow direction suggests that the heat transfer coefficient experienced by the pin is relatively constant along its sides.

In the case of 18 percent clearance, the leading edge of the pin exhibits higher temperatures than the sides of the pin, with a high temperature region extending from the leading edge to trailing edge through the central part of the pin tip as illustrated in **Figure 4.25**. Not evident from the still images is the fact that this high temperature region was observed to be periodic in nature. During testing, it appeared as though "plumes of elevated temperature" traveled across the face of the pin tips at a rate of one every several seconds, being confined to the central portion of the tip.

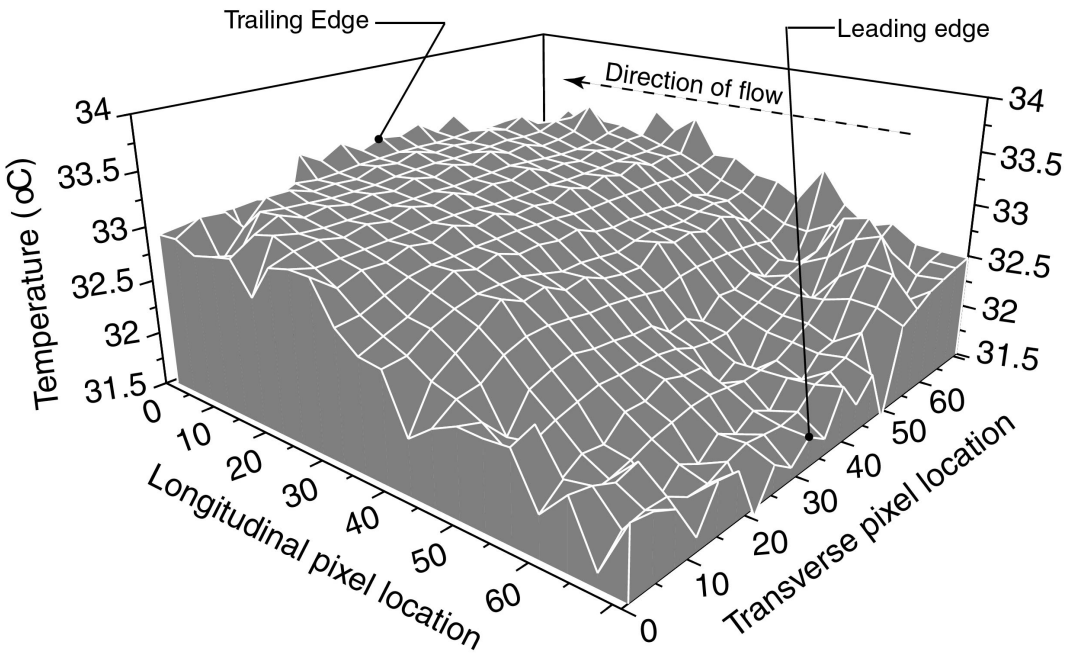

Figure 4.24: Pin tip temperature profile, Re = 1382, C = 0

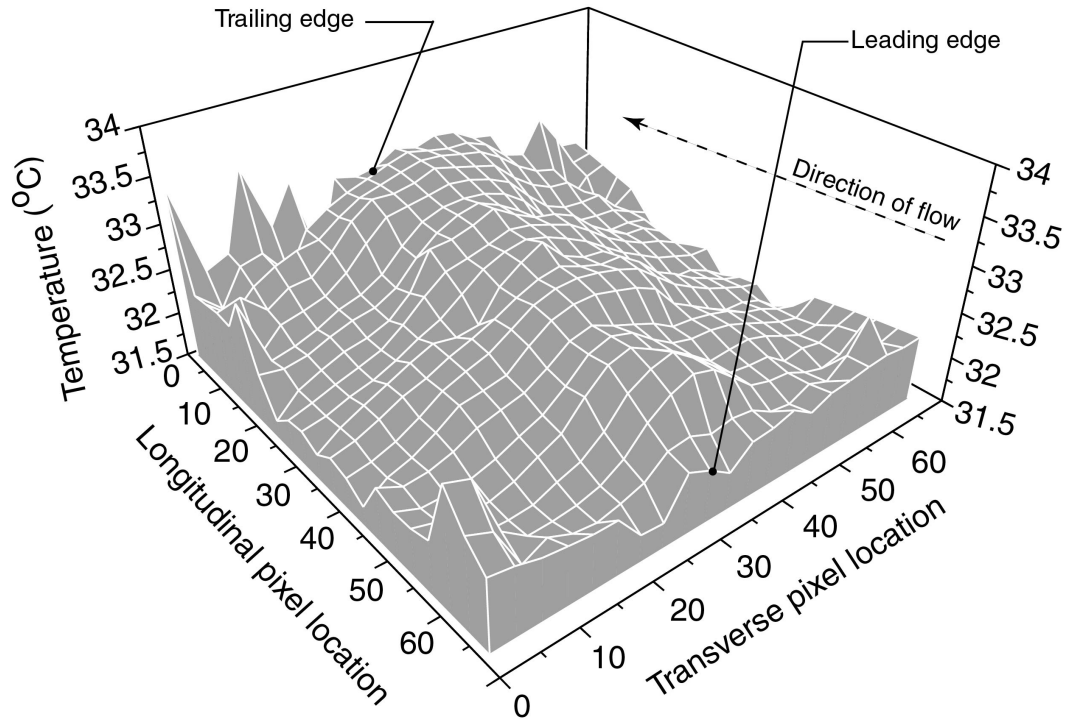

Figure 4.25: Pin tip temperature profile, Re = 1384, C = 18

This suggests the occurrence of vortices, perhaps shedding from the edges of pins in preceding rows, and then washing across the periphery of the given pin. This would produce regions of relatively high convective heat transfer where the turbulent flow passes over the pin tip, and correspondingly low heat transfer across the central region of the tip, thereby producing the observed temperature fields. Similar behavior was observed for each pin array, with the character of the temperature profiles generally evolving from apparently steady state horizontal outlines evident at low clearance, to the transient vertical plumes that were generated at higher levels of clearance.

Rozati et al. (2008) predicted similar behavior in their numerical study of tip clearance in pin fin arrays. **Figure 4.26** shows non-dimensional temperature profiles on the tips of two pins. While Rozati did not publish results for Cg/D = 0, the profile

at left is at a very low Re, which in terms of local velocity is not far removed from a non-clearance case. Like the profile in **Figure 4.24**, the numerical model suggests a relatively horizontal temperature profile across the face of the pin fin with low or no flow. And like the profile in **Figure 4.25**, with tip clearance present and a relatively moderate Re, a pronounced vertical profile structure is exhibited, with the central portion of the tip at the highest temperature. **Figure 4.27** depicts the general flow patterns that produced this behavior in the model.

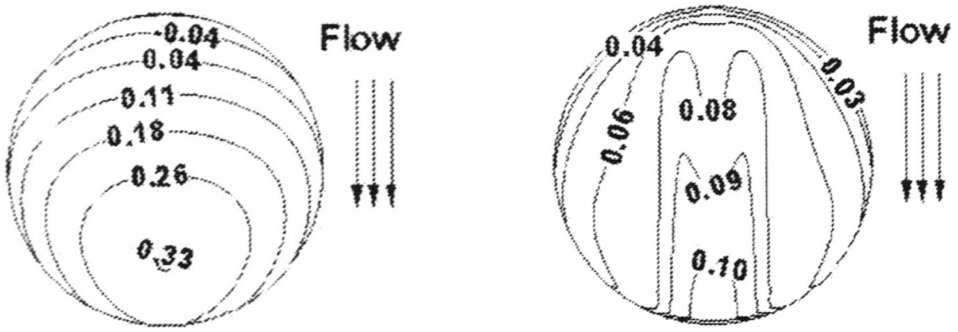

(a) (b)

Figure 4.26: Numerically predicted non-dimensional pin tip temperature profile for (a) Re = 10, Cg/D = 0.3, and (b) Re = 325, Cg/D = 0.3 (Rozati et al., 2008)

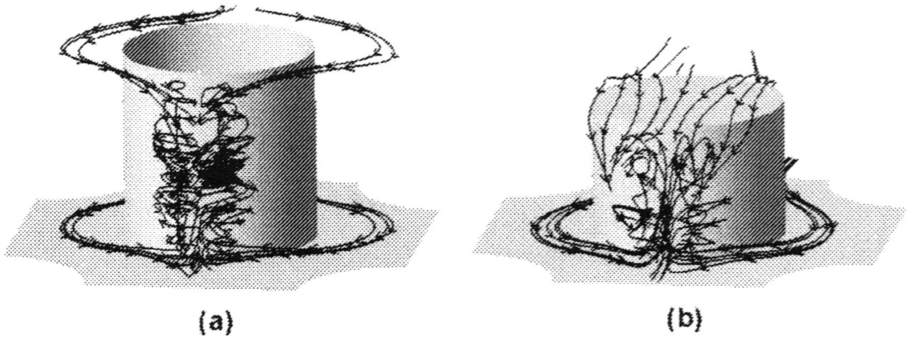

Figure 4.27: Wake time-averaged streamlines at Re = 325 for (a) Cg/D = 1, and (b) Cg/D = 0.3 (Rozati et al., 2008)

Chapter 5: Conclusions and Recommendations

5.1 Summary of Contributions

Employing arrays of short, shrouded pin fins to enhance forced convection heat transfer is a common engineering practice. For example, the approach is ubiquitous in the cooling schemes of turbine blades. And with recent advancements in micro machining and silicon fabrication techniques, the concept of applying direct forced liquid cooling at the chip level of a silicon device using micro-arrays of cylindrical or square pin fins has gained a great deal of attention of late as is evidenced by the very recent work at IBM (**Brunschwiler et al., 2008**).

While there is a great body of knowledge and research regarding cross-flow heat transfer in cylindrical arrays, and a lesser, yet substantial collection of investigations regarding the subset scenario of short pin fin arrays, only a handful of researchers have considered the role that tip clearance plays in the performance of a shrouded pin fin array. Of those studies that have looked at the impact of clearance, nearly all have involved a relatively large amount of clearance, on the order of fifty percent of pin height or greater. And while several such studies have indicated either directly or indirectly, that heat transfer augmentation may occur at small clearance gaps, none have systematically investigated this possibility experimentally.

The primary aim of this study therefore has been to provide for the first time, a systematic experimental study of pin fin array performance with and without small clearance gaps above the array. The results obtained have been presented and discussed

in terms of the impact to both the pressure drop and heat transfer performance of the array and can be summarized accordingly.

5.1.1 Hydrodynamic Behavior

Adiabatic pressure losses were recorded for a range of Cg/D from 0 to 30 percent, at H/D ratios of 0.5, 0.8 and 1.1, with Reynolds number from $2x10^2$ to $1.8x10^4$. A number of significant observations were made and are summarized as follows:

- On a non-dimensional basis, overall pressure drop was found to initially increase with the introduction of tip clearances (Cg/D) in the range of 0.05 to 0.10. At larger clearances, the pressure drop was generally found to drop below that of the non-clearance case (**Figure 4.3**). To the best knowledge of the author, this is the first time such behavior has been reported experimentally, although a very recent numerical study on the effects of tip clearance at low Re by A. Rozati et al. (2008) also predicts such general behavior.
- The impact of clearance on the non-dimensional pressure drop (*f*) was also observed to decrease with increasing Reynolds number (**Figure 4.3**). At the low end of the range considered (Re ~200), *f* was observed to be as much as fifty percent greater with clearance than without it while for Re > 5000, the presence of tip clearance appeared to have little impact on friction factor.
- The results of this study (**Figure 4.5**) suggest that (*f*) is a weak function of H/D within the range of 0.5 < H/D < 1.1 for Re < 1000 (ie laminar

regime), with H/D having a greater impact above Re of 1000 (increasingly turbulent regime). The majority of previous studies have been restricted to the higher turbulent range. As such, little data is available in the literature in the low Re range.

- It has also been shown (**Figure 4.9**) that the Zukauskas correlations for cross flow over tube banks is adequate for predicting pressure drop for Re < 1000 for all H/D considered in this study. For Re > 1000, the Zukauskas model diverges from the data observed here with this divergence increasing with decreasing H/D.
- It was observed that that the standard Power law relationship which has typically been employed to empirically model flow and heat transfer effects in pin fin arrays, is insufficient to model the affects of clearance accurately (**Figure 4.5**).
- An empirical correlation based on a modified power law relationship that employs an exponential function of Cg/H has been proposed (**Figure 4.6**). This correlation was shown to produce a 2x improvement in accuracy compared to the standard power law form.

5.1.2 Heat Transfer Behavior

Mean heat transfer has been studied through the application of liquid crystal thermography. This approach enabled the calculation of thermal performance independent of conduction effects along the length of the pin fins. It also provided visual evidence of clearance related changes in heat transfer and fluid flow associated with the

array. Major findings on the effect of tip clearance on the heat transfer of pin fin arrays included the following:

- On a constant volumetric flow rate basis, heat transfer rates were observed to be greatest when no tip clearance is present (**Figures 4.10 – 4.11**). As a clearance gap is introduced, local velocity decreases and this more than negates any advantage gained by the exposure of additional heat transfer area at the tip.
- On a Re (i.e. constant local velocity) basis, increases in heat transfer are possible (**Figures 4.12-4.13**). Whether an increase or decrease occurs, and what the relative degree of the change will be, appears to be a complicated function of Re, Cg/D, H/D, assuming other array parameters are invariant.
- On a constant pumping power basis (**Figure 4.18**), the inclusion of tip clearance was found to be generally advantageous within the range of tip clearance considered, particularly in the laminar range. As Re increases the relative impact of clearance in most cases was seen to decrease, with some clearance gaps seen to produce a slightly lower heat transfer per pumping power than at the non-clearance case.
- Contrary to the results of Van Fossen (1984), results of this study (**Table 4.3**) suggested that heat transfer can be strongly influenced by pin aspect ratio of less than 1.0. While similar heat transfer rates were observed between H/D = 0.8 and 1.1 for the non-clearance case, a thirty percent reduction in heat transfer was observed when H/D was

reduced to 0.5 (Re = 5000). In the laminar region, no such decrease was observed.

- Liquid crystal imaging (**Figures 4.21 – 4.23**) provided visual evidence of basic changes in fluid flow about the pin tips which supports the numerically based predictions of **Rozati et al. (2008)**. It was observed that with the introduction of clearance, the pin tips experience transient fluctuations in flow patterns with presumed vortices washing across the outer edges of the pin tips, producing an elongated vertical temperature profile along the streamwise length of the tip. This is in contrast to a horizontal temperature field observed for the non-clearance case.

5.2 *Suggestions for Future Work*

The current study, by necessity, was limited in its scope in terms of investigating the numerous parameters that impact pin array performance and their relationship to the presence of tip clearance. While normalized pin height (H/D) and Re were varied, all other pin geometries were maintained essentially constant. As such, the results obtained here, while indicating the general potential of tip clearance, are none the less significantly limited in their applicability. To expand the understanding of tip clearance effects beyond the current work, it is recommended that the following areas be considered for further study:

- **Low Re regime**. Results show that clearance effects appear to be greatest at lower values of Re. While the current study did not consider Reynolds numbers below 200, there are a number of applications such as liquid cooled micro-arrays that likely would operate well below this limit and which could benefit from tip clearance effects.

- **Variations in S_T/D and S_L/D**. It has been well established that pin pitch impacts the overall performance of pin fin arrays. The pin pitches used in the current study were relatively compact compared to the majority of arrays studied in the literature over the past 30 years. As such, they represent one extreme of a wide range of pitches one would expect to be employed. It is therefore important to determine the relationship of tip clearance with performance in arrays in which the pins are not as tightly spaced to better generalize the role of clearance.

- **H/D dependency**. The work of Van Fossen (1982) asserted that while heat transfer is a function of pin aspect ratio down to H/D = 2.0, it becomes insensitive to aspect ratio in the range $0.5 < H/D < 2.0$. While the current study found little difference for H/D of 1.0 and 0.8, a significant decrease in heat transfer (approximately 30 percent) was experienced when H/D was reduced to 0.5. Therefore, it is believed that additional investigation into the impact of H/D is warranted, particularly in the range of 0.25 to 2.0.

- **Numerical modeling**. The experimental work of this study and those proposed for future consideration could benefit from a compliment of numerically based investigations. One such recent work by **Rozati et al. (2008)** produced a number of results that are consistent with those observed here and in doing so, provided some valuable insight into the possible reasons for the observed behavior.

5.3 *Concluding Remarks*

The role that tip clearance plays in the performance of a shrouded pin fin array is influenced by a complex combination of many parameters. Depending on the relative size of the clearance gap, the geometry of the array, and the material properties of the array, tip clearance can be beneficial or detrimental. It has been shown that tip clearance can result in elevated rates of heat transfer for a given array footprint. It can also result in higher heat transfer efficiency relative to the pumping power needed to sustain the forced convection. However, depending on the flow conditions and geometries, it can also produce higher pressure losses compared to a non-clearance scenario and promote lower overall heat transfer efficiencies. As such, more investigation is needed to better understand the limits and role of tip clearance in the overall performance of pin fin arrays.

Appendix A. Tabulation of Literature Review

A comprehensive list of 43 journal and conference papers, specifically dealing with the performance of shrouded pin fin arrays is tabulated here as follows:

- Table A1: Summary of pin fin array geometries and conditions considered in each study.
- Table A2: Summary of primary performance aspects considered in each study.
- Table A3: Summary of available empirical correlations and their range of applicability.

Table A1: Summary of Pin Fin Geometries and Conditions in Literature

Lead Author/ Yr.	Array Type	Pin Type	H/d	S_T/d	S_L/d	N_r	N_p	Fluid	PMT	Idealized BC	Re	Definition of Re	W (%)	Comments
Rozati/ 2008	S	C	0.6 – 1.0	2.1	1.1	NA	NA	Air	NA	Isoflux	10-400	$\frac{V_{max} d}{\upsilon}$	NA	Numerical Study
Hwang/ 2001	S	C,S,D	2.5 - 4.6	2.5	2.5	5	5	Air	LC	Transient/ Semi infinite solid	6,000 - 40,000	$\frac{UD_h}{\upsilon}$ ($D_h = 4Ac/P$)	Re, 6.4 Nu, 8.5 Eu, 7.7	Lateral flow effect, comparison between three different pin shapes
Tanda/2001	I,S	D	4.0	4-8	4-8	7-14	2-5	Air	LC	Isoflux	1800 - 6000	$\frac{V_{max} w}{\upsilon}$ (w = length of pin edge)	Re,3.2 *f*, 7.8 h, 6.5	Steady-state LC
Uzol/ 2001A	S	E	1.5	2.0	2.0	2	3	Air	LC	-	-	-	-	-
Hwang/ 1999A	I, S	C	1.3 - 3.6	2.5	2.5	5	5	Air	LC	Transient/ Semi infinite solid	7,000 - 53,000	$\frac{UD_h}{\upsilon}$ ($D_h = 4Ac/P$)	Re, 6.4 Nu, 8.6 K_L, 7.7	Transient technique, endwall htc, turning flow trapezoidal flow passage,
Hwang/ 1999B	I,S	C	1.3 - 3.6	2.5	2.5	5	5	Air	TC	Isoflux endwalls	6,000 - 40,000	$\frac{UD_h}{\upsilon}$ ($D_h = 4Ac/P$)	Re, 65 Nu, 8.4 K_L, 7.6	Effect of turning flow within a trapezoidal channel
Chyu/ 1999A	I, S	C	1	2.5	2.5	7	5	Air	NS	Isothermal pins and endwall	5,000 - 25,000	$\frac{V_{max} d}{\upsilon}$	Re, nr Nu, nr	Nu of pins shown to be 10% - 20% greater than that of endwall dependent on Re
Chyu/ 1999B	I, S	C	1	2.5	2.5	7	5	Air	NS	Isothermal pins, adiabatic endwall	5,000 - 30,000	$\frac{V_{max} d}{\upsilon}$	Re, 4.0 Sh, 7.0	Effect of flow entering perpendicular to array
Chyu/ 1999C	I	S	1	2.5	2.5	12	3	Air	LC	Transient/ Semi infinite solid	16000	$\frac{Ud}{\upsilon}$	Re, 5.0 Nu, 8.0	Effect of fin tip clearance
Chyu/ 1998	I, S	S,D,C	1	2.5	2.5	7	5	Air	NS	Isothermal pins, adiabatic endwall	9000 - 27000	$\frac{V_{max} L}{\upsilon}$ L=pin length	Re, nr Nu, 4.5 *f*, 6.0	Comparisons between square, circular, and diamond shaped pin fins.

Lead Author/ Yr.	Array Type	Pin Type	H/d	S_T/d	S_L/d	N_r	N_p	Fluid	PMT	Idealized BC	Re	Definition of Re	W (%)	Comments
Li/ 1998	S	E	1	1.1 - 3.0	1.1 - 3.0	10	nr	Air	NS	Isothermal pins and endwall	1000 - 9000	$\frac{V_{max} d}{\upsilon}$ d=equiv circumf dia	Re, nr Nu, nr Eu, nr	Elliptic pins outperformed round pins. Nu_{pin}/Nu_{ew} = f(Re) and > 1.0
Babus' Haq/ 1995	S	C	30	1.4 - 6.0	1.15-4.6	nr	nr	Air	TC	Isoflux endwall, adiabatic shroud	~ 1800	$\frac{Ud}{\upsilon}$	-	Study of optimum S_T and S_L pin pitch as a function of pin conductivity, very long pins
Minakami/ 1994	I	S	15.7	1.5 – 6	3 - 6	15	125, 250	Air	TC DI	Transient/ Semi infinite solid	20 - 120	$\frac{V_{max} d}{\upsilon}$	Re, nr Nu, nr *f*, nr	Effect of transverse pitch on Nu
Short/ 1994	S	T	1.9 - 7.5	1.8 - 3.2	2.0 - 6.4	8 - 22	24 - 39	Air	TC	Isoflux endwall, conductive shroud	175 - 4500	$\frac{V_{max} d}{\upsilon}$	Re, 2.0 *f*, 3.0 j, 32.0	Effect of S/d, T/d, L/d on Nu (j)- One active endwall
Jubran/ 1993	C	I, S	9.44	2.44 – 19.5	1.25 - 11.25	nr	nr	Air	TC	Quasi-Isothermal	5000 - 54000	$\frac{V_{max} d}{\upsilon}$	Re, 3.0 Nu, 5.0	Effect of pin spacing and tip clearance on average array heat transfer
Olsen/ 1992	A	T	0.34	1.35	1.17	87	nr	He	TC	Isoflux endwall, conductive shroud	450, 12,000	$\frac{UD_h}{\upsilon}$ ($D_h = 4Vo/A_w$)	Re, 10.7 Nu, 14-44 *f* , 23	Flow approaches at 12° angle relative to staggered arrangement
Al Dabagh/ 1992	S	C	0.7 - 2.2	2.0	1.5	9 - 13	4 - 6	Air	TC	Isothermal both endwalls	4000 - 48000	$\frac{V_{max} d}{\upsilon}$	Re, nr Nu, 10	pin and endwall contributions streamwise Nu development
Chyu/ 1991	I, S	C	1.0	2.4	2.08	5	7	Air	NS	Isothermal endwall, adiabatic pins	16000	$\frac{Ud}{\upsilon}$	Re, nr St, 4.0	Streamwise heat transfer development on endwall
Sparrow/ 1991	S	D	24	2.0	1.73	24	12	Air	-	-	200 - 2200	$\frac{V_{max} d}{\upsilon}$ d = pin width	Re, nr ξ, nr	Pressure drop measurements only
Chyu/ 1990	I, S	C	0.5 - 1.0	2.5	2.5	7	5	Air	NS	Isothermal pins, adiabatic endwall	5,000-30,000	$\frac{V_{max} d}{\upsilon}$	Re, nr Sh, 4.0 *f*, nr	Looked at effect of fillets at base of pins. (Nu ≈ 0.6Sh)
Lau/ 1989	S	C	1.0	2.5	2.5	6,8	6,4	Air		Isoflux both endwalls	6,000 - 60,000	$\frac{V_{max} d}{\upsilon}$	Nu, 6.5 Re, 5.0 *f*, 8.0	Effect of lateral flow ejection as occurs in turbine blades

Lead Author/ Yr.	Array Type	Pin Type	H/d	S_T/d	S_L/d	N_r	N_p	Fluid	PMT	Idealized BC	Re	Definition of Re	W (%)	Comments
Armstrong/ 1988	S	-	-	-	-	-	-	-	-	-	-		-	Review paper on staggered pin fin arrays for turbine blade cooling
Lau/ 1987	I, S	C	0.5 - 1.0	2.5	2.5	3 - 9	5,6	Air	NS	Isothermal endwall, adiabatic pins	33,000	$\frac{V_{max} d}{\upsilon}$	Re, nr Nu, 8.0	Endwall heat transfer, effect of L/D
Peng/ 1984	S	C	4,6	2,3,4	2,3,4	8 - 16	ns	Air	TC	Isothermal both endwalls	1,000 - 60,000	$\frac{V_{max} D_h}{\upsilon}$ ($D_h = 4A_{min}$)	Re, 3.0 j, 6.0 f, 6.5	Pins with end clearance extend from both endwalls.
Simoneau/ 1984	I, S	C	3.0	2.67	2.67	1 - 6	2,3	Air	TC	Isoflux (pin only)	5,000 - 125,000	$\frac{Ud}{\upsilon}$	Re, 5.0 Nu, 5.0 Tu, 10	Measurements of turbulence intensity with internally heated pin
Metzger/ 1984	I, S, A	C,O	1.0	2.5	1.5,2.5	10	ns	Air	TC	Isothermal both endwalls	5,000 - 50,000	$\frac{V_{max} d}{\upsilon}$	Re, nr Nu, 5.0 f, nr	Flow orientation shown to alter Nu by +10%
Brigham/ 1984	S	C	4.0	4.0	3.5	4,8	10	Air	TC	Isoflux both endwalls	300, 60,000	$\frac{UD_h}{\upsilon}$ ($D_h = 4A_cL/S$)	Re, 5.0 Nu, 5.0	Nu based on unique definition of characteristic length
VanFossen/ 1982	S	C	0.5 - 2	2 - 4	1.7-3.5	4	5	Air	TC	Isothermal both endwalls	300 - 30,000	$\frac{UD_h}{\upsilon}$ ($D_h = 4A_cL/S$)	Re, nr Nu, nr	Indicates Nu to be 35% higher along pins than on endwall
Metzger/ 1982A	S	C	1.0	2.5	1.0 - 5.0	10	10	Air	TC	Isothermal both endwalls	1,500 - 50,000	$\frac{V_{max} d}{\upsilon}$	Re,0.2 Nu, 5.0 *f*, nr	Indicates Nu to be within 10% on pin and endwall
Metzger/ 1982B	S	C	1.0	2.5	1.5, 2.5	10	4	Air	TC	Isothermal both endwalls	1,000 - 100,000	$\frac{V_{max} d}{\upsilon}$	Re, 0.2 Nu, 5.0 *f*, n.r.	Row resolved heat transfer development
Metzger/ 1982C	S	C	1.0	2.5	1.5, 2.5	10	5 - 10	Air	TC	Isothermal both endwalls	10^3 - 10^5	$\frac{V_{max} d}{\upsilon}$	Re, 0.2 Nu, 5.0	Row resolved heat transfer, Conducting vs. non conducting pins
Sparrow/ 1982A	I	C	4.0 - 12.0	2.2 - 4.1	2.2 - 4.1	6	6	Air	NS	Isothermal pins, adiabatic endwall	600- 5000			
Sparrow/ 1982B	I, S	C	3.0	3.0	2.6	18	n.s.	Air	NS	Isothermal endwall, adiabatic pins	1270 - 8900	$\frac{V_{max} d}{\upsilon}$	nr	0.14L tip clearance

Lead Author/ Yr.	Array Type	Pin Type	H/d	S_T/d	S_L/d	N_r	N_p	Fluid	PMT	Idealized BC	Re	Definition of Re	W (%)	Comments
Sparrow/ 1981	N.A.	C	7 - 19	NA	NA	NA	NA	Air	NS LB	Isothermal pins, adiabatic endwall	2,500 - 25,000	$\frac{Ud}{\upsilon}$	Re, nr Nu, nr	Nu from tip of cylinder with clearance 50% higher than pin sides
Sparrow/ 1980	I	C	1 - 3	3.0	2.6	18	5	Air	NS	Isothermal pins, adiabatic endwall	1000 - 9000	$\frac{V_{max}d}{\upsilon}$ Unique V_{max}	Re, nr *f*, nr	Effect of tip clearance on Heat transfer and Pressure drop, In-Line arrays
Sparrow/ 1978	S	C	1 - 3	3.0	2.6	18	5	Air	NS	Isothermal pins, adiabatic endwall	1000 - 9000	$\frac{V_{max}d}{\upsilon}$ Unique V_{max}	Re, nr Sh, nr *f*, nr	Effect of tip clearance on Heat transfer and Pressure drop Staggerd Arrays

Table A2: Primary Aspects Considered in Each Study

Lead Author/ Yr.	Array Orientation	H/D	St/d SL/d	Row Resolved Nu	Nu_{Ew} vs. Nu_{pin}	Pin Shape	Tip Clr.	BC's	Flow Entry	Channel Geometry/ effects	ΔP	Other
Rozati/2008		x					x				x	
Hwang/ 2001						x				x	x	
Tanda/2001	x			x							x	
Hwang/1999A	x									x		
Hwang/1999B	x									x		
Chyu/1999A	x			x	x			x?				
Chyu/1999B	x								x			
Chyu/1999C							x					
Chyu/1998	x			x		x					x	Nu/*f* comparisons
Li/1998					x	x					x	
Babus'Haq/1995			x								x	
Minakami/1994			x								x	
Short/1994		x	x					x			x	
Jubran/ 1993	x		x				x					
Olsen/1992	x										x	Array rotated 18 degrees from inline
Al Dabagh/1992		x		x	x							
Chyu/1991	x			x								Array has large tip clearance
Sparrow/1991						x					x	
Chyu/1990	x			x		x					x	Effect of endwall fillet
Armstrong/1988	x	x	x	x	x				x	x	x	Review Paper
Lau/1987										x	x	Lateral flow ejection
Peng/1984		x	x				x				x	
Simoneau/1984	x			x								Turbulence intensity is measured
Metzger/1984	x		x			x					x	
Brigham/1984		x										
Sparrow/ 1984												
VanFossen/1982		x			x							
Metzger/1982A		x	x		x						x	
Metzger/1982B			x	x							x	
Sparrow/1982A												
Sparrow/1982B	x											Effect of missing pin
Sparrow/1981							x					Nu from pin tip vs. circumferential area
Sparrow/1980	x	x		x			x				x	
Sparrow/1978		x		x			x				x	

Table A3: Summary of Shrouded Pin Fin Correlations Presented in the Literature

Lead Author	Yr.	Correlations	Thermal Boundary Conditions	Range	Comments
Hwang	2001	(1) $Nu_{ew} = 0.234\,\mathrm{Re}^{0.662}\left(1 - 0.3\varepsilon + 0.38\varepsilon^2\right)$ (2) $Nu_{ew} = 0.296\,\mathrm{Re}^{0.636}\left(1 - 0.28\varepsilon + 0.4\varepsilon^2\right)$ (3) $Nu_{ew} = 0.222\,\mathrm{Re}^{0.651}\left(1 - 0.22\varepsilon + 0.36\varepsilon^2\right)$	Semi-infinite solid w/ isothermal far boundary	6,000 < Re < 40,000 2.5 < H/D < 4.6 X/D = 2.5 S/D = 2.5	Effect of partial lateral ejection on endwall heat transfer - (1) Square pins; (2) Diamond shaped pins; (3) Circular pin - ε = ratio of lateral to total flow rate - Straight exit area to lateral exit area ratio was 2.5
Hwang	1999B	(1) $\overline{Nu} = 0.118\ \mathrm{Re}^{0.690}$ (2) $\overline{Nu} = 0.188\ \mathrm{Re}^{0.662}$ (3) $\overline{Nu} = 0.288\ \mathrm{Re}^{0.636}$ (4) $\overline{Nu} = 0.254\ \mathrm{Re}^{0.651}$	Isoflux endwalls	6,000 < Re < 40,000 1.3 < H/D < 3.6 X/D = 2.5 S/D = 2.5	Effect of turning flow in a trapezoidal channel - (1) Inline array, Straight flow - (2) Staggered array, Straight flow - (3) Inline array, 90° turn - (4) Staggered array, - 90° turn Straight exit area to lateral exit area ratio was 2.5
Hwang	1999A	(1) $Nu_{ew} = 0.117\ \mathrm{Re}^{0.691}$ (2) $Nu_{ew} = 0.187\ \mathrm{Re}^{0.666}$ (3) $Nu_{ew} = 0.288\ \mathrm{Re}^{0.631}$ (4) $Nu_{ew} = 0.254\ \mathrm{Re}^{0.650}$	Semi-infinite solid w/ isothermal far boundary	7,000 < Re < 53,000 1.3 < H/D < 3.6 X/D = 2.5 S/D = 2.5	Effect of turning flow in a trapezoidal channel - (1) Inline array, Straight flow - (2) Staggered array, Straight flow - (3) Inline array, 90° turn - (4) Staggered array, 90° turn - Straight exit area to lateral exit area ratio was 2.5
Chyu	1999A	(1) $Nu_p = 0.337\ \mathrm{Re}^{0.585}$ (2) $Nu_{ew} = 0.315\ \mathrm{Re}^{0.582}$ (3) $\overline{Nu} = 0.320\ \mathrm{Re}^{0.583}$ (4) $Nu_p = 0.115\ \mathrm{Re}^{0.658}$ (5) $Nu_{ew} = 0.052\ \mathrm{Re}^{0.759}$ (6) $\overline{Nu} = 0.320\ \mathrm{Re}^{0.733}$	Isothermal pins and endwalls	5000 < Re < 25000 H/D = 1.0 X/D = 2.5 S/D = 2.5	Comparisons between endwall and pin heat transfer - (1) Average Nu for pins alone, staggered array - (2) Average Nu for endwall alone, staggered array - (3) Array averaged Nu , staggered array - (4) Average Nu for pins alone, inline array - (5) Average Nu for endwall alone, inline array - (6) Array averaged Nu , inline array
Chyu	1998	(1) $Nu_p = 0.202\ \mathrm{Re}^{0.631}$ (2) $Nu_p = 0.162\ \mathrm{Re}^{0.639}$ (3) $Nu_p = 0.120\ \mathrm{Re}^{0.704}$ (4) $Nu_p = 0.073\ \mathrm{Re}^{0.732}$	Isothermal pins, adiabatic endwalls	9000 < Re < 27000 H/D = 1.0 X/D = 2.5 S/D = 2.5	Heat transfer from square and diamond shaped pins - (1) In-line Square pins - (2) In-line Diamond shaped pins - (3) Staggered square pins - (4) Staggered diamond shaped pins

Lead Author	Yr.	Correlations	Thermal Boundary Conditions	Range	Comments
Li	1998	$(1)\ Nu_p = 0.279\ \mathrm{Re}^{0.615}$ $(2)\ Nu_{ew} = 0.096\ \mathrm{Re}^{0.733}$ $(3)\ Nu_p = 0.322\ \mathrm{Re}^{0.545}$ $(4)\ Nu_{ew} = 0.099\ \mathrm{Re}^{0.676}$ $(5)\ \overline{Nu} = 0.462\ \mathrm{Re}^{0.530}$ $(6)\ \overline{Eu} = 1.96\ \mathrm{Re}^{-0.340}$	Isothermal pins and endwall	1000 < Re < 9000 H/D = 1.0 1.1 < X/D < 3.0 1.1 < S/D < 3.0	Heat transfer from elliptical pins. Endwall vs. pin comparisons - (1) X/D = S/D = 1.1 - (2) X/D = S/D = 1.1 - (3) X/D = S/D = 3.0 - (4) X/D = S/D = 3.0 - (5)* X/D = S/D = 2.5 - (6) X/D = S/D = 2.5 * data modified by Li et al. to model fin efficiency of steel pins
Li	1996	$Nu = 0.107\,\mathrm{Re}^{0.693}\left(\frac{a}{b}\right)^{0.28}$	N.A.	10^4 < Re < 10^5	German language paper on cam shaped pin fins.
Babus'Haq	1995	$\frac{S_{L,opt}}{d} = 1.59 + 0.0667\ e^{0.01k}$ $\frac{S_{T,opt}}{d} = 2.04$	IsoFlux endwall, adiabatic shroud	Re ~ 1800 H/D = 30.0 1.4 < X/D < 6.0 1.15 < S/D < 4.6	S_T/d held constant at 1. (relatively constant); S_L/d held constant at 2.3
Short	1994	$\overline{Nu} = 0.786\left(\frac{S}{d}\right)^{0.1}\left(\frac{T}{d}\right)^{0.2}\left(\frac{L}{d}\right)^{-0.20}\mathrm{Re}^{0.33}$ $f = 1.87\left(\frac{S}{d}\right)^{-1.4}\left(\frac{T}{d}\right)^{-0.61}\left(\frac{L}{d}\right)^{-0.11}\mathrm{Re}^{-0.31}$	IsoFlux endwall, adiabatic shroud	175 < Re < 4500 1.9 < H/D < 7.5 1.8 < X/D < 3.2 2.0 < S/D < 6.4	Data includes effect of fin efficiency. Pins were Al. modified from authors correlation for colburn j factor based on Nu = (j)(Re)($Pr^{0.33}$)

Lead Author	Yr.	Correlations	Thermal Boundary Conditions	Range	Comments
Jubran	1993	$(1)\ Nu = 0.45\,\mathrm{Re}^{0.71}\left(\frac{S_T}{w}\right)^{0.40}\left(\frac{S_L}{L}\right)^{0.51}$ $(2)\ Nu = 0.30\,\mathrm{Re}^{0.98}\left(\frac{S_T}{w}\right)^{0.35}\left(\frac{S_L}{L}\right)^{0.24}$ $(3)\ Nu = 0.36\,\mathrm{Re}^{0.56}\left(\frac{S_T}{w}\right)^{0.47}\left(\frac{S_L}{L}\right)^{0.13}$ $(4)\ Nu = 0.21\,\mathrm{Re}^{0.68}\left(\frac{S_T}{w}\right)^{0.06}\left(\frac{S_L}{L}\right)^{0.08}$ $(5)\ Nu = 0.58\,\mathrm{Re}^{0.51}\left(\frac{S_T}{w}\right)^{0.18}\left(\frac{S_L}{L}\right)^{0.21}$ $(6)\ Nu = 0.31\,\mathrm{Re}^{0.92}\left(\frac{S_T}{w}\right)^{0.20}\left(\frac{S_L}{L}\right)^{0.23}$	Isoflux endwall, adiabatic shroud	5,000 < Re < 54,000 H/D = 9.44 2.44 < X/D < 19.5 1.25 < S/D < 11.25	- (1) Inline, C/H =0 - (2) Staggered C/H = 0 - (3) Inline, C/H = 0.5 - (4) Staggered C/H = 0.5 - (5) Inline, C/H =1.0 - (6) Staggered C/H = 1.0
Olson	1992	$f = 0.8561\,\mathrm{Re}^{-0.216}$ $Nu_m = 0.0198\,\mathrm{Re}^{0.928}$ $Nu_w = 0.0357\,\mathrm{Re}^{0.837}$	Isoflux	450 < Re < 12,000 H/D = 0.34 X/D = 1.35 S/D = 1.17	Flow approaches at 12° angle relative to staggered arrangement
Chyu	1990	$(1)\ Nu = 0.33\ \mathrm{Re}^{0.55}$ $(2)\ Nu = 0.18\ \mathrm{Re}^{0.60}$	Isothermal pins, adiabatic wall	5,000 < Re < 30,000 H/D = 1.0 X/D = 2.5 S/D = 2.5	- (1) First row mass transfer of straight pin fins - (2) first row mass transfer from filleted pin fins

Lead Author	Yr.	Correlations	Thermal Boundary Conditions	Range	Comments
Metzger	1982B	(1) $Nu = 0.140\ \mathrm{Re}^{0.611}$ (2) $Nu = 0.022\ \mathrm{Re}^{0.813}$ (3) $Nu = 0.069\ \mathrm{Re}^{0.728}$ (4) $Nu = 0.092\ \mathrm{Re}^{0.707}$		1,000 < Re < 100,000 H/D = 1.0 S/D = 2.5	- (1) first row or array only, 1000 < Re < 10,000 - (2) first row of array only, 10,000 < Re < 100,000 - (3) Array average, 1000 < Re < 10,000, X/D = 2.5 - (4) Array average, 1000 < Re < 10,000, X/D = 1.5
Metzger	1982A	(1) $Nu = 0.092\ \mathrm{Re}^{0.707}$ (2) $Nu = 0.069\ \mathrm{Re}^{0.728}$ (3) $f = 0.317\ \mathrm{Re}^{-0.132}$ (4) $f = 1.76\ \mathrm{Re}^{-0.318}$		1,500 < Re < 50,000 H/D = 1.0 S/D = 1.05 to 5.0	- (1) X/D=1.5; S/D=2.5 - (2) X/D=2.5; S/D=2.5 - (3) 1000 < Re < 10,000 - (4) 10,000 < Re < 100,000
Metzger	1982C	(1) $Nu = 0.092\ \mathrm{Re}^{0.707}$ (2) $Nu = 0.069\ \mathrm{Re}^{0.728}$	Isothermal endwalls	1,500 < Re < 100,000 H/D = 1.0 S/D = 1.05 to 5.0	- (1) X/D=1.5; S/D=2.5 - (2) X/D=2.5; S/D=2.5 Same data as above reference

Legend Key to Tables A1 – A3:

Array Type: I - Inline S - Staggered A - Alternate arrangement somewhere between Inline and staggered	**Reported Results and related Uncertainties**: Re - Reynolds Number Nu - Nusselt Number *f* - Dimensionless friction factor Eu - Euler Number Sh - Sherwood Number j - colburn j-factor KL= 2DP/(G^2/rho)
Pin Shape: C - Right circular cylinder C' - Right circular cylinder (step changes in diameter along pin length) T - Tapered circular cylinder (diameter varies along pin length) O - Oblong E - Elliptical S - Square or rectangular D - Diamond shaped pins X – Other	**PMT - Primary measurement technigue:** LC - Thermochromic Liquid Crystals Temperature Measurements NS - Naphthalene Sublimation mass/(heat) transfer measurements TC - Thermocouples temperature measurements DI - Dye Injection flow visualization LB - Lamp Black flow visualization

This page intentionally left blank

Appendix B. Details of Uncertainty Analysis

B1 Estimated Uncertainty of Measured Quantities

General Approach:

A statistical approach was used to estimate uncertainties for reported variables involving large samples of measured data. As described by Coleman and Steele (1999), for a confidence level of 95 percent:

$$W_{95} = \left[B_i^2 + \left(2\sigma^2\right)\right]^{1/2}$$

Where:

B_i is the systemic uncertainty (bias error) of the measurement and (σ) is the standard deviation in the random error of the readings.

B1.1 Thermocouple Temperatures:

Uncertainties in thermocouple based temperature measurements were determined directly from an ice bath calibration, using a NIST traceable precision glass thermometer with 1/20 °C graduation as the reference. (16) readings were taken at a rate of one per second on each of (19) data channels for a total of (304) samples. Taking Bi = 0.05 °C (accuracy of standard), W_{95} was found to be 0.13°C.

B1.2 Liquid Crystal Temperatures:

In calibrating the liquid crystal Hue-vs.-Temperature behavior, Hue was calculated on a unit cell basis as described in Chapter 3. Each unit cell contained approximately 8500 pixels, with roughly 3500 samples per pin tip region and 2800 per endwall region (the remaining pixels being ignored). Since the image data is digital, Bi is taken to be zero, so the uncertainty is simply 2σ of the region data for a given test point.

B2 Estimated Uncertainty in Derived Quantities

General Approach:

The method used for estimating the propagation of uncertainty in values derived from experimental data was taken from Kline and McClintock (1953). The general form of the uncertainty calculation is as follows:

$$W_R = \sqrt{\left(\frac{\partial R}{\partial x_1} W_{x_1}\right)^2 + \left(\frac{\partial R}{\partial x_2} W_{x_2}\right)^2 + \ldots \left(\frac{\partial R}{\partial x_n} W_{s_n}\right)^2} \qquad \text{(B.1)}$$

where:	R:	Some derived parameter of interest such as h, Nu, etc.
	W_R:	Uncertainty in R (units of R)
	x_1, x_2, x_n:	Variables used in deriving R
	$W_{x_1}, W_{x_2}, W_{x_n}$	Uncertainty in variables used to derive R (units of x_n)
	W_R/R	Uncertainty in R (percent)

Added Uncertainty Associated With Curve Fitting:

Several quantities, including differential pressure, flow rate, and liquid crystal based temperature measurements are calculated from a least-square

curve fit polynomial of order (n). In these cases, there is an added amount of uncertainty introduced with the application of that polynomial, above and beyond that associated with the raw data

B2.1 Flow Rate:

Flow rate was measured using a series of variable are flow meters. These meters were calibrated by measuring the total volume of fluid passing through the meter in a given time period using a graduated flask and stopwatch. Uncertainties in this calibration process include the accuracy of the volume measurement and the accuracy in measuring the actual time period of water collection. During experimental trials, meter readings were very steady and care was taken to operate at flow directly corresponding to calibration points. Therefore the uncertainty involved in reading the flow meter level has been taken to be negligible and is not included below. Flow rates reported in this study are reported on a mass basis according to:

$$\dot{m} = \rho \dot{V} c \tag{B.2}$$

where :

$$c = \frac{1\,\text{min}}{60s} \cdot \frac{1m^2}{1000L}$$

$$\rho = 999.9 + 1.07 \cdot 10^{-1} T - 1.09 \cdot 10^{-2} T^2 + 9.61 \cdot 10^{-5} T^3 - 4.03 \cdot 10^{-7} T^4$$

$$W_{\dot{m}} = \sqrt{\left(\frac{\partial \dot{m}}{\partial \rho} W_\rho\right)^2 + \left(\frac{\partial \dot{m}}{\partial \dot{V}} W_{\dot{V}}\right)^2} \tag{B.3}$$

and:

$$\frac{\partial \dot{m}}{\partial \rho} = \frac{\dot{V}}{c} \tag{B.4}$$

$$\frac{\partial \dot{m}}{\partial \dot{V}} = \frac{\rho}{c} \tag{B.5}$$

$$W\rho = \sqrt{\left(\frac{\partial \rho}{\partial T} W_T\right)^2 + \left(W_{poly\_p}\right)^2} \tag{B.6}$$

$$\dot{V} = \frac{V}{t} \tag{B.7}$$

$$W_{\dot{V}} = \sqrt{\left(\frac{\partial \dot{V}}{\partial V} W_V\right)^2 + \left(\frac{\partial \dot{V}}{\partial t} W_t\right)^2} \tag{B.8}$$

$$\frac{\partial \dot{V}}{\partial V} = \frac{1}{t} \tag{B.9}$$

$$\frac{\partial \dot{V}}{\partial t} = -\frac{V}{t^2} \tag{B.10}$$

$$W_V = 0.005 \text{ Liters} \tag{B.11}$$

$$W_t = 0.5 \sec \tag{B.12}$$

B2.2 Differential Pressure:

Pressure drop was measured using a calibrated differential pressure transducer. The transducer was calibrated by exposing a vertical liquid column of water to one pressure port, while the other port was exposed to atmospheric pressure. Pressure drop during calibration of transducer defined as:

$$\Delta P = \rho g H_{wc} \tag{B.6}$$

(Assume no uncertainty associated with gravity constant)

$$W_{\Delta P} = \sqrt{\left(\frac{\partial \Delta P}{\partial H} W_{H_{wc}}\right)^2 + \left(\frac{\partial \Delta P}{\partial \rho} W_{\rho}\right)^2} \tag{B.7}$$

where:

$$\frac{\partial \Delta P}{\partial H} = \rho g \tag{B.8}$$

$$\frac{\partial \Delta P}{\partial \rho} = g H_{wc} \tag{B.9}$$

$$W_{H_{wc}} = 0.25\ in./3\ ft.\ of\ tubing$$

$$W_{\rho} = 0.5\ \text{kg/m}^3$$

Uncertainty in pin fin array pressure drop:

$$\Delta P_A = \Delta P_{bp} - \Delta P_{fp} \tag{B.10}$$

where:

$$W_{\Delta P_A} = \sqrt{\left(\frac{\partial \Delta P_A}{\partial \Delta P_{bp}} W_{bp}\right)^2 + \left(\frac{\partial \Delta P_A}{\partial \Delta P_{fp}} W_{fp}\right)^2} \tag{B.11}$$

$$\frac{\partial \Delta P_A}{\partial \Delta P_{bp}} = 1$$

$$\frac{\partial \Delta P_A}{\partial \Delta P_{fp}} = 1$$

$$W_{\Delta P_{bp}} = 0.02 \Delta P_{bp} \tag{B.12}$$

$$W_{\Delta P_{fp}} = 0.02 \Delta P_{fp} \tag{B.13}$$

B2.3 Differential Temperature:

This quantity is used to calculate the heat transfer coefficients of the array. Temperature differential and its associated uncertainty are expressed as:

$$\Delta T = T_{bp} - T_f \tag{B.14}$$

$$W_{\Delta T} = \sqrt{\left(\frac{\partial \Delta T}{\partial T_{bp}} W_{T_{bp}}\right)^2 + \left(\frac{\partial \Delta T}{\partial T_f} W_{T_f}\right)^2} = \sqrt{(0.165)^2 + (0.165)^2} = 0.233^{\circ} C \tag{B.15}$$

B2.4 Power Dissipation:

Uncertainties in calculated heater power are as follows:

$$Q_H = I_H V_H = \frac{V_R}{R_R} V_H \tag{B.16}$$

$$W_{Q_h} = \sqrt{\left(\frac{\partial Q_h}{\partial V_R} W_{V_R}\right)^2 + \left(\frac{\partial Q_h}{\partial R_R} W_{R_R}\right)^2 + \left(\frac{\partial Q_h}{\partial V_h} W_{V_h}\right)^2} = \sqrt{\left(\frac{V_h}{R_R} W_{V_R}\right)^2 + \left(-\frac{V_R V_h}{R_R^2} W_{R_R}\right)^2 + \left(\frac{V_R}{R_R} W_{V_h}\right)^2} \tag{B.17}$$

where:

$$W_{V_R} = \frac{0.01}{100} V_R + 1\ sig\ dig \tag{B.18}$$

$$W_{V_h} = \frac{0.01}{100} V_h + 1\ sig\ dig \tag{B.19}$$

$$W_{R_R} = 0.01\,\Omega$$

This formulation is applied to both the base plate trials and the heat loss calibration trials. Uncertainties in final array power levels are then:

$$Q_A = Q_H - Q_{L,cond} - Q_{L,conv} \tag{B.20}$$

where:

$$W_{Q_A} = \sqrt{\left(\frac{\partial Q_A}{\partial Q_H} W_{Q_H}\right)^2 + \left(\frac{\partial Q_A}{\partial Q_{L,cond}} W_{Q_{L,cond}}\right)^2 + \left(\frac{\partial Q_A}{\partial Q_{L,conv}} W_{Q_{L,conv}}\right)^2} \quad \text{(B.21)}$$

$$\frac{\partial Q_A}{\partial Q_H} = 1$$

$$\frac{\partial Q_A}{\partial Q_{L,cond}} = 1$$

$$\frac{\partial Q_A}{\partial Q_{L,conv}} = 1$$

B2.5 Reynolds Number:

$$\mathrm{Re} = \frac{V_{\max} D_{ave}}{\upsilon} \quad \text{(B.22)}$$

where:

$$V_{\max} = U \cdot c_g \quad \text{(B.23)}$$

$$c_g = \max\left\{\frac{S_T}{2(S_D - D_{ave})} \quad ; \quad \frac{S_T}{(S_T - D_{ave})}\right\} \quad \text{(B.24)}$$

$$U = \dot{V}\left(\frac{1\min}{60\sec}\right)\left(\frac{1m^3}{1000L}\right)\left(\frac{1}{A_c}\right) \quad \text{(B.25)}$$

$$\mathrm{Re} = \frac{U c_g D_{ave}}{\upsilon} \quad \text{(B.26)}$$

Assume negligible uncertainties associated with geometry variables.

Therefore:

$$W_{\mathrm{Re}} = \sqrt{\left(\frac{\partial \mathrm{Re}}{\partial U} W_U\right)^2 + \left(\frac{\partial \mathrm{Re}}{\partial \upsilon} W_\upsilon\right)^2} \tag{B.27}$$

where:

$$\frac{\partial \mathrm{Re}}{\partial U} = \frac{c_g D_{ave}}{\upsilon} \tag{B.28}$$

$$\frac{\partial \mathrm{Re}}{\partial \upsilon} = -\frac{U c_g D_{ave}}{\upsilon^2} \tag{B.29}$$

$$W_U = \sqrt{\left(\frac{\partial U}{\partial \dot{V}} W_{\dot{V}}\right)^2} \tag{B.30}$$

$$\frac{\partial U}{\partial \dot{V}} = \left(\frac{1\,\mathrm{min}}{60\,\mathrm{sec}}\right)\left(\frac{1 m^3}{1000 L}\right)\left(\frac{1}{A_c}\right) \tag{B.31}$$

$W_{\dot{V}}$: see equation. B.3

$$\upsilon = \frac{\mu}{\rho} \tag{B.32}$$

$$W_\upsilon = \sqrt{\left(\frac{\partial \upsilon}{\partial \rho} W_\rho\right)^2 + \left(\frac{\partial \upsilon}{\partial \mu} W\mu\right)^2} \tag{B.33}$$

$$\frac{\partial \upsilon}{\partial \rho} = -\frac{\mu}{\rho^2} \tag{B.34}$$

$$\frac{\partial \upsilon}{\partial \mu} = \frac{1}{\rho} \tag{B.35}$$

Fifth order polynomial curve fits to thermophysical properties from Incropera and Dewitt [1985] were used where:

$$\begin{aligned}\rho = {} & 999.9 + 1.07 \cdot 10^{-1} T - 1.09 \cdot 10^{-2} T^2 \\ & + 9.61 \cdot 10^{-5} T^3 - 4.03 \cdot 10^{-7} T^4\end{aligned} \tag{B.36}$$

$$\begin{aligned}\mu = {} & 1.74 \cdot 10^{-3} - 5.20 \cdot 10^{-5} T + 8.94 \cdot 10^{-7} T^2 \\ & - 8.06 \cdot 10^{-9} T^3 + 2.87 \cdot 10^{-11} T^4\end{aligned} \tag{B.37}$$

and:

$$W_\rho = \sqrt{\left(\frac{\partial \rho}{\partial T} W_T\right)^2} + W_{poly-\rho} \tag{B.38}$$

$$W_\mu = \sqrt{\left(\frac{\partial \mu}{\partial T} W_T\right)^2} + W_{poly-\mu} \tag{B.39}$$

$$\frac{\partial \rho}{\partial T} = 1.07 \cdot 10^{-1} - 2.17 \cdot 10^{-2} T + 2.88 \cdot 10^{-4} T^2 - 1.61 \cdot 10^{-6} T^3 \tag{B.40}$$

$$\frac{\partial \mu}{\partial T} = -5.2 \cdot 10^{-5} + 1.79 \cdot 10^{-6} T - 2.4 \cdot 10^{-8} T^2 + 1.15 \cdot 10^{-10} T^3 \tag{B.41}$$

$$W_{poly-\rho} = 0.38 kg / m^3$$

$$W_{poly-\mu} = 7.13 \cdot 10^{-6} \quad N \cdot s / m^2$$

B2.6 Nusselt Number:

$$Nu = \frac{h D_{ave}}{k_f} \tag{B.42}$$

Assume dimensional uncertainties are negligible.

$$W_{Nu} = \sqrt{\left(\frac{\partial Nu}{\partial h} W_h\right)^2 + \left(\frac{\partial Nu}{\partial k} W_k\right)^2} \tag{B.43}$$

$$\frac{\partial Nu}{\partial h} = \frac{D_{ave}}{k} \tag{B.44}$$

$$\frac{\partial Nu}{\partial k} = -\frac{h D_{ave}}{k_f^2} \tag{B.45}$$

A polynomial curve fit based on data of Incropera and Dewitt [1985] was used to estimate the thermal conductivity of water. It is of the form:

$$k_f = 5.7\cdot 10^{-1} + 1.77\cdot 10^{-3}T - 5.39\cdot 10^{-6}T^2 + 8.92\cdot 10^{-9}T^3 - 4.27\cdot 10^{-11}T^4 \quad \text{(B.46)}$$

where:

$$W_k = \sqrt{\left(\frac{\partial k}{\partial T}W_T\right)^2} + W_{poly-k} \quad \text{(B.47)}$$

$$\frac{\partial k}{\partial T} = 1.77\cdot 10^{-3} - 1.08\cdot 10^{-5}T + 2.70\cdot 10^{-8}T^2 - 1.85\cdot 10^{-10}T^3 \quad \text{(B.48)}$$

$$W_{poly-k} = 0.00075 \quad W/mk$$

$$h = \frac{Q_A}{A\Delta T} \quad \text{(B.49)}$$

where:

$$\Delta T = T_{bp} - T_f \quad \text{(B.50)}$$

$$W_h = \sqrt{\left(\frac{\partial h}{\partial Q_A}W_{Q_A}\right)^2 + \left(\frac{\partial h}{\partial \Delta T}W_{\Delta T}\right)^2} \quad \text{(B.51)}$$

$$\frac{\partial h}{\partial Q_A} = \frac{1}{A\Delta T} \quad \text{(B.52)}$$

$$\frac{\partial h}{\partial \Delta T} = -\frac{Q_A}{A(\Delta T)^2} \quad \text{(B.53)}$$

W_{Q_A} : see equation B.22

$W_{\Delta T}$: see equation B.16

B2.7 Friction Factor:

$$f = \frac{\Delta P_A}{2\rho V_{\max}^2 N} \tag{B.54}$$

$V_{\max}$: see equation B.24 (B.55)

c_g : see equation B.25 (B.56)

therefore:

$$f = \frac{\Delta P_A}{2\rho U^2 c_g^2 N} \tag{B.57}$$

$$W_f = \sqrt{\left(\frac{\partial f}{\partial \Delta P_A} W_{\Delta P_A}\right)^2 + \left(\frac{\partial f}{\partial U} W_U\right)^2 + \left(\frac{\partial f}{\partial \rho} W_\rho\right)^2} \tag{B.58}$$

where:

$$\frac{\partial f}{\partial \Delta P_A} = \frac{1}{2\rho U^2 c_g^2 N} \tag{B.59}$$

$$\frac{\partial f}{\partial U} = -\frac{\Delta P_A}{\rho U^3 c_g N} \tag{B.60}$$

$$\frac{\partial f}{\partial \rho} = -\frac{\Delta P_A}{2\rho^2 U^2 c_g^2 N} \tag{B.61}$$

$W_{\Delta P_A}$: see equation B.11

W_U : see equation B.31

$W_\rho = 0.5\,\mathrm{kg/m^3}$

$$U = \dot{V}\left(\frac{1\,\mathrm{min}}{60\,\mathrm{sec}}\right)\left(\frac{1m^3}{1000L}\right)\left(\frac{1}{A_c}\right) \tag{B.62}$$

Appendix C: Photographs and Illustrations

This section includes additional photographs of the testing apparatus and detailed drawings used to manufacture the various components of the test assembly.

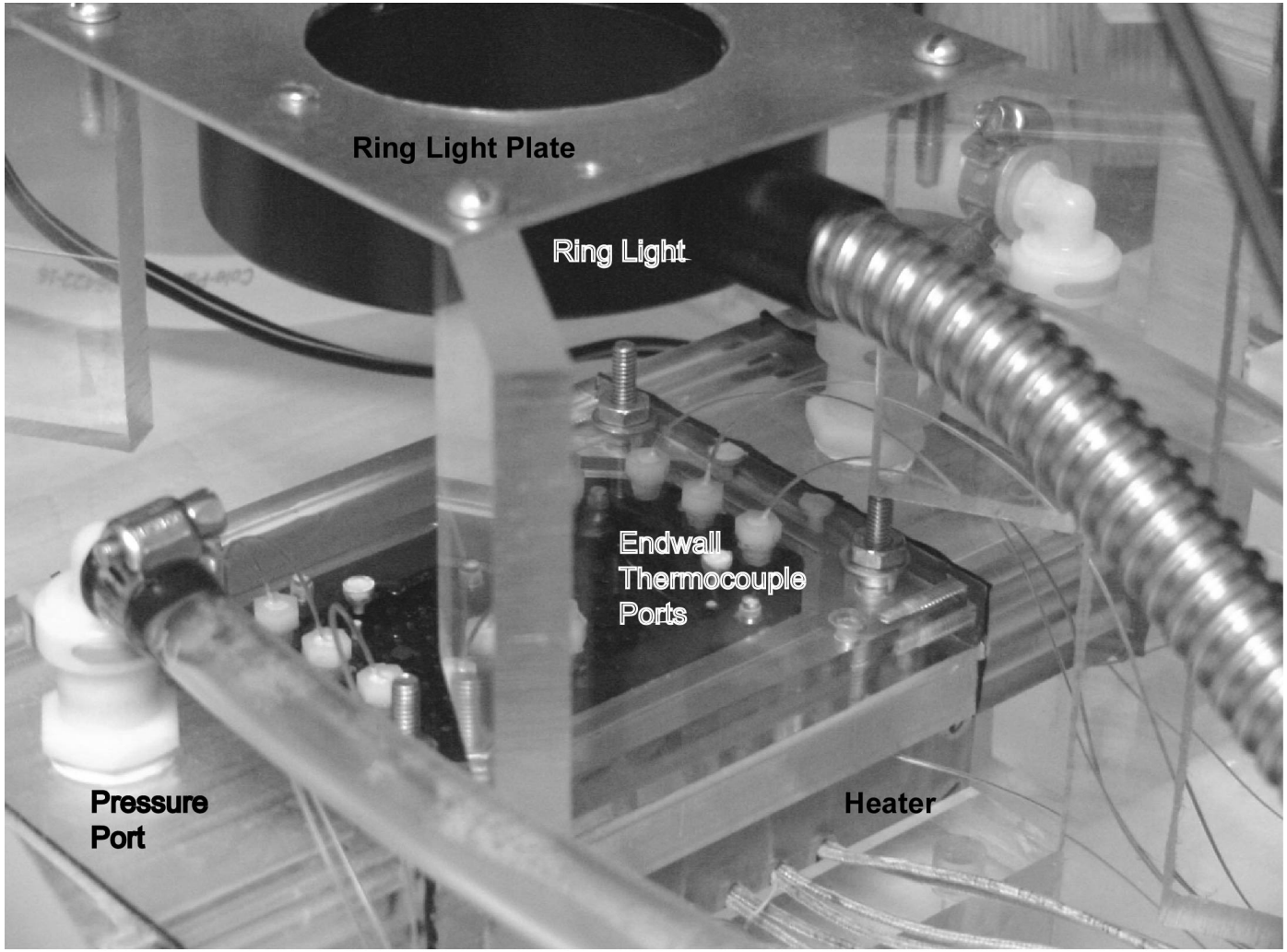

Figure C.1: Photograph of test assembly and liquid crystal viewing set-up

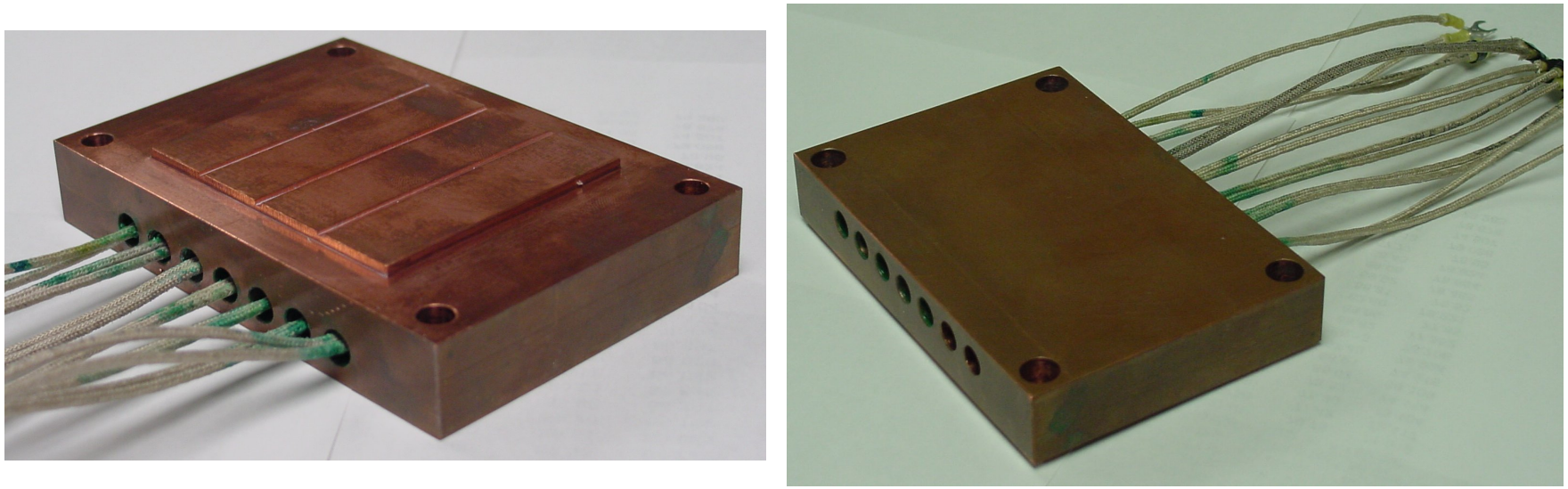

Figure C.2: Photo of copper heater, top and bottom sides. The three vertical lines on the face of the block are 1/16” wide by 1/16” deep channels. Thermocouples were embedded into the channels using thermally conductive epoxy.

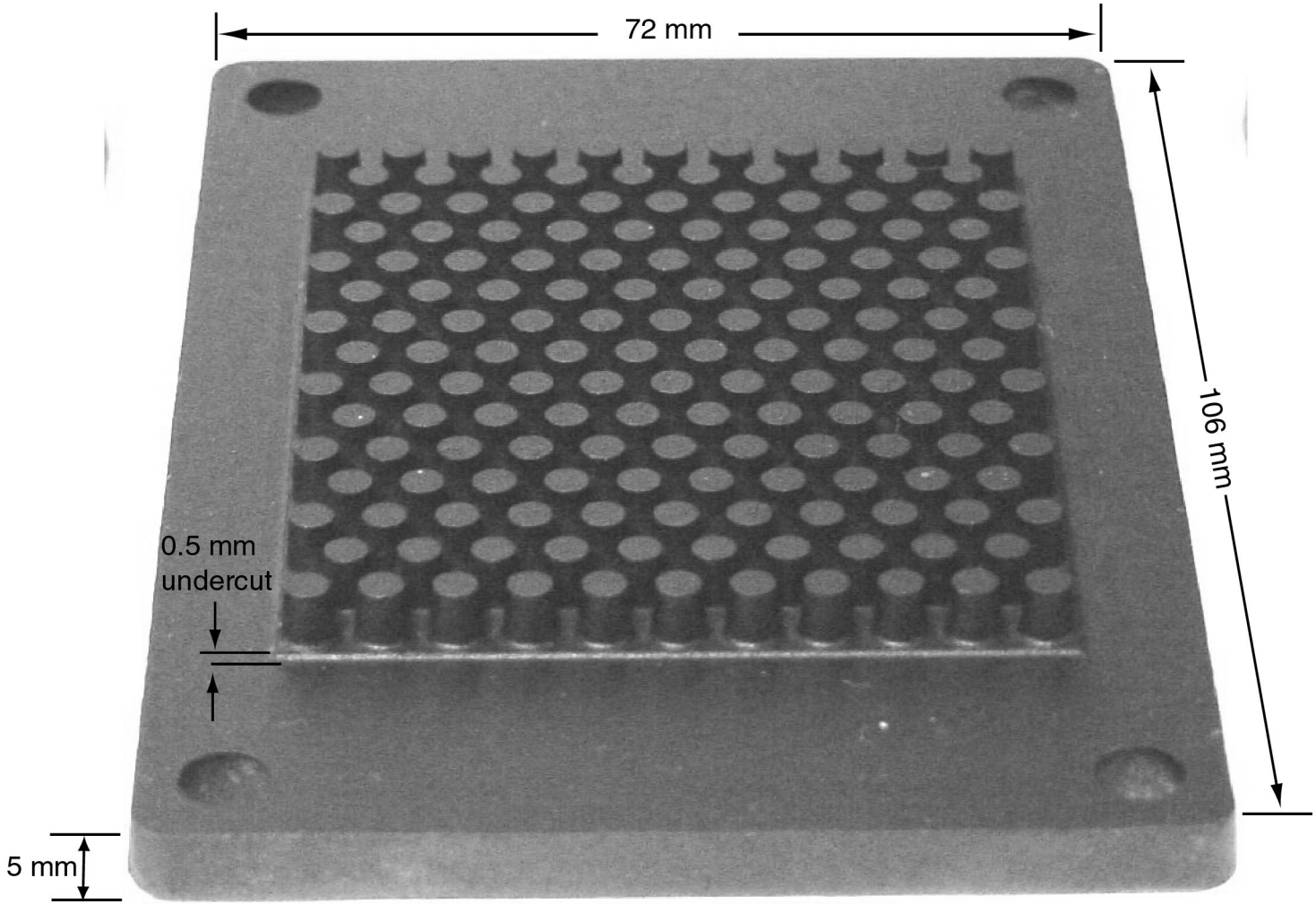

Figure C.3: Photograph of 4mm height pin fin base plate, coated with black backing paint and liquid crystals

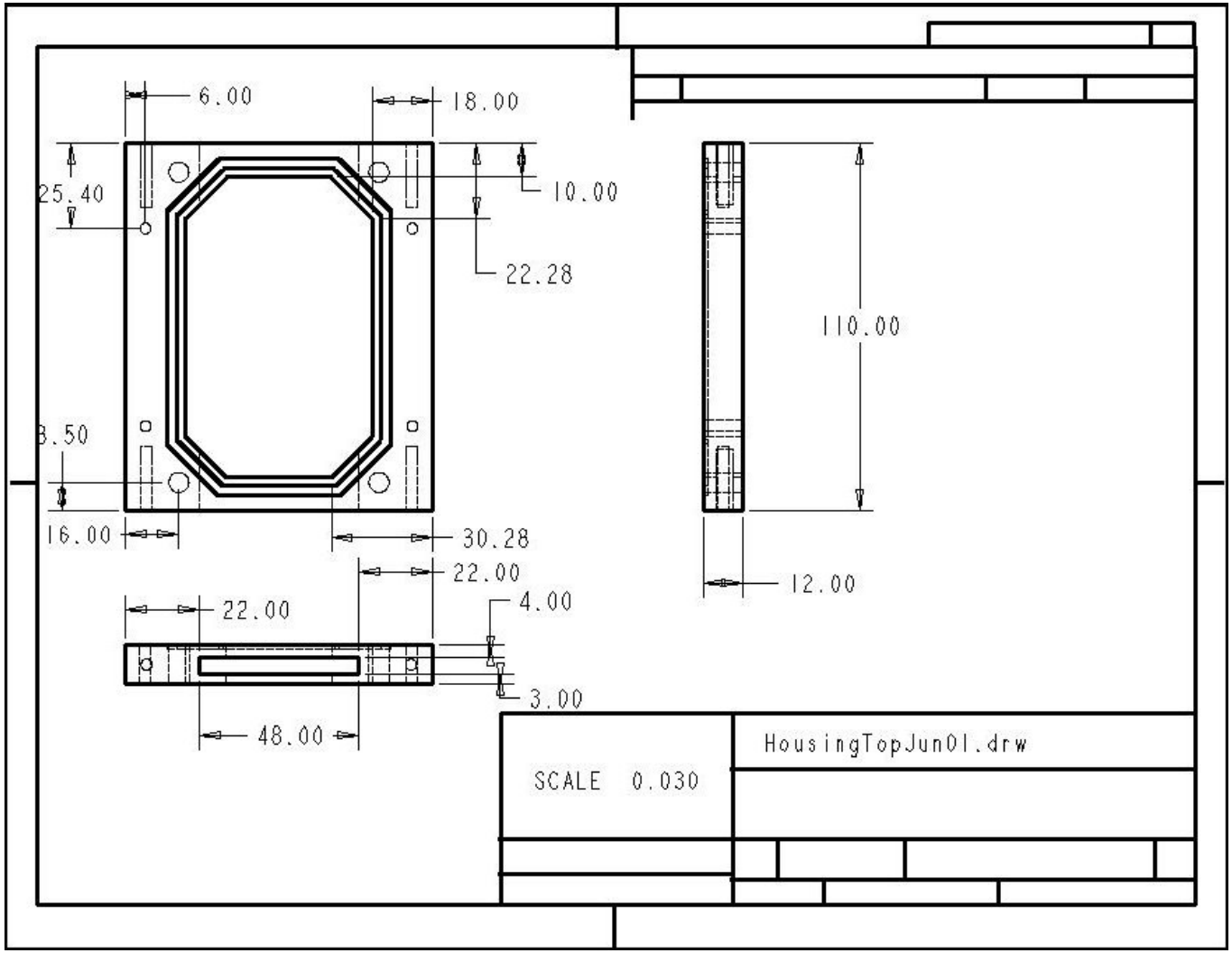

Figure C.4: Aluminum housing section of test assembly

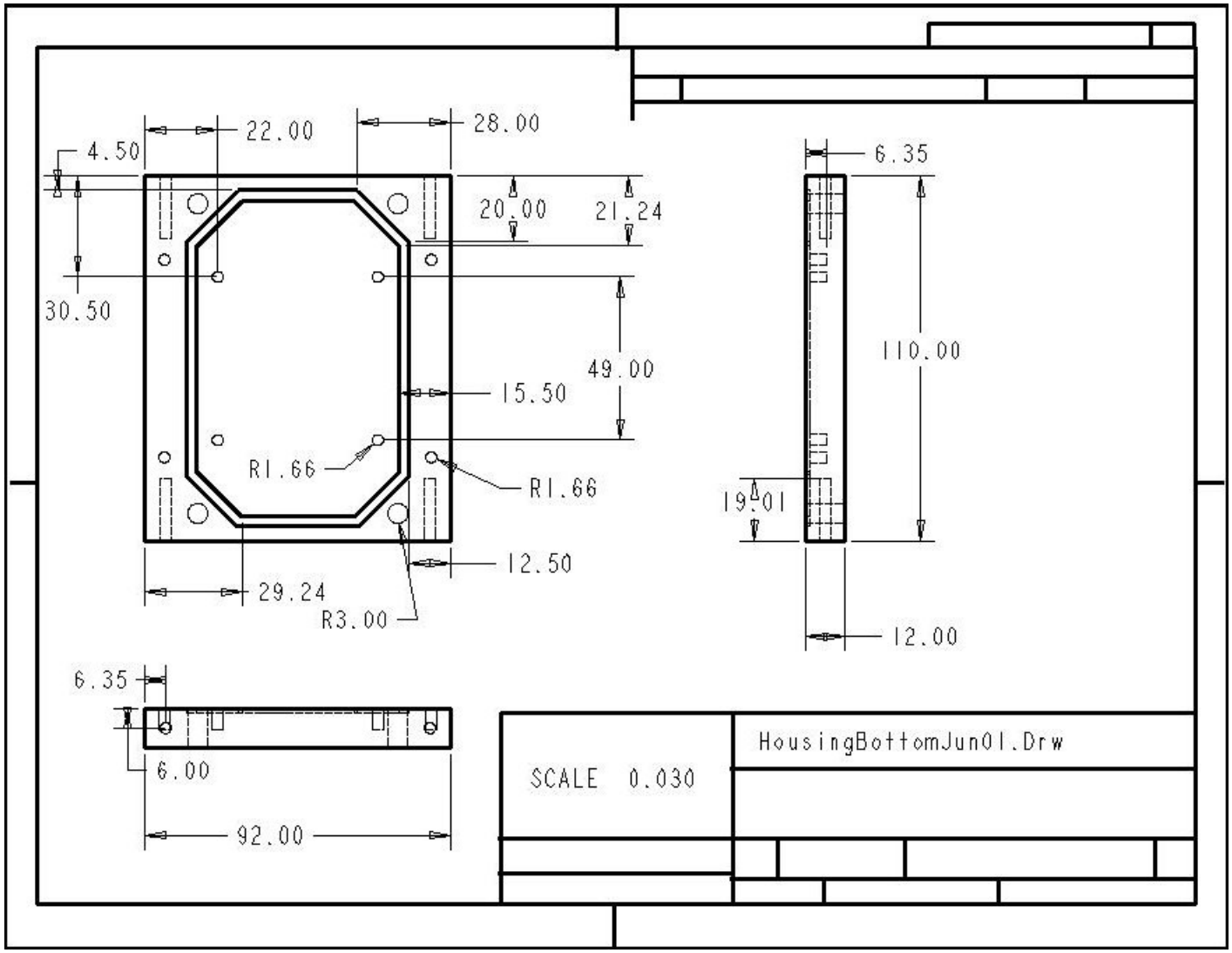

Figure C.5: Plexiglas housing section of test assembly

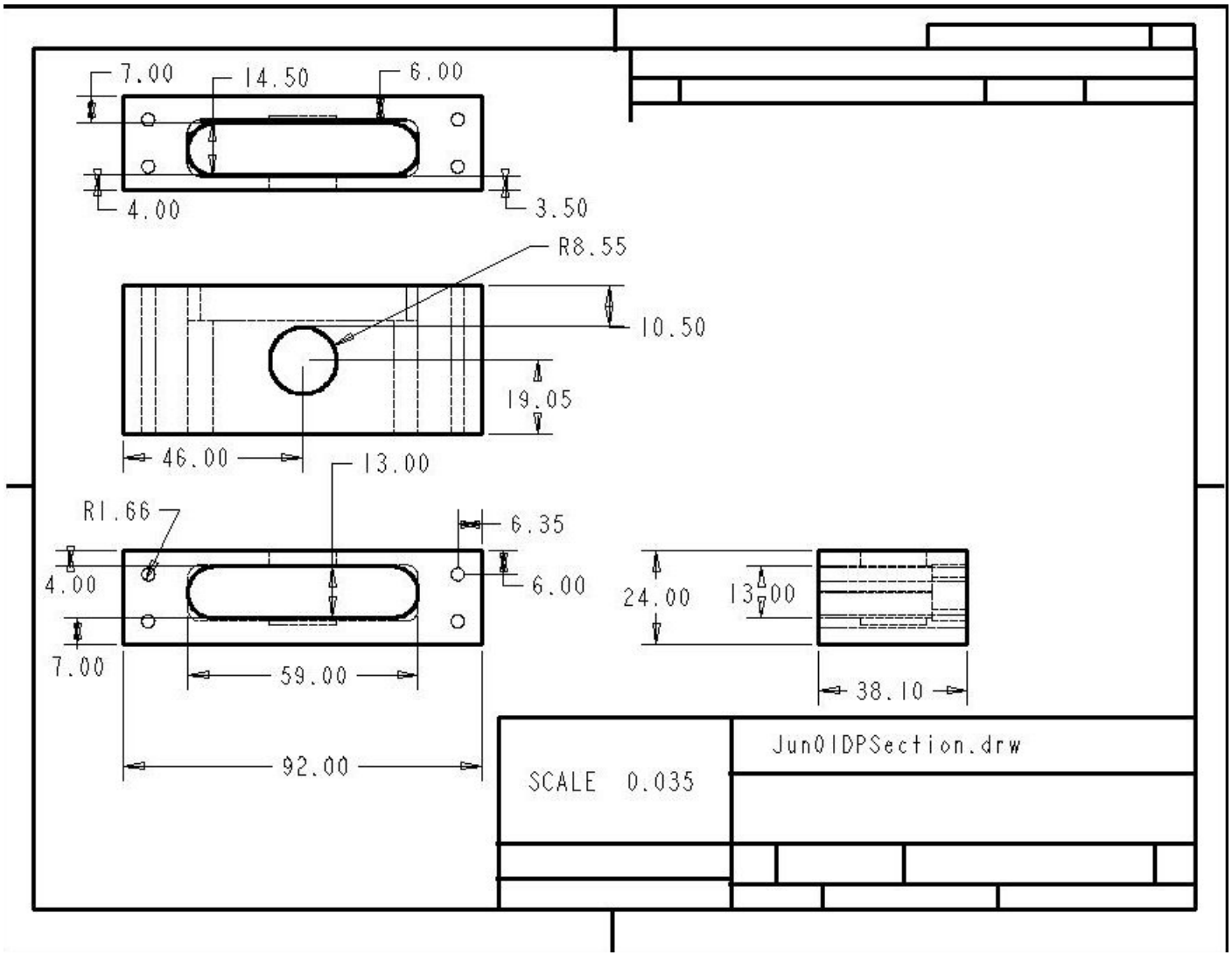

Figure C.6: Plexiglas pressure port section of test assembly

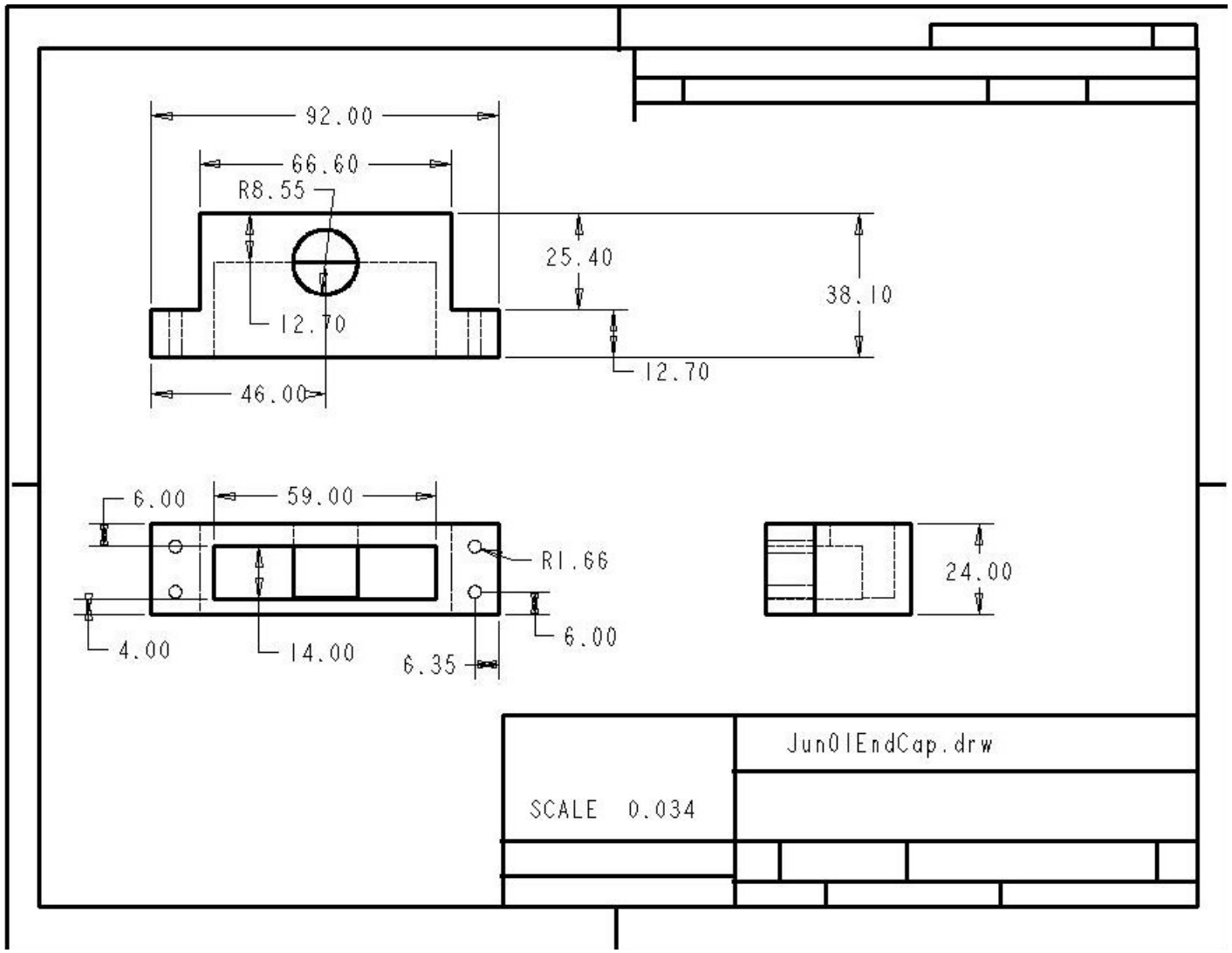

Figure C.7: Plexiglas endsection (inlet/outlet) of test assembly

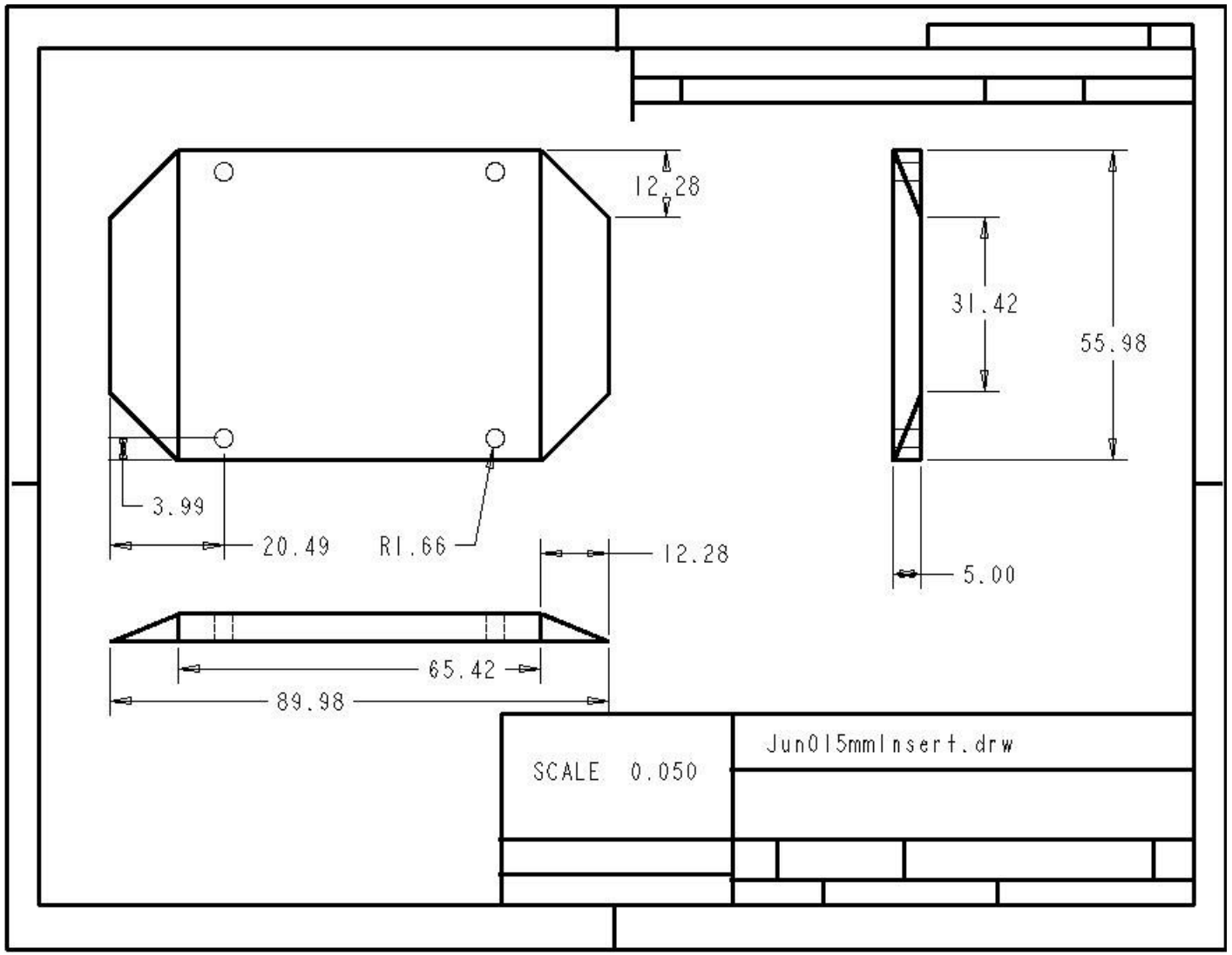

Figure C.8: Plexiglas insert 5 mm - (similar 3 mm and 4 mm thick inserts also used in testing)

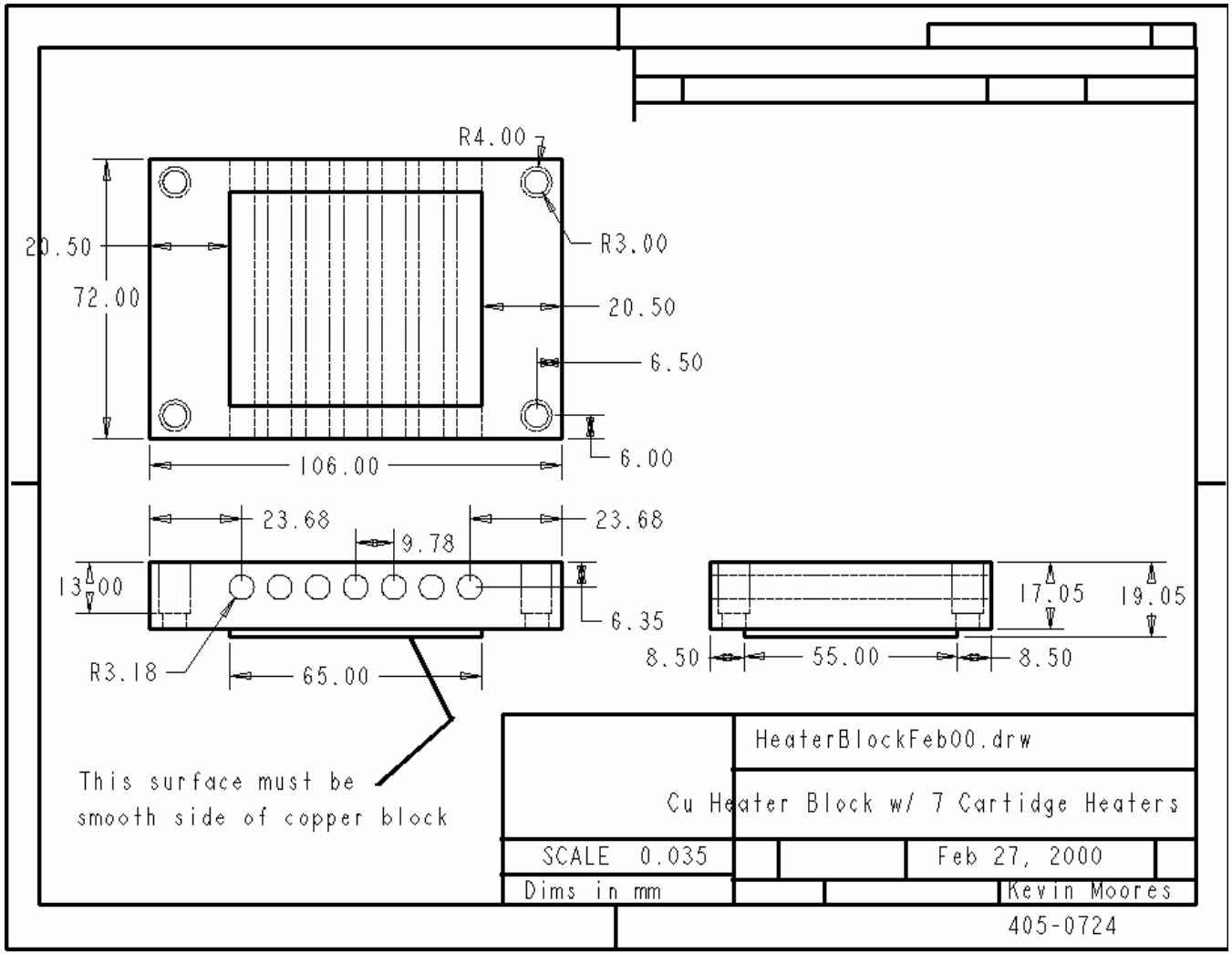

Figure C.9: Copper heater block

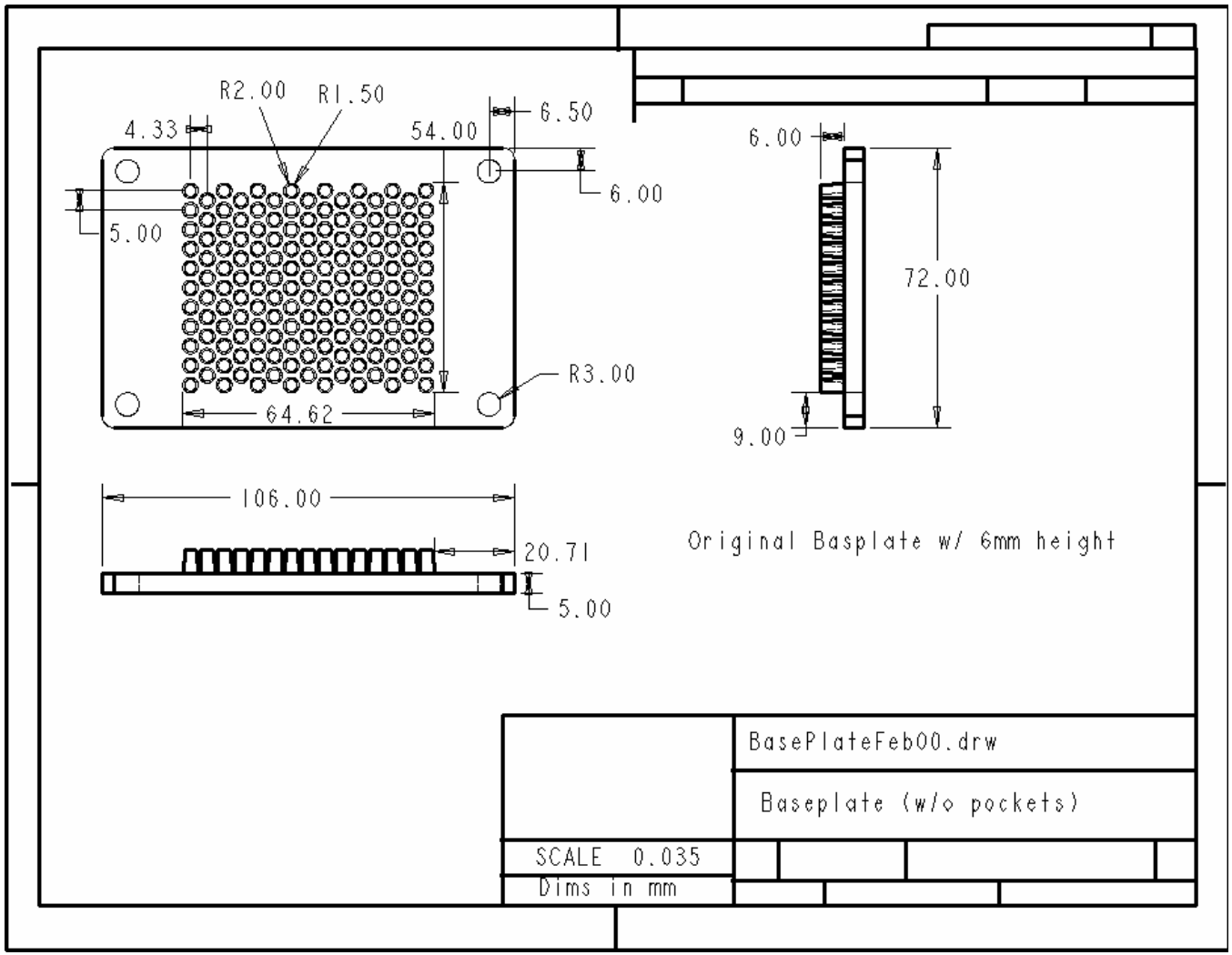

Figure C.10: AlSiC baseplate with 6mm pin fin height.

This page intentionally left blank

References

Akino, N., Kunugi, T., Ichimiya, K., Mitsushiro, K., Ueda, M., 1989, “Improved liquid crystal thermometry excluding human color sensation”, J. Heat Transfer, Vol. 111, pp. 558-565.

Al Dabagh, A.M., Andrews, G.E., 1992, "Pin fin heat transfer: contributions of the wall and the pin to the overall heat transfer", ASME paper 92-GT-242.

Armstrong, J., Winstanley, D., 1988, “A Review of staggered array pin fin heat transfer for turbine cooling applications”, Trans. ASME, J. Turbomachinery, Vol. 110, pp. 94-103.

Arora, S.C., Abdel Messeh, W., 1983, "Heat transfer experiments in high aspect ratio rectangular channel with epoxied short pin fins", ASME Paper No. 83-GT-57.

Arora, S.C., Abdel Messeh, W., 1985, "Pressure drop and heat transfer characteristics of circular and oblong low aspect ratio pin fins", NATO AGARD-CP-390, Heat Transfer and cooling in gas turbines, Propulsion and Energetics Panel 65th Symposium, Bergen, Norway, May 6-10.

Azar, K., Benson, J.R., Manno, V.P., 1991, “Liquid crystal imaging for temperature measurement of electronic devices”, Proc. Seventh Annual SEMI-THERM Symposium, pp. 23-33.

Babus'Haq, R.F., Akintunde, K., Probert, S.D., 1995, "Thermal performance of a pin fin assembly", Int. J. Heat and Fluid Flow, Vol. 16, pp. 50 – 55.

Baughn, J.W., 1995, “Liquid crystal methods for studying turbulent heat transfer”, Int. J. Heat and Fluid Flow, Vol. 16, pp. 365-375.

Baughn, J.W., Anderson, M.R., Mayhew, J.E., Wolf, J.D., 1999, “Hysteresis of thermochromic liquid crystals temperature measurement based on hue”, J. Heat Transfer, Vol. 121, pp. 1067-1074.

Baughn, J.W., Elderkin, M.J., McKillop, A.A., 1986, “Heat transfer from a single cylinder, cylinders in tandem, and cylinders in the entrance region of a tube back with a uniform heat flux”, Trans. ASME J. Heat Transfer, Vol. 108, pp.386-391.

Baughn, J.W., Hoffman, M.A., Makel, D.B., 1986, “Improvements in a new technique for measuring and mapping heat transfer coefficients”, Rev. Sci. Instrumentation, Vol. 57, No. 4, pp. 650-654.

Baughn, J.W., Ireland, P.T., Jones, T.V., Saniei, 1989, “A comparison of the transient and heated-coating methods for the measurement of local heat transfer coefficients on a pin fin”, J. Heat Transfer, Vol. 111, pp. 877-881.

Baughn, J.W., Mayhew, J.E., Anderson, M.R., Butler, R.J., 1998, “A periodic transient method using liquid crystals for the measurement of local heat transfer coefficients”, J. Heat Transfer, Vol. 120, pp. 772-777.

Bergelin, O.P., Brown, G.A., Doberstein, S.C., 1952, “Heat transfer and fluid friction during flow across banks of tubes – IV: A study of the transition zone between viscous and turbulent flow”, Transactions of the ASME, Vol. 74, pp. 953-960.

Brigham, B.A., Van Fossen, G.J., 1984, “Length of diameter ration and row number effects in short pin fin heat transfer”, Trans. ASME J. Engineering for Gas Turbines and Power, Vol., 106, pp. 241-245.

Brunschwiler, T., Michel, B., Rothuizen, H., Kloter, U., Wunderle, B., Oppermann, H., Reichl, H., "Forced convective interlayer cooling in vertically integrated packages," Proc. 11th Intersociety Conference on Thermal Management, ITHERM May 28-31, Orlando FL (2008).

Butler, R.J., Baughn, J.W., 1996, “The effect of the thermal boundary condition on transient method heat transfer measurements on a flat plate with a laminar boundary layer”, J. Heat Transfer, Vol. 118, pp. 831-837.

Camci, C., Kim, K., Hippensteele, S.A., Poinsatte, P.E., 1993, “Evaluation of a hue capturing based transient liquid crystal method for high resolution mapping of convection heat transfer on curved surfaces”, J. Heat Transfer, Vol. 115, pp. 311-318.

Chyu, M.K., 1990, “Heat transfer and pressure drop for short pin-fin arrays with pin endwall fillet”, Trans. ASME, J. Heat Transfer, Vol. 112, pp. 926-932.

Chyu, M.K., Goldstein, R.J., 1991, “Influence of an array of wall-mounted cylinders on the mass transfer from a flat surface”, In., J. Heat Mass Transfer, Vol., 34, No. 9, pp. 2175-2186.

Chyu, M.K., Hsing, Y.C., Natarajan, V., 1998, "Convective heat transfer of cubic fin arrays in a narrow channel", Trans. ASME, J. Turbomachinery, Vol. 120, pp. 362 – 367.

Chyu, M.K., Hsing, Y., Natarajan, V., Chiou, J.S., 1999(B), "Effects of perpendicular flow entry on convective heat/mass transfer from pin-fin arrays", Trans., ASME, Journal of Heat Transfer, Vol. 121, pp. 668-674.

Chyu, M.K., Hsing, Y., Shih, T.I.P., 1999(A), "Heat transfer contributions of pins and endwall in pin fin arrays: effects of thermal boundary condition modeling", Trans., ASME, J. Turbomachinery, Vol. 121, pp. 257-263.

Chyu, M.K., Yen, C.H., Ma. W., Shih, T.I.P., 1999(C), "Effects of flow gap atop pin elements on the heat transfer from pin fin arrays", ASME Paper 99-GT-47.

Critoph, R.E., Holland, M.K., Fisher, M., 1999, "Comparison of steady state and transient methods for measurement of local heat transfer in plate fin-tube heat exchangers using liquid crystal thermography with radiant heating", Int. J. Heat and Mass Transfer, Vol. 42, pp. 1-12.

Coleman, W.H., Steele, W.G, 1995, Experimentation and Uncertainty Analysis for Engineers, 2nd Edition, John Wiley and Sons, New York.

Ekkad, S.V., Han, J., 2000, "A transient liquid crystal thermography technique for gas turbine heat transfer measurements", Measurement Science Technology, Vol. 11, pp. 957-968.

Fairfield, J.G., Soling, S.P., Patterson, S.P., 1938, "Heat transfer and flow resistance in cross flow of gases over tube banks", Trans. ASME. Vol., 60, pp. 381-392.

Farina, D.J., Hacker, J.M., Moffat, R.J., Eaton, J.K., 1993, "Illuminant invariant calibration of thermochromic liquid crystals", HTD-Vol. 252, Visualization of Heat Transfer Processes, pp. 1-11.

Goldstein, R.J., Jabbari, M.Y., Chen, S.B., 1994, "Convective mass transfer and pressure loss characteristics of staggered short pin-fin arrays", Int. J. Heat Mass Transfer, Vol. 37, Supplement 1, pp. 149-160.

Grimison, E.D., 1937, "Correlation and utilization of new data on flow resistance and heat transfer for cross flow of gases over tube banks", Trans. ASME, Vol. 59, pp. 583-594.

Hay, J.L., Hollingsworth, D.K., 1996, "A comparison of trichromic systems for use in calibration of polymer-dispersed thermochromic liquid crystals", Experimental Thermal and Fluid Science, Vol. 12, pp. 1-12.

Hay, J.L., Hollingsworth, D.K., 1998, "Calibration of micro-encapsulated liquid crystals using hue angle and a dimensionless temperature", Experimental Thermal and Fluid Science, Vol. 18, pp. 251-257.

Hippensteele, S.A., Poinsatte, P.E., 1993, "Transient liquid crystal technique used to produce high resolution convective heat transfer coefficients maps", HTD-Vol. 252, Visualization of Heat Transfer Procedures, pp. 13-21.

Hollingsworth, D.K., Boehman, A.L., Smith, E.G., Moffat, R.J., 1989, “Measurement of temperature and heat transfer coefficient distributions in a complex flow using liquid crystal thermography and true-color image processing”, ASME Collected Papers in Heat Transfer, pp. 35-42.

Huge, E.C., 1937, “Experimental investigation of effects of equipment size on convection heat transfer and flow resistance in cross flow of gases over tube banks”, Vol. 59, pp. 573-581.

Hwang, J.J., Lai, D.Y., Tsia, Y.P., 1999(B) "Heat transfer and pressure drop in pin fin trapezoidal ducts", Trans. ASME, J. Turbomachinery, Vol. 121, pp. 264 – 271.

Hwang, J.J., Lui., C.C., 1999(A), "Detailed heat transfer characteristic comparisons in straight and 90-deg turned trapezoidal ducts with pin fin arrays", Int. J. Heat and Mass Transfer, Vol. 42, pp. 4005 – 4016.

Hwang, J.J., Lui, C.C., 2001, "Lateral flow effects on endwall heat transfer and pressure drop in a pin-fin trapezoidal duct of various pin shapes", Trans. ASME, J. Turbomachinery, Vol. 123, pp. 133 – 139.

Incropera, F.P., Dewitt, D.P., 1985, *Fundamentals of Heat and Mass Transfer*, 2nd Edition, John Wiley & Sons, N.Y.

Ireland, P.T., Jones, T.V., 2000, “Liquid crystal measurements of heat transfer and surface shear stress”, Measurement Science and Technology, Vol. 11, No. 7, pp. 969-986.

Ireland, P.T., Neely, A.J., Gillespie, R.H., Robertson, A.J., 1999, “Turbulent heat transfer measurements using liquid crystals”, Int. J. Heat and Fluid Flow, Vol. 20, pp. 355-367.

Jubran, B.A., Hamdan, M.A., Abjualh, R.M., 1993, “Enhanced heat transfer, missing pin, and optimization for cylindrical pin fin arrays”, Trans. ASME, J. Heat Transfer, Vol. 115, pp. 576-583.

Kumaran, T.K., Han, J.C., Lau, S.C., 1991, "Augmented heat transfer in a pin fin channel with short or long ejection holes", Int. J. Heat Mass Transfer, vol. 34, No. 10, pp. 2617-2628.

Lau, S.C., Han, J.C., Batten, T., 1989, "Heat transfer, pressure drop and mass flow rate in pin fin channels with long and short trailing edge ejection holes", Trans. ASME, J. Turbomachinery, Vol. 111, pp. 116-123.

Lau, S.C., Han, J.C., Kim, Y.S., 1989, “Turbulent heat transfer and friction in pin fin channels with lateral flow ejection”, Trans. ASME, J. Heat Transfer, Vol. 111, pp. 51-58.

Lau, S.C., Kim, Y.S., Han, J.C., 1987, “Local endwall heat/mass transfer distributions in pin fin channels”, J. Thermophysics and Heat Transfer, Vol. 1, No. 4, pp. 365-372.

Li, Q., Chen, Z., Flechtner, U., Warnecke, H.J., 1996, "Konvective warme/stoff-ubertragung und druckverlust in rohrbundeln bestehend aus tropfenformigen rohren", Chemie Ingenieur Technik, Vol. 68, pp. 1299 – 1302 (In German).

Li. Q., Chen, Z., Flechtner, U., Warnecke, H.J., 1998, "Heat transfer and pressure-drop characteristics in rectangular channels with elliptic pin fins", Int. J. Heat and Fluid Flow, Vol. 19, pp.245-250.

Matsumoto, R., Kikkawa, S., 1997, “Effect of pin fin arrangement on endwall heat transfer”, JSME International Journal, Vol. 40, No. 1, pp. 142-151.

McMillin, R.D., S.C. Lau, 1992, "Effect Of trailing-edge ejection on local heat (mass) transfer in pin fin cooling channels in turbine blades", ASME Paper No. 92-GT-178.

Metzger, D.E., Berry, R.A., Bronson, J.P., 1982(B), “Developing heat transfer in rectangular ducts with staggered arrays of short pin fins”, Trans. ASME, J. Heat Transfer, Vol. 104, pp. 700-706.

Metzger, D.E., Fan, C.S., Haley, S.W., 1984, “Effects of pin shape and array orientation on heat transfer and pressure loss in pin fin arrays”, Trans. ASME J. Heat Transfer, Vol. 106, pp. 252-257.

Metzger, D.E., Fan. Z.X, Shephard, W.B., 1982(A), “Pressure loss and heat transfer through multiple rows of short pin fins”, ASME Paper No. 82-IHTC-31.

Metzger, D.E., Haley, S.W., 1982(C), “Heat transfer experiments and flow visualization for arrays of short pin fins", ASME Paper No. 82-GT-138.

Metzger, D.E., Shephard, W.B., Haley, S.W., 1986, "Row resolved heat transfer variations in pin-fin arrays including effects on non-uniform arrays and flow convergence", ASME paper No. 86-GT-132.

Minakami, K., Iwasaki, H., 1994, "Heat transfer characteristics of pin-fins with in line arrangement", Heat Transfer - Japanese Research, Vol. 23, No. 3, pp. 213-228.

Moores, K.A., Joshi, Y.K., 2001, “High performance packaging materials and architectures for improved thermal management of power electronics”, Future Circuits International, Issue No. 7, pp. 45-49.

Moores, K.A., Joshi, Y.K., Schiroky, G.H., 2001, “Thermal characterization of a liquid cooled AlSiC base plate with integral pin fins”, IEEE Transactions on Components and Packaging Technologies, Vol. 24, No. 2, pp. 213-219.

Moores, K.A., Joshi, Y.K., 2003, “Effect of tip clearance on the thermal and hydrodynamic performance of a shrouded pin fin array”, J. Heat Transfer, Vol. 125, Issue 6, pp. 999-1007.

Neely, A.J., Ireland, P.T., Harper, L.R., 1997, “Extended surface convective cooling studies of engine components using the transient liquid crystal technique”, J. Power and Energy, Vol. 211, pp. 273-287.

Norris, R.H., Spofford, W.A., 1942, “High performance fins for heat transfer”, Transactions of the ASME, Vol. 64, pp. 489-496.

Olsen, D.A., 1991, "Heat transfer and pressure drop in a compact pin fin heat exchanger with pin orientation at 18 degrees to the flow direction", NISTIR 3964, National Institute of Standards and Technology, Boulder, Co.

Olsen, D.A., 1992, “Heat transfer in thin, compact heat exchangers with circular, rectangular, or pin-fin flow passages”, Trans. ASME, Journal of Heat Transfer, Vol. 114, pp. 373-382.

Peng, Y., 1984, "Heat transfer and friction loss characteristics of pin fin cooling configurations", Trans. ASME, J. Engineering for Gas Turbines and Power, Vol. 106, pp. 246 – 251.

Pierson, O.L., 1937, “Experimental investigation of the influence of tube arrangement on convection heat transfer and flow resistance in cross flow of gases over tube banks”, Trans. ASME, Vol. 59, pp. 563-572.

Prstic, S., Iyengar, M., Bar-Cohen, A., 2001, ‘Bypass effects in high performance heat sinks”, J. Mechanical Engineering, Vol. 47, No. 8, pp. 441-448.

Rozati, A., Tafti, D.K., Blackwell, N.E., 2008, “Effect of pin tip clearance on flow and heat transfer at low Reynolds numbers”, Trans. ASME, Journal of Heat Transfer, Vol. 130, No. 7, 071704.

Sergent, J.E., Krum, A., 1998, *Thermal Management Handbook: For Electronic Assemblies*, McGraw-Hill Inc., New York, pp.3.9 - 3.15.

Sherrod, P.H., NLREG Users Guide, (www.nlreg.com).

Short, B.E., 1994, “Pressure drop and heat transfer in cast pin fin coldwalls”, Ph.D. Thesis, Southern Methodist University.

Short, B.E., Raad, P.E., Price, D.C., 1994, "Pressure drop and heat transfer in cast pin fin coldwalls used for electronics cooling", HTD-Vol. 292, Heat Transfer in

Electronic Systems, International Mech. Engr. Congress and Exposition, Chicago, IL, Nov. 6 – 11.

Simoneau, R.J., VanFossen, G.J., 1984, "Effects of location in an array on heat transfer to a short cylinder in cross-flow", Trans. ASME, J. Heat Transfer, Vol. 106, pp. 42-48.

Sparrow, E.M., Grannis, V.B., 1991, "Pressure drop characteristics of heat exchangers consisting of arrays of diamond-shaped pin fins", Int. J. Heat Mass Transfer, Vol. 34, No. 3, pp. 589-600.

Sparrow, E.M., Larson, E.D., 1982(A), "Heat transfer from pin-fins situated in an oncoming longitudinal flow which turns to cross-flow", Int. J. Heat Mass Transfer, Vol. 25, No. 5, pp. 603-614.

Sparrow, E.M., Molki, M., "Effect of a missing cylinder on heat transfer and fluid flow in an array of cylinders in cross-flow", Int. J. Heat Mass Transfer, Vol. 25, No. 4, pp. 449-456, 1982B.

Sparrow, E.M, Ramsey, J.W., 1978, "Heat transfer and pressure drop for a staggered cylinder wall attached array of cylinders with tip clearance", Int. J. Heat Mass Transfer, Vol., 21, pp. 1369-1377.

Sparrow, E.M., Ramsey, J.W., Altemani, C.A.C., 1980, "Experiments on in-line pin fin arrays and performance comparisons with staggered arrays", Trans. ASME, J. Heat Transfer, Vol. 102, pp 44-50.

Sparrow, E.M., Samie, F., 1981, "Measured heat transfer coefficients at and adjacent to the tip of a wall-attached cylinder in cross-flow: application to fins", Trans. ASME, J. Heat Transfer, Vol. 103, pp. 778-784.

Sparrow, E.M., Suopys, A.P., Ansari, M.A., 1984, "Effect of inlet, exit and fin geometry on pin fins situated in a turning flow", Int. J. Heat Mass Transfer, Vol. 27, pp. 1039-1054.

Stasiek, J., 1997, "Thermochromic liquid crystals and true color image processing in heat transfer and fluid flow research", Heat and Mass Transfer, Vol. 33, pp. 27-39.

Sun, J.H., Leong, K.C., Liu, C.Y., 1997, "Influence of hue origin on the hue-temperature calibration of thermochromic liquid crystals", Heat and Mass Transfer, Vol. 33, pp. 121-127.

Tanda, G., 2001, "Heat transfer and pressure drop in a rectangular channel with diamond-shaped elements", Int. J. Heat Mass Transfer, Vol. 44, pp. 3529-3541.

Theoclitus, G., 1966, “Heat transfer and flow friction characteristics on nine pin fin surfaces”, Trans. ASME, J. Heat Transfer, pp. 383-390.

Uzol, O., Camci, C., 2001(A), “Elliptical pin fins as an alternative to circular pin fins for gas turbine blade cooling applications part 1: endwall heat transfer and total pressure loss characteristics”, ASME Paper 2001-GT-0180**.**

Uzol, O., Camci, C., 2001(B), “Elliptical pin fins as an alternative to circular pin fins for gas turbine blade cooling applications part 2: wake flow field measurements and visualization using particle image velocimetry”, ASME Paper 2001-GT-0181.

VanFossen, G.J., 1982, “Heat transfer coefficients for staggered arrays of short pin fins”, Trans. ASME, J. Engineering for Power, Vol. 104, pp. 268-274.

Webb, R.L., 1980, “Air-side heat transfer in finned tube heat exchangers”, Heat Transfer Engineering, Vol. 1, No. 3, pp. 33-49.

Zukauskas, A.A., 1972, “Heat transfer from tubes in cross-flow”, Advances in Heat Transfer, Vol. 8, pp. 116-150.